

KALMAN FILTER DESIGN FOR REAL-TIME ESTIMATION OF MODAL
PARAMETERS AND CUTTING FORCE COEFFICIENTS FOR DETERMINING THE
DYNAMIC STABILITY OF HIGH-SPEED LOW-RADIAL-IMMERSION MILLING
PROCESSES

A Dissertation presented to the Faculty of the Mechanical
and Aerospace Engineering Department
at the University of Missouri

In Partial Fulfillment
of the Requirements for the Degree

Doctor of Philosophy

by

JOSIAH A. BRYAN

Dr. Roger Fales, Dissertation Supervisor

MAY 2014

The undersigned have examined the dissertation entitled

**KALMAN FILTER DESIGN FOR REAL-TIME ESTIMATION OF
MODAL PARAMETERS AND CUTTING FORCE COEFFICIENTS FOR
DETERMINING THE DYNAMIC STABILITY OF HIGH-SPEED LOW-
RADIAL-IMMERSION MILLING PROCESSES**

presented by Josiah Bryan,

a candidate for the degree of Doctor of Philosophy,

and hereby certify that, in their opinion, it is worthy of acceptance.

Professor Roger Fales

Professor Frank Feng

Professor Craig Kluever

Professor Frank Pai

Professor Carmen Chicone

ACKNOWLEDGEMENTS

I would like to thank Dr. Roger Fales for his advisement and guidance, and for being so supportive throughout this research. It has been a privilege studying under him.

I would like to thank the Honeywell Kansas City Plant for funding this research and providing equipment. In particular, I would like to thank all the Honeywell engineers and technicians that have been so generous with their time and experience in aiding this project. Their assistance has been invaluable.

I would like to acknowledge Dr. John B. Miles for informing me of the opportunity to be a student intern with the NASA-Missouri Space Grant Consortium and for assisting in the application process, and I thank the NASA-Missouri Space Grant Consortium for the opportunity to be a student intern and for supporting this research.

I would like to thank Khaled Adem, Brian Mooney, and Joseph Gu for their assistance in the lab and their support of this research. Their assistance and friendship have been very great blessings academically and personally.

I would like to thank Anupam Radhakrishnan and Joe Kennedy for all their hard work in providing a starting point for this research.

I would also like to thank my parents and family for their support and helpful observations and all the countless ways they have blessed me. The prayers and counsel of my parents and friends have been critical in this process of growing academically and spiritually.

I would especially like to thank Rachel, my wife and constant supporter, for her love and prayers and encouragement. I am so glad God has placed us on this journey together.

Most of all, I would like to thank my Lord and Savior Jesus Christ Who created the universe He helps me to study. Apart from Him I can do nothing.

TABLE OF CONTENTS

ACKNOWLEDGEMENTS	ii
LIST OF FIGURES	vi
LIST OF TABLES	ix
NOMENCLATURE	x
ABSTRACT	xvi
CHAPTER 1: INTRODUCTION	1
1.1. Chatter Background	1
1.2. Approaches to Identifying System Parameters	2
1.3. Approaches to Modeling Undeformed Chip Thickness	4
1.4. Objectives	5
1.5. Contributions	6
1.6. Overview of the Paper	9
CHAPTER 2: SYSTEM MODELS	12
2.1. Cutting Force & Dynamic Model	12
2.2. Traditional Chip Thickness Model	14
2.3. Numerical Chip Thickness Model	16
CHAPTER 3: EQUIPMENT SETUP	22
3.1. Measuring Tool Deflection	22
3.2. Measuring Cutting Forces	26
CHAPTER 4: FILTER DESIGN	32
4.1. Overview of Kalman Filters	32
4.2. Effect of Modal Parameters and Cutting Coefficients on Stability	34
4.3. Using an EKF to Estimate Modal Parameters	37
4.4. Using an EKF to Estimate Cutting Force Coefficients	44
4.5. Observability	51
CHAPTER 5: SIMULATION RESULTS	54
5.1. System Parameter Identification	54
5.2. Comparison of Chip Thickness Models	62

5.3. Comparison of Simulations to Experiments	69
CHAPTER 6: ESTIMATES	84
6.1. EKF Modal Parameter Estimation	84
6.2. EKF Cutting Force Coefficient Estimation	102
CHAPTER 7: CENTRIFUGAL AND CORIOLIS FORCES	113
7.1. Modification of the Dynamic Model	113
7.2. Simulation Results	117
CHAPTER 8: CONCLUSION	126
8.1. Summary of Findings	126
8.2. Areas for Future Research	129
APPENDIX: RESULTS OF CUTTING FORCE EXPERIMENTS	135
REFERENCES	136
VITA.....	141

LIST OF FIGURES

Figure	Page
2.1. Dynamic model of the milling tool, showing the undeformed chip	14
2.2. Example of finding chip thickness with the numerical model	19
3.1. Sensor mounting fixture, data acquisition system, bottom view of sensor configuration.....	23
3.2. Tool deflection measured at sensor given various deflections at tool tip.	24
3.3. Spindle-mounted dynamometer while slot-milling.....	27
4.1. Example of varying each modal parameter individually to affect TFEA chatter stability. ...	35
4.2. Scaling all three modal parameters by same factor to affect TFEA chatter stability.....	35
4.3. Varying each cutting coefficient individually to affect TFEA chatter stability	36
5.1. Comparison of incline simulations with traditional and numerical chip models.....	65
5.2. Comparison of traditional and numerical chip model simulations over one revolution	65
5.3. Differences between chip model simulations over one revolution	66
5.4. Example of simulated tooth paths and chip thicknesses from each chip model	66
5.5. Once-per-revolution deflection from traditional model with incline #1 parameters.....	68
5.6. Once-per-revolution deflection from numerical model with incline #1 parameters	68
5.7. Experimental tool deflection for incline cuts #1, #2, and #3	71
5.8. Experimental tool deflection for decline cuts #1, #2, and #3.....	72
5.9. Simulated and experimental (incline #1) deflection trajectories over single revolution.....	76
5.10. Simulated and experimental (incline #2) deflection trajectories over single revolution.....	76
5.11. Simulated and experimental (incline #3) deflection trajectories over single revolution.....	77
5.12. Simulated and experimental (decline #1) deflection trajectories over single revolution.....	77

5.13. Simulated and experimental (decline #2) deflection trajectories over single revolution.....	78
5.14. Simulated and experimental (decline #3) deflection trajectories over single revolution.....	78
5.15. Once-per-revolution deflection from traditional model (decline #1, except $c = 26$ kg/s)....	83
5.16. Once-per-revolution deflection from traditional model (decline #1, except $c = 24$ kg/s)....	83
6.1. Modal parameter estimates given simulated deflections along x -axis	88
6.2. Modal parameter estimates given simulated deflections along x - and y -axes.....	89
6.3. Modal parameter estimates given experimental deflections along x -axis.....	92
6.4. Modal parameter estimates given experimental deflections along x - and y -axes	93
6.5. Modal mass and stiffness estimates given simulated deflections along x - and y -axes	95
6.6. Modal mass and stiffness estimates given experimental deflections along x - and y -axes	95
6.7. Modal mass and damping estimates given simulated deflections along x - and y -axes.....	97
6.8. Modal mass and damping estimates given experimental deflections along x - and y -axes.....	97
6.9. Comparison of original and higher-res resampled simulated deflection with noise	99
6.10. Comparison of amplitude spectra of original and higher-res resampled simulated data	99
6.11. Comparison of amplitude spectra of original and lower-res resampled simulated data	101
6.12. Comparison of amplitude spectra of original and higher-res resampled experimental data	101
6.13. Tangential coefficient estimates (separate teeth) given simulated data for both axes	105
6.14. Radial coefficient estimates (separate teeth) given simulated data for both axes.....	105
6.15. Tangential coefficient estimates (separate teeth) given experimental data for both axes..	107
6.16. Radial coefficient estimates (separate teeth) given experimental data for both axes.....	107
6.17. Tangential and radial coefficient estimates (teeth together) given sim data for both axes	109
6.18. Chip thicknesses calculated during EKF iterations given simulated data for both axes....	109
6.19. Tangential coefficient estimates (separate teeth) on ten trials given experimental data....	111
6.20. Radial coefficient estimates (separate teeth) on ten trials given experimental data.....	111
7.1. Diagram of applied and inertial forces, including centrifugal and Coriolis forces	114
7.2. Once-per-revolution deflection from inertial force model with incline #1 parameters	118

7.3. Cutting and inertial forces of inertial model over single revolution (incline #1).....	119
7.4. Deflection and chip thickness of inertial model over single revolution (incline #1)	119
7.5. Once-per-revolution displacement of inertial model (incline #1) with eccentricity	121
7.6. Cutting and inertial forces of inertial model (incline #1) over one rev with eccentricity	123
7.7. Deflection and chip thickness of inertial model (inc. #1) over one rev with eccentricity....	123
7.8. Simulated displacement over multiple revolutions without eccentricity (incline #1).....	124
7.9. Simulated displacement over multiple revolutions with eccentricity (incline #1).....	124
7.10. Raw experimental displacement over multiple revolutions (incline #1).....	125

LIST OF TABLES

Table	Page
5.1. Bifurcation points of six simulated and experimental cuts (incline and decline)	71
5.2. System parameter estimates from six experimental cuts (incline and decline).....	81

NOMENCLATURE

Abbreviations

EKF	=	Extended Kalman Filter
FPGA	=	Field-Programmable Gate Array
TFEA	=	Time Finite Element Analysis
UKF	=	Unscented Kalman Filter

Symbols

b	=	axial depth of cut, m
c_x	=	modal damping parameter in x -direction, kg/s
c_y	=	modal damping parameter in y -direction, kg/s
$F_{1,1}, F_{1,2}, F_{2,1}, F_{2,2}, \dots, F_{i,j}$	=	i th-row j th-column element of \mathbf{F}_{k-1}
F_{Cor}	=	Coriolis force applied to tool, N
F_{cen}	=	centrifugal force applied to tool, N
\mathbf{F}_{k-1}	=	matrix partial derivative equal to $\left. \frac{\partial f_{k-1}}{\partial x} \right _{\hat{x}_{k-1}^+}$
F_r	=	radial force applied to active cutting tooth, N
\bar{F}_r	=	average magnitude of radial force over one revolution, N
\bar{F}_{rc}	=	slope of the best-fit average-magnitude radial-force-vs.-feed-rate line (N/m)

\bar{F}_{re}	=	vertical intercept of the best-fit average-magnitude radial-force-vs.-feed-rate line (N)
F_{rp}	=	radial force acting on tooth p , N
F_t	=	tangential force applied to active cutting tooth, N
\bar{F}_t	=	average magnitude of tangential force over one revolution, N
\bar{F}_{tc}	=	slope of the best-fit average-magnitude tangential-force-vs.-feed-rate line (N/m)
\bar{F}_{te}	=	vertical intercept of the best-fit average-magnitude tangential-force-vs.-feed-rate line (N)
F_{tp}	=	tangential force acting on tooth p , N
F_x	=	sum of forces acting in x -direction, N
F_y	=	sum of forces acting in y -direction, N
f_{k-1}	=	system state update function evaluated at states from previous ($k - 1$) iteration
g_p	=	switching function for tooth p
\mathbf{H}_k	=	matrix partial derivative equal to $\left. \frac{\partial h_k}{\partial x} \right _{\hat{x}_k^-}$
h	=	feed per tooth, m
h_k	=	system measurement update function evaluated at states from current (k th) iteration
\mathbf{I}	=	identity matrix with dimensions matching $\mathbf{K}_k \mathbf{H}_k$
\mathbf{K}_k	=	Kalman filter gain matrix on current (k th) iteration
K_r	=	radial cutting force coefficient, N/m ²
K_{r1}, K_{r2}	=	radial cutting force coefficients of first and second teeth, respectively, N/m ²
K_{rc}	=	radial cutting force linear (first-order) coefficient

		(equivalent to K_r), N/m ²
K_{re}	=	radial cutting force edge (zeroth-order) coefficient, N/m
K_t	=	tangential cutting force coefficient, N/m ²
K_{t1}, K_{t2}	=	tangential cutting force coefficients of first and second teeth, respectively, N/m ²
K_{tc}	=	tangential cutting force linear (first-order) coefficient (equivalent to K_t), N/m ²
K_{te}	=	tangential cutting force edge (zeroth-order) coefficient, N/m
k_x	=	modal stiffness parameter in x -direction, N/m
k_y	=	modal stiffness parameter in y -direction, N/m
L_{k-1}	=	matrix partial derivative equal to $\left. \frac{\partial f_{k-1}}{\partial \mathbf{w}} \right _{\hat{\mathbf{x}}_{k-1}^+}$
M_k	=	matrix partial derivative equal to $\left. \frac{\partial h_k}{\partial \mathbf{v}} \right _{\hat{\mathbf{x}}_k^-}$
m_x	=	modal mass parameter in x -direction, kg
m_y	=	modal mass parameter in y -direction, kg
N	=	total number of system states
n	=	number of cutting teeth
\mathbf{O}	=	observability matrix
\mathbf{P}_k^-	=	<i>a priori</i> covariance matrix of estimation error on current (k th) iteration
\mathbf{P}_k^+	=	<i>a posteriori</i> covariance matrix of estimation error on current (k th) iteration
p	=	current tooth number
\mathbf{Q}_k	=	covariance matrix of process noise on current (k th)

		iteration
R	=	distance from rotation center to tool center, m
\mathbf{R}_k	=	covariance matrix of measurement noise on current (k th) iteration
r	=	tool radius, m
r_0	=	eccentricity of undeflected centerline, m
r_i	=	radial depth of cut (or radial immersion), m
T	=	time step for system update equations, s
t	=	time, s
U_i	=	x -position of point in previous tooth path, m
U_p	=	displacement of tooth p in x -direction, m
\mathbf{u}_{k-1}	=	system input vector on previous ($k - 1$) iteration
V_i	=	y -position of point in previous tooth path, m
V_p	=	displacement of tooth p in y -direction, m
\mathbf{v}_k	=	measurement noise vector on current (k th) iteration
$v_{x,k}$	=	tool deflection measurement noise along x -axis on current (k th) iteration, m
$v_{y,k}$	=	tool deflection measurement noise along y -axis on current (k th) iteration, m
$w_{C,k-1}$	=	modal damping process noise on previous ($k - 1$) iteration, kg/s^2
$w_{K,k-1}$	=	modal stiffness process noise on previous ($k - 1$) iteration, N/m-s
\mathbf{w}_{k-1}	=	process noise vector on previous ($k - 1$) iteration

$w_{M,k-1}$	=	modal mass process noise on previous ($k - 1$) iteration, kg/s
w_p	=	undeformed chip thickness due to tooth p , m
$w_{p,k-1}$	=	undeformed chip thickness due to tooth p on previous ($k - 1$) iteration, m
x	=	tool deflection in x -direction, m
$x_{1,k}, x_{2,k}, \dots, x_{i,k}$	=	elements of state vector on k th iteration
$\hat{x}_{1,k-1}^+, \hat{x}_{2,k-1}^+, \dots, \hat{x}_{i,k-1}^+$	=	elements of <i>a posteriori</i> state estimate vector on previous ($k - 1$) iteration
\mathbf{x}_k	=	system state vector on current (k th) iteration
$\hat{\mathbf{x}}_k^-$	=	<i>a priori</i> state estimate vector on current (k th) iteration
$\hat{\mathbf{x}}_k^+$	=	<i>a posteriori</i> state estimate vector on current (k th) iteration
x_{n-1}	=	tool deflection in x -direction on previous ($n - 1$) revolution, m
x_n	=	tool deflection in x -direction on current (n th) revolution, m
y	=	tool deflection in y -direction, m
\mathbf{y}_k	=	system measurement vector on current (k th) iteration
α	=	slope of current tooth radial line in numerical chip thickness model, m/m
β	=	y -intercept of current tooth radial line in numerical chip thickness model, m
δ	=	distance between (U_i, V_i) in previous tooth path and nearest point in radial line, m
δ_x	=	horizontal position of point in radial line nearest (U_i, V_i) in previous tooth path, m

δ_y	=	vertical position of point in radial line nearest (U_i, V_i) in previous tooth path, m
θ	=	angular displacement of tool, rad
θ_0	=	angle of eccentricity vector, rad
θ_{dyn}	=	angle of dynamometer with respect to cutting teeth, rad
θ_{entry}	=	angular displacement at entry of cut (traditional chip thickness model), rad
θ_{exit}	=	angular displacement at exit of cut (traditional chip thickness model), rad
θ_p	=	angular displacement of tooth p , rad
$\theta_{p,k-1}$	=	angular displacement of tooth p on previous $(k - 1)$ iteration, rad
τ	=	time required for one tooth pass, s
ϕ	=	angle from positive x -axis to tool deflection vector, rad
ω	=	spindle speed, rpm
ω_π	=	spindle speed, rad/s

KALMAN FILTER DESIGN FOR REAL-TIME ESTIMATION OF MODAL PARAMETERS AND CUTTING FORCE COEFFICIENTS FOR DETERMINING THE DYNAMIC STABILITY OF HIGH-SPEED LOW-RADIAL-IMMERSION MILLING PROCESSES

Josiah A. Bryan

Dr. Roger Fales, Dissertation Supervisor

ABSTRACT

Chatter is a particularly severe form of tool vibration that can occur in milling processes. Present under certain combinations of spindle speed and axial depth of cut, chatter accelerates tool wear and produces a poor surface finish of machined parts. The ability to predict the onset of chatter in a particular tool-workpiece dynamic system could enable the development of a control system that advises the operator of corrective measures to avoid imminent chatter or that automatically controls the machine to take such corrective measures. Because chatter stability depends on parameters that vary from one tool-workpiece system to another, and because these parameters are affected by tool wear and other factors, a chatter avoidance system would benefit from the ability to reliably estimate relevant system parameters in real time. Various Extended Kalman Filters (EKFs) are considered here for estimating modal parameters or cutting force coefficients of the tool-workpiece dynamic system from tool deflection measurements. These parameter estimates could be used to predict the dynamic stability of the system.

The tool-workpiece system is observable if tool deflection measurements along the x -axis are given and only one system parameter is estimated, as previous research has shown. This study makes use of tool deflection measurements along the y -axis, allowing

one more system parameter to be estimated while maintaining observability. A novel observable system is described here in which both a radial and a tangential cutting force coefficient can be estimated. A separate set of force coefficients for each cutting tooth may also be estimated, provided no two teeth cut simultaneously.

Simulations of the milling process were considered with a traditional and a numerical chip thickness model from previous research. The numerical chip thickness model was modified to significantly reduce computational time. The EKFs were tested on simulated deflection data from the traditional model and were found to estimate system parameters with good accuracy and repeatability.

Experimental tool deflection measurements were taken from high-speed, low-radial-immersion milling processes (which are studied because of their wide application in industrial high-precision machining), and the EKFs were used to estimate system parameters from these measurements. The resulting estimates were compared with alternative measurement approaches (i.e., hammer tests to find modal parameters and dynamometer tests to calculate cutting force coefficients) and were found to differ significantly. However, tool trajectories simulated with the estimated system parameters were found to correlate well with experimental deflection measurements, and simulated bifurcation points in a minority of trials correlated well with experimental observations.

Model modifications were proposed to include centrifugal and Coriolis inertial forces, which may be significant in high-speed milling, and to accommodate eccentricity of the undeflected tool center from the center of rotation (as in runout). Early simulations with these modifications produced intriguing bifurcation behavior but did not reflect experimental trajectories. Other system modifications were proposed for future work.

CHAPTER 1: INTRODUCTION

1.1. Chatter Background

Chatter is a phenomenon that develops in milling processes under certain combinations of spindle speed and axial depth of cut, characterized by severe tool vibrations, accelerated tool wear, and poor surface finish of the machined part. Chatter limits material removal rate and productivity by forcing industrial milling processes to use overly conservative spindle speeds or depths of cut. The ability to predict the onset of chatter in a particular tool-workpiece dynamic system would enable manufacturers to maximize material removal rates while avoiding cutting conditions that provoke chatter.

Explaining the reasons for chatter has been the topic of considerable research for over fifty years [1]-[2]. The dynamics of metal-cutting has been investigated experimentally and analytically, demonstrating that surface waviness affects cutting force and might result in unstable cutting processes [3]. Analytical approaches to predicting chatter have been proposed based on experimentally determined constants [4], and a conservative stability criterion has been developed [5]. Stability lobe calculation has also been accomplished through time-domain simulations [6]-[7], a graphical method [8], a numerical solution [9], and Fourier-series expansions of force coefficients [10]. Time Finite Element Analysis (TFEA) and semi-discretization (SD) methods have also been proposed to determine stability bounds [11], and Poincaré sections have been used to determine whether chatter is present (as discussed in [12]-[13]).

Throughout the discussion of chatter stability in literature, modal parameters and cutting force coefficients play an important role in characterizing the system that is

analyzed. Accurate knowledge of these system parameters is necessary to accurately predict stability boundaries for the system for, as noted in [5], one stability chart does not suffice for a given machine. Stability depends on the particular characteristics (such as stiffness, damping, mass, cutting force coefficients, etc.) of the tool-workpiece system being used, and these characteristics may change over time (e.g., as the tool wears).

This research is concerned primarily with high-speed, low-radial-immersion milling processes, which are frequently used in industry for applications that involve complex geometries and are difficult to machine (e.g., lightweight aerospace materials). Some research has already been conducted in this area [14-16], but the majority of milling research thus far has focused on slot-milling, or full-radial-immersion milling, due to its inherently simpler mathematics and analytical solutions.

1.2. Approaches to Identifying System Parameters

Modal characteristics and cutting force coefficients represent two categories of information that must be identified for a given tool-workpiece system before the system can be simulated or typical stability analysis approaches can be used. The modal characteristics can be represented in various ways, as with a frequency response function [17] or with modal mass, damping, and stiffness parameters [18-20]. A typical approach to finding these modal characteristics involves striking the milling tool with a piezoelectric hammer (recording the impulse forcing function) while simultaneously measuring the acceleration of the tool with a piezoelectric accelerometer mounted on the opposite side of the tool (this approach is described in [17]). From the dynamic response of the tool for the given impulse, the modal characteristics of the tool can be found.

Spindle bearing stiffness has been found to vary with spindle speed [21, 22], and it is possible that modal damping and mass of the tool and spindle would also be affected by changes in cutting conditions. Alternative approaches to finding modal parameters include conducting finite-element analysis of the spindle structure [22], operational modal analysis [23] conducted with accelerometers and dynamometer while machining, and conducting impulse tests on a non-rotating outer spindle bearing while the spindle was rotating [24], using laser sensor measurements to verify dynamic compliance at various speeds.

Approaches to finding cutting force coefficients vary but typically require the cutting forces to be measured with a dynamometer (see [25-33] for examples). One approach proposes using surface error measurements instead of force measurements to find cutting force coefficients [34]. Another approach uses capacitive displacement sensors at the spindle to indirectly measure cutting force (with limited bandwidth, but improved by filtering out the spindle dynamics with a Kalman filter) [24]. Though this approach made use of a Kalman filter, it did not estimate the modal parameters or cutting force coefficients in real time. As in [27], cutting conditions (such as feed rate and spindle speed) and tool runout can affect cutting force coefficients significantly.

Because of the prohibitive effort required to thoroughly identify the modal parameters and cutting force coefficients of every tool-workpiece system over the range of cutting scenarios it may encounter, it is highly desirable to find a means of accurately identifying modal parameters and cutting force coefficients in real time while cutting. A real-time approach is even more important because such a battery of tests would become outdated as the tool became worn. Real-time milling parameter identification has not

been found in existing literature, except in [35], in which modal parameters were estimated by an Extended Kalman Filter (EKF) from tool deflection measurements along one axis (only one parameter could be estimated with observability). Therefore, using an EKF to efficiently and accurately estimate modal parameters or cutting force coefficients, with the aim of doing so in real time, serves as a primary focus of this study.

1.3. Approaches to Modeling Undeformed Chip Thickness

Not only must the system parameters be known accurately, but the system model used by the estimator must also accurately reflect the milling process. One of the most important parts of the model is calculating the undeformed chip thickness. This calculation plays an integral role in determining the cutting force acting on the tool which, in turn, significantly affects the dynamic response of the tool.

Undeformed chip thickness has been approximated by various means. Early models assume the tooth path is a circle and approximate chip thickness as a sinusoid [17]. More sophisticated models include the effect of feed rate on the tooth path, assuming the path to be a trochoid instead of a circle [36-38]. It has been proposed that dynamic chip thickness, which is dependent on the displacements of the cutting teeth in two dimensions, both at the current time and at the time one tooth-pass before, is critical in stability analysis [36-38]. Dynamic chip thickness requires the use of delay differential equations to model tool motion. The delay between tooth passes can either be assumed to be constant or can vary with feed per tooth or another cutting condition. Some sophisticated analytical approaches consider the intersection of the current tooth with the path of the previous tooth while ignoring the dynamics of the tool [39]. The

interaction between tool dynamics and previous tooth passes, however, is more difficult to model analytically. This interaction has been successfully modeled through numerical simulation [40].

Two chip thickness models are employed in this research: a traditional one in which the tooth path is a circle, and a more contemporary one that numerically seeks intersection points between the current tooth and a previous tooth path. The numerical model produces tooth paths that are trochoidal in shape, like those in [36-38], but without making any assumptions about the period of delay from one tooth pass to another. The tooth is assumed to engage the workpiece only when an intersection is found, rather than always engaging after a specified amount of time has passed. Furthermore, the dynamic chip thickness is determined by the intersection point and not simply by the tooth position at a specified time beforehand. This numerical model closely resembles the ones in Radhakrishnan [40] and Kennedy [35]. Sections 2.2 and 2.3 describe these two chip thickness models in more detail, and Section 5.2 compares simulations conducted with these models.

1.4. Objectives

The long-term goal of this research is to develop a control system that uses deflection measurements of the milling tool, estimates system parameters relevant to chatter stability, generates a stability diagram identifying the proximity of current cutting conditions to the nearest chatter region, and either advises an operator of corrective measures to take if chatter is imminent or else automatically controls the milling system to take such corrective measures. Solutions to this problem must be robust and

computationally fast enough to operate in real time in a broad range of milling scenarios. The objective of this paper, then, is to further efforts toward this goal by considering means of improving the accuracy, speed, and robustness of key elements of the control system, especially by considering alternative designs of the filter used to estimate system parameters relevant to chatter stability. Designing such a filter involves considering the observability of the system, the accuracy and speed of the filter in converging on estimates, and the effective use of those estimates in accurately and efficiently analyzing the stability of the system. Key elements of the control system to be evaluated for accuracy and efficiency also include the chip thickness model used by the filter, the selection of an algorithm to calculate chatter stability, and the control algorithm used to avoid chatter. Though the control algorithm is not considered in detail here, a proposed solution can be found in [35].

1.5. Contributions

The primary contributions of this paper to the existing body of research lie in three areas: 1) using an EKF to estimate the cutting force coefficients of the tool-workpiece dynamic system based on measurements of tool deflections in the x - and y -directions, 2) analyzing the observability of a system that estimates the cutting force coefficients of the tool-workpiece dynamic system based on measurements of tool deflections in the x - and y -directions, and 3) considering the effects of centrifugal and Coriolis inertial forces in a numerical simulation of the tool-workpiece dynamic system.

The first contribution is novel in its estimation of cutting force coefficients instead of modal parameters as a step toward calculating chatter stability. As discussed in

Kennedy [35], an EKF has been used to estimate the modal parameters of the tool-workpiece system based on simulated and experimental tool deflection data in the x -direction, resulting in parameter estimates that match (within a few percent) the parameters found by impulse-response experiment. Kennedy considers the observability of such a system, however, and discovers that the system remains observable only if one modal parameter is estimated, but the system loses observability if two or more are estimated. Given that there are three modal parameters, this limitation means there is no guarantee that the tool dynamics can be fully characterized using measurements by Kennedy's approach which, in turn, limits the ability of the chatter stability analysis to robustly accommodate the tool-workpiece combinations and conditions it encounters.

As will be addressed in Chapter 4, the inclusion of tool deflection measurements in the y -direction allows the system to maintain observability while estimating two parameters. This still does not allow an EKF to estimate all three modal parameters reliably and, therefore, Kennedy's approach would still have no guarantee of convergence. If, however, an EKF were to estimate cutting force coefficients (of which there are two) instead of modal parameters, the dynamic system might be equivalently characterized as with modal parameter estimates, but still allow the filter to have guaranteed convergence on its estimates. Estimating a cutting force coefficient has the same effect on chatter stability as estimating a gain applied to the modal parameters, as will be shown in Chapter 4. Estimating the two cutting force coefficients, then, may allow the same freedom in adjusting the chatter boundaries to accommodate various cutting scenarios as estimating the three modal parameters. This will be discussed at greater length in Chapter 4.

The second contribution is novel in its consideration of whether a system that estimates cutting force coefficients based on measurements of tool deflections in the x - and y -directions is, in fact, observable. As just mentioned, it is believed that such a system would be observable, but analysis of the system must be conducted to confirm this belief. Furthermore, the EKF must be applied to simulated and experimental data to determine if its performance is as expected. If the system is found to be observable, this contribution would improve upon the system described in Kennedy [35].

The third contribution is novel in its consideration of centrifugal and Coriolis inertial forces in a numerical simulation of the milling process. As discussed in Chapter 7, these forces were found to have magnitudes that were very significant compared to the cutting forces. Chapter 7 includes a description of modifications made to the dynamic system of Section 2.1 to include these forces. In addition, it is proposed that the undeflected center of mass of the tool does not necessarily coincide with the center of tool rotation (as in the case of tool runout). A new parameter is, therefore, described in Chapter 7 for the purpose of offsetting the reference point of the spring model from the center of rotation, which is also the origin of the coordinate axes. Simulations are conducted with these model modifications, but so far no system parameters have been identified that allow this simulation to closely reflect experimental data.

Two secondary contributions are also noted here: 1) a modification was made to the numerical chip thickness model developed by Kennedy [35] that increases its computational speed significantly, and 2) cutting force coefficients were determined experimentally for a variety of tool-workpiece combinations. The first contribution, which will be discussed in Section 2.3, consists of replacing a numerical search with a

simple analytical formula. The numerical search would find the distance of a point in a previous tooth path to the current tooth, a problem that can be solved analytically without any numerical search. This modification allowed milling simulations to run as much as sixteen times faster (e.g., 3 min instead of 48 min). Not only does this improvement allow the effects of modifying system parameters to be studied more easily through simulations, but it also makes implementation of the numerical chip thickness model in a real-time parameter estimator more feasible. The second contribution made use of a spindle-mounted dynamometer to measure the cutting forces acting on the tool while milling slots (full radial immersion). The methods involved in these measurements are discussed in Section 3.2, and the resulting cutting force coefficients will be presented in the Appendix. Having known cutting force coefficients associated with particular tool-workpiece combinations provides a foundation for comparing simulations of the milling process to experimental results, as well as for comparing filter-based estimates of the cutting force coefficients to the experimental values. Experimentally determined coefficients relieve the need to approximate them theoretically or to locate values for a similar tool-workpiece combination in literature, where such a tool and workpiece may differ in significant ways from those used in this research.

1.6. Overview of the Paper

Chapter 2 describes the system models used to represent the tool dynamics during the milling process. First the cutting force and dynamic models are described (Section 2.1), followed by discussions of two different chip thickness models used in this paper. The first is a traditional model, considering tooth path to be circular and assuming

constant entry and exit angles for the tooth engaged in the workpiece (Section 2.2). The second is a numerical model that seeks intersections between the current tooth and previous tooth paths, assuming the tooth is cutting only when such an intersection is found (Section 2.3).

Chapter 3 describes the equipment setup used in this paper to experimentally measure tool deflection (Section 3.1) and to measure cutting forces (Section 3.2). The corresponding approach to determining cutting force coefficients is presented as well.

Chapter 4 discusses the design of a Kalman filter to estimate system parameters relevant to chatter stability analysis. First an overview of Kalman filters and their role in this research is presented (Section 4.1), followed by a discussion of the relevance of modal parameters and cutting force coefficients to chatter stability (Section 4.2). Then EKF's are described that estimate modal parameters (Section 4.3) and cutting force coefficients (Section 4.4). The respective observability of each approach is considered (Section 4.5), with and without the inclusion of tool deflection measurements in the y -direction.

Chapter 5 summarizes results of simulating the milling process using the chip thickness models described in Chapter 2. System parameters are identified for use in the milling simulations (Section 5.1). Simulations are compared between the two chip thickness models (Section 5.2), and then both models are compared to experimental results (Section 5.3).

Chapter 6 compares the performance of some filters discussed in Chapter 4. First an EKF estimates modal parameters using simulated and experimental tool deflection

data (Section 6.1), then an EKF estimates cutting force coefficients using simulated and experimental tool deflection data (Section 6.2).

Chapter 7 discusses the effects of adding centrifugal and Coriolis inertial forces to the dynamic model. Modification of the dynamic model to include these forces is discussed (Section 7.1), as well as a modification to accommodate eccentricity in the tool, followed by some results of using these modifications in simulations (Section 7.2).

Chapter 8 summarizes the findings of this paper (Section 8.1) and considers areas of future research (Section 8.2) that might further the goal of developing a control system to prevent chatter. The Appendix lists the results of the cutting force coefficient experiments described in Section 3.2.

CHAPTER 2: SYSTEM MODELS

2.1. Cutting Force & Dynamic Model

The dynamic model of the milling tool is a mass-spring-damper system with two degrees of freedom, allowing deflections along x - and y -axes (Fig. 2.1). Radial and tangential forces, F_{tp} and F_{rp} respectively, act on tooth p at time t and are [20]

$$F_{tp}(t) = K_t b w_p(t)^\gamma \quad (2.1)$$

$$F_{rp}(t) = K_r b w_p(t)^\gamma \quad (2.2)$$

where K_t and K_r are, respectively, the tangential and radial cutting force coefficients (N/m^2), b is the axial depth of cut (m), $w_p(t)$ is the undeformed chip thickness (m) engaged by tooth p at time t , and γ is a term that allows force to be a nonlinear function of chip thickness. For the purposes of this research, γ is assumed to equal one, making force a linear function of chip thickness. Time t is given in seconds, and force is given in newtons. The forces in the x - and y -directions, F_x and F_y respectively, are then found by conducting coordinate transformations on the radial and tangential forces, and by summing the forces over all the teeth as

$$F_x(t) = \sum_{p=1}^n -[F_{tp}(t) \cos \theta_p(t) + F_{rp}(t) \sin \theta_p(t)] g_p(t) \quad (2.3)$$

$$F_y(t) = \sum_{p=1}^n [F_{tp}(t) \sin \theta_p(t) - F_{rp}(t) \cos \theta_p(t)] g_p(t) \quad (2.4)$$

where n is the number of teeth on the milling tool, $\theta_p(t)$ is the angular displacement (deg) of tooth p at time t , and $g_p(t)$ is a switching function that equals one when the p th tooth is cutting and zero otherwise. The switching function will be discussed in greater detail in Sections 2.2 and 2.3.

The tool dynamics are modeled as mass-spring-damper systems in the x - and y -directions as

$$m_x \ddot{x}(t) + c_x \dot{x}(t) + k_x x(t) = F_x(t) \quad (2.5)$$

$$m_y \ddot{y}(t) + c_y \dot{y}(t) + k_y y(t) = F_y(t) \quad (2.6)$$

where m_x and m_y are the modal mass parameters (kg), c_x and c_y are the modal damping parameters (kg/s), k_x and k_y are the modal stiffness parameters (N/m), and $x(t)$ and $y(t)$ are the tool deflections (m) at time t , all in the x - and y -directions, respectively. Dot notation denotes time derivatives. It is believed that the modal parameters of the tool can be approximated by use of an impulse-response experiment. The tool is first excited by a known impulse, such as that of a hammer with a piezoelectric transducer, and then the dynamic response of the tool is measured with an accelerometer attached to the tip of one of the flutes of the tool. An error minimization algorithm is employed to find the modal parameters that best characterize the tool, matching the simulated response to that of the

experiment for the given impulse. It is unclear how accurately this test (which is conducted while the tool is neither rotating nor cutting) reflects the modal parameters of the tool-workpiece system during the milling process. Perhaps a real-time estimator could approximate these values more accurately for the dynamic system while milling, as will be discussed in Chapter 4.

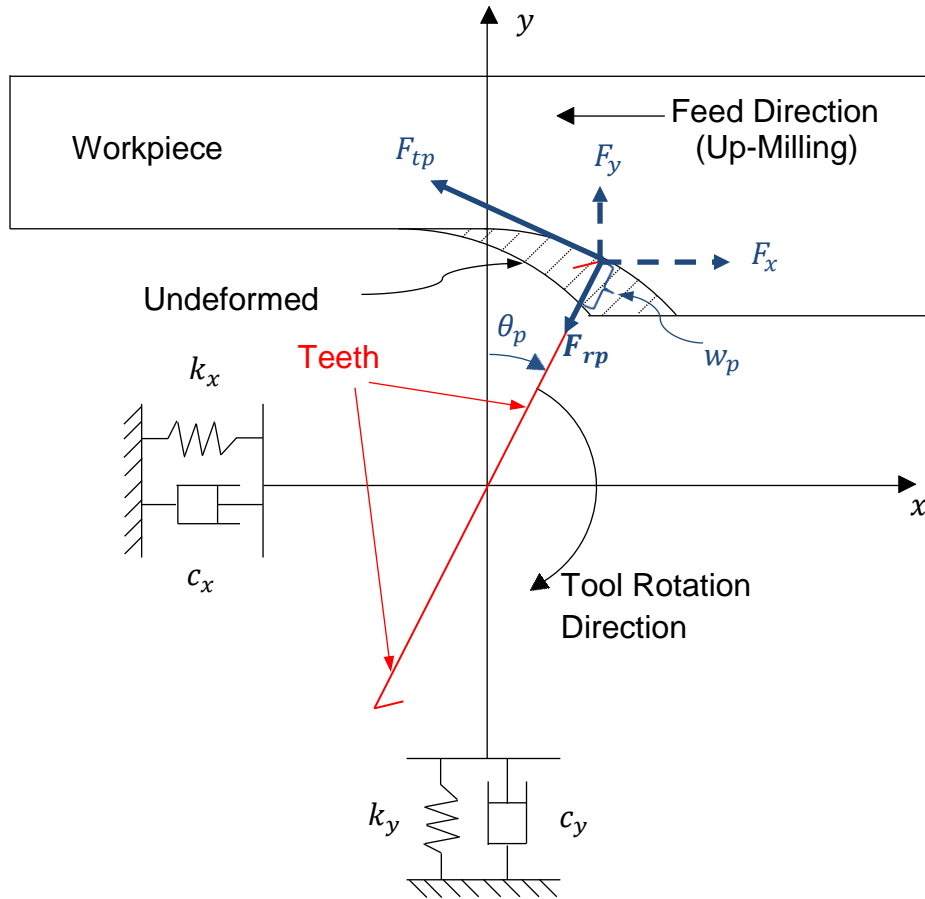


Figure 2.1. Dynamic model of the milling tool, showing the undeformed chip.

2.2. Traditional Chip Thickness Model

This research makes use of two chip thickness models, as mentioned in Section 1.2. A traditional model is considered here that assumes a circular tooth-path shape with constant, known angles of entry and exit of the cut. A more contemporary model is

considered in Section 2.3 that numerically seeks intersection points between the current tooth and a previous tooth path, making no assumptions about entry and exit angles. The numerical model produces a more trochoidal tooth-path shape, though the shape itself is dependent on the deflection of the tool.

According to the traditional model, chip thickness $w_p(t)$ is found as [20]

$$w_p(t) \cong h \sin \theta_p(t) + [x(t) - x(t - \tau)] \sin \theta_p(t) + [y(t) - y(t - \tau)] \cos \theta_p(t) \quad (2.7)$$

where h is the feed rate per tooth (m) and τ is the time delay (s) from one tooth pass to the next. The first term of Eq. (2.7) represents the static chip thickness, due only to feed, and the second two terms represent the dynamic chip thickness, due to the tool deflection either toward the material or away from it. Because the entry and exit angles of the cut are assumed to be constant in this model, the switching function $g_p(t)$ in Eqs. (2.3)-(2.4) is defined as one if $\theta_{entry} \leq \theta_p(t) \leq \theta_{exit}$ and zero otherwise. In up-milling, teeth enter the material by cutting into a surface that has already been cut and exit by leaving the original surface of the material. The entry and exit angles θ_{entry} and θ_{exit} in up-milling are defined as

$$\theta_{entry} = 0 \quad (2.8)$$

and

$$\theta_{exit} = \cos^{-1} \left(1 - \frac{r_i}{r} \right) \quad (2.9)$$

where r is the tool radius (m) and r_i is the radial depth of cut or radial immersion (m). Note that Eqs. (2.8)-(2.9) do not hold for down-milling, in which the tool enters the original surface and exits a surface that has already been cut. Down-milling is omitted here because it is not addressed in this research.

2.3. Numerical Chip Thickness Model

The numerical model seeks intersections between the current tooth and previous tooth paths and, therefore, requires the positions of each tooth. The position of the tip of tooth p is defined by

$$U_p(t) = r \sin \theta_p(t) + x(t) + \frac{nh\omega t}{60} \quad (2.10)$$

$$V_p(t) = r \cos \theta_p(t) + y(t) \quad (2.11)$$

where $U_p(t)$ and $V_p(t)$ represent the displacements (m) of the tooth tip at time t along the x - and y -axes, respectively, and ω is the spindle speed (rpm). It is assumed that spindle speed remains constant throughout the milling process, in part because the machine attempts to regulate the speed at its desired value and in part because the mass of the spindle acts as a flywheel to resist perturbations that might alter the speed. The final term

of Eq. (2.10), which accounts for the effect of feed in displacing the tooth, is responsible for causing the shape of the tooth path to resemble a trochoid.

Whenever a tooth tip is found to be beyond the original surface of the material, a numerical search is conducted to find any intersections between the tooth and previous tooth paths. Note that the tooth is represented as a line, defined by the tooth tip and the tool center, and the previous tooth paths are approximated as a set of discrete points, one point for each time step of simulation. The minimum distances from the tooth to every discrete point in the previous tooth paths (up to some specified number of revolutions) are found analytically. A candidate intersection point exists when a locally minimum distance is found between the tooth (Fig 2.2) and a point in a previous tooth path and when this distance is below some appropriate threshold (to avoid considering unreasonable candidates, such as intersections of tooth paths with the non-cutting tooth, which in a two-flute tool occupies the same line). Of the two points in the tooth path that are adjacent to the candidate intersection point, the point that is nearer to the current tooth is selected as an assisting point. A line is defined by the candidate point and the assisting point to locally approximate the slope of the surface. Then the intersection between the tooth line and the local surface line is calculated analytically. This process is repeated for as many candidate intersection points as are found. If a candidate intersection has a y -component less than that of the tooth tip, then the distance from the tooth tip to that candidate intersection is found. These distances represent candidate chip thicknesses, and the minimum candidate chip thickness is selected as the current chip thickness because it corresponds to the intersection of the cutting tooth with the deepest cut previously made, which is also the current surface of the material. If a candidate

intersection has a y -component greater than that of the tooth tip, then a previous tooth path has already exceeded the reach of the tooth in question, and no valid intersections exist because the tooth is not in contact with the material. Hence, at times, particularly when chatter is present, the search algorithm finds no valid intersection points (and sometimes no candidate intersections points at all, as when the tooth is parallel to the surface) because the tooth does not contact the material.

The number of revolutions over which to conduct the search can be adjusted depending on current milling conditions in order to balance accuracy and computational cost. In simulation every previous revolution is included in the search until five revolutions have occurred. Then until ten revolutions have occurred, the previous 2.05 revolutions are included in the search. The value 2.05 is selected because it allows the search to consider tooth-path data for two complete revolutions (where chatter may prevent certain tooth passes from contacting the workpiece), plus an additional 0.05 revolution that provides a slight factor of safety for finding tool-workpiece intersections, given that a deflected tooth may intersect the workpiece at a later rotation angle than the angle at which the previous cut was made. Following the first ten revolutions, only the previous 0.55 revolution (slightly more than one tooth pass) is included in the search to speed up computation. In chatter-free cutting, the current tooth usually only intersects the tooth path of the previous tooth, and the delay between tooth passes remains nearly constant. In simulation the tool deflection is compared at each time step to the deflection at the same point in the previous revolution, and if the deflection has changed severely, as it does in chatter, the search window is expanded again to 2.05 revolutions. In this manner the simulation conducts a more thorough search for intersection points between the

current tooth and previous tooth paths when chatter is present. The switching function $g_p(t)$ equals one if a valid intersection is found and zero otherwise.

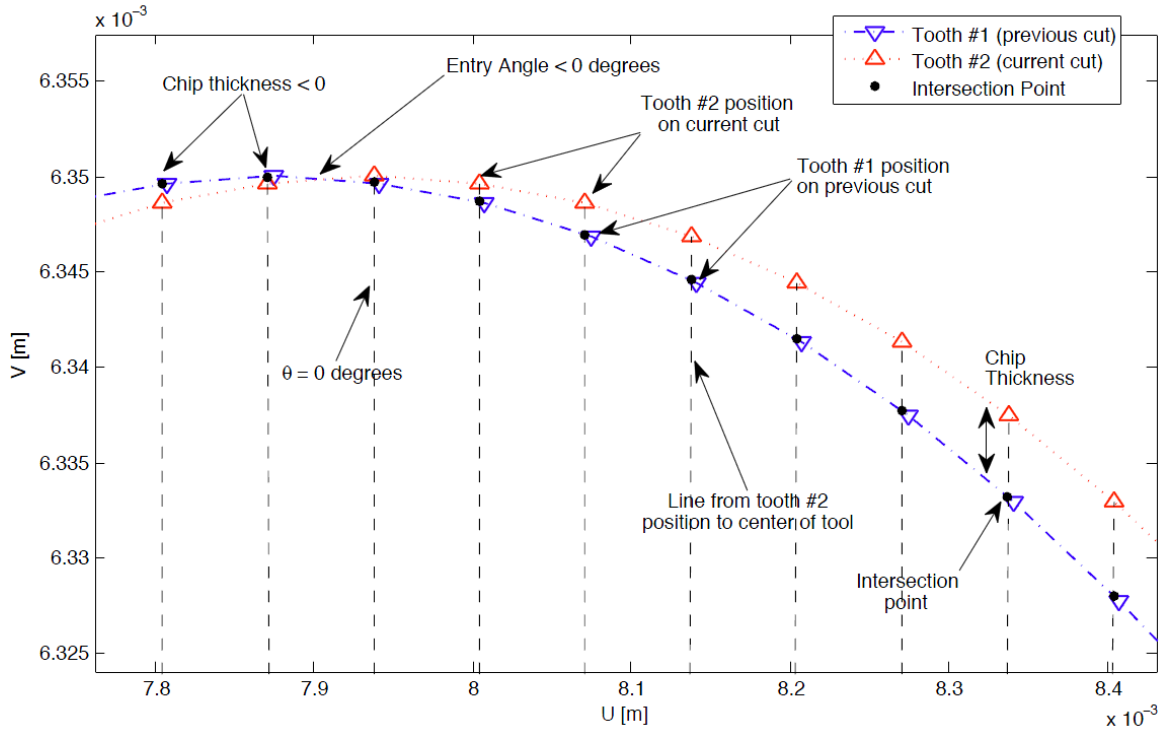


Figure 2.2. Example of finding chip thickness with the numerical model [35].

As mentioned in Section 1.5, a modification was made to the numerical chip thickness model employed in Kennedy [35] to expedite computation. Previously a numerical search was used to determine the distance of every point in a previous tooth path to the current tooth, but this is a problem that can be solved analytically without any numerical search. The current tooth is represented in the model as a radial line, defined by the tool rotation angle and the tooth tip position. If the radial line has slope α and y -intercept β (defined with respect to the tool deflection coordinate axes), the horizontal

position δ_x (along the x -axis) of the point in the radial line nearest to any point (U_i, V_i) in a previous tooth path can be found as

$$\delta_x = \frac{(U_i + \alpha(V_i - \beta))}{1 + \alpha^2}, \quad (2.12)$$

and the vertical position δ_y (along the y -axis) of the same nearest point is

$$\delta_y = \alpha\delta_x + \beta. \quad (2.13)$$

The distance δ between the point (U_i, V_i) and the nearest point on the radial line is, therefore,

$$\delta = \sqrt{(U_i - \delta_x)^2 + (V_i - \delta_y)^2}. \quad (2.14)$$

As mentioned in Section 1.5, using this calculation instead of a numerical search to find the closest point on the radial line allowed milling simulations to run as much as sixteen times as fast (e.g., 3 min instead of 48 min). Not only does this improvement allow the effects of modifying system parameters to be studied more easily through simulations, but it also makes implementation of the numerical chip thickness model in a real-time parameter estimator more feasible.

In the interest of further reducing computational time, the model could also be modified to consider potential intersections of the cutting tooth with only the current

workpiece surface, rather than with the entire historical tooth trajectories, over the selected number of previous revolutions. Even though a limited number of revolutions is considered by the model for any given chip thickness calculation, the step size for these calculations is so small that the computational time required to complete a typical simulation with the numerical chip model can be many minutes. Therefore, for a given chip thickness calculation, reducing the amount of data considered from a couple high-resolution revolutions to a fraction of a revolution (by considering only the current workpiece surface) could reduce the computational cost by several times. Such an approach has been implemented in a similar model in literature [41, 42] but is neglected here because the numerical chip thickness model was found to be unnecessary for the parameter estimation conducted in this study. Nevertheless, the special cases of tool-workpiece intersection that are outlined in [41] (as when a tooth is exiting a cut and does not intersect a previous tooth pass but is still engaged in the workpiece) might also be considered for implementation in this model, regardless of whether the same surface memory approaches are used here.

CHAPTER 3: EQUIPMENT SETUP

3.1. Measuring Tool Deflection

To measure the deflection of the milling tool in the x - and y -directions, two capacitive displacement sensors are mounted near the smooth part of the tool, above its flutes, one along the x -axis and one along the y -axis (Fig. 3.1). These sensors are both connected to a signal conditioning box, which outputs a voltage corresponding to the displacement between the sensor and the tool. A grounding brush touches the tool to provide a voltage reference point for the sensors. The voltage output from the signal conditioner is connected to a National Instruments (NI) PCI 6831 field-programmable gate array (FPGA) which, in turn, is connected to an NI data acquisition card inside a computer. The computer operates LabVIEW ® Real-Time Controller software to collect data and is accessed via Ethernet cable by another computer outside the body of the CNC machining center, also operating LabVIEW ® software. A Terahertz Technologies LT-880 laser tachometer encoder is also mounted beside the smooth part of the tool, slightly above the capacitive sensors, and a piece of masking tape is applied to the tool at an arbitrary angular displacement. The encoder conveys laser light by optical fiber cable to the tool surface and collects reflected light from the tool to return to the tachometer. The tachometer sends a digital voltage pulse to the FPGA upon detecting a significant change in intensity of the returned laser light (as when the tape, or else a gap in the tape, passes by), indicating the start of a new tool revolution. In this way the tool deflection data can be analyzed over discrete numbers of tool revolutions and, if the angular displacement of the tape is known, the absolute angular displacement of the tool can be found at each data

point, allowing a Kalman filter to nearly synchronize the simulated cutting process with the actual cutting process.

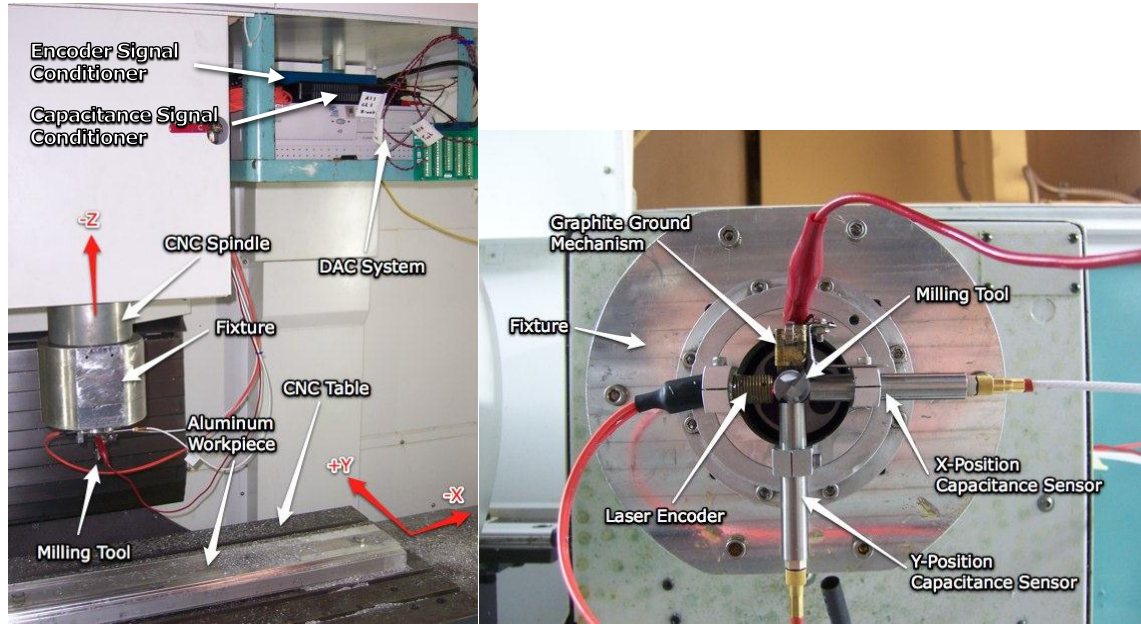


Figure 3.1. Sensor mounting fixture and data acquisition system (left) and bottom view of sensor configuration (right) [35].

All experiments are conducted with a Cincinnati CFV1050^{si} CNC machining center with the ability to move its workpiece table along the x - and y -axes and its spindle along the z -axis. All tools are mounted in the spindle with a TRIBOS-R toolholder, which uses a thermoset plastic to dampen tool vibrations. The toolholder also minimizes tool runout or eccentricity by holding the tool symmetrically, as opposed to using set screws. A hydraulic press must be used to squeeze the toolholder to release the tool.

Because the capacitive sensors are placed above the cutting flutes of the tool, the deflections measured by the sensors do not represent the deflections at the tool tip. Most cutting occurs at or near the tip in this study, due to a relatively low axial depth of cut. In order to accurately calculate chip thickness and chatter behavior at the tip, then, the

measured deflection at the sensor must be multiplied by a constant conversion factor to calculate the deflection at the tip. To determine the value of this conversion factor, the tool was mounted on the milling machine and positioned beside the workpiece with the tip extending 0.1 in below its surface. The tool was then brought against the side of the workpiece and subjected to various static deflection loads. Each load was determined by manually adjusting the workpiece position by a given amount to cause the tool tip to deflect by the same amount. Figure 3.2 shows the measured deflection from the sensor for various tool tip deflections.

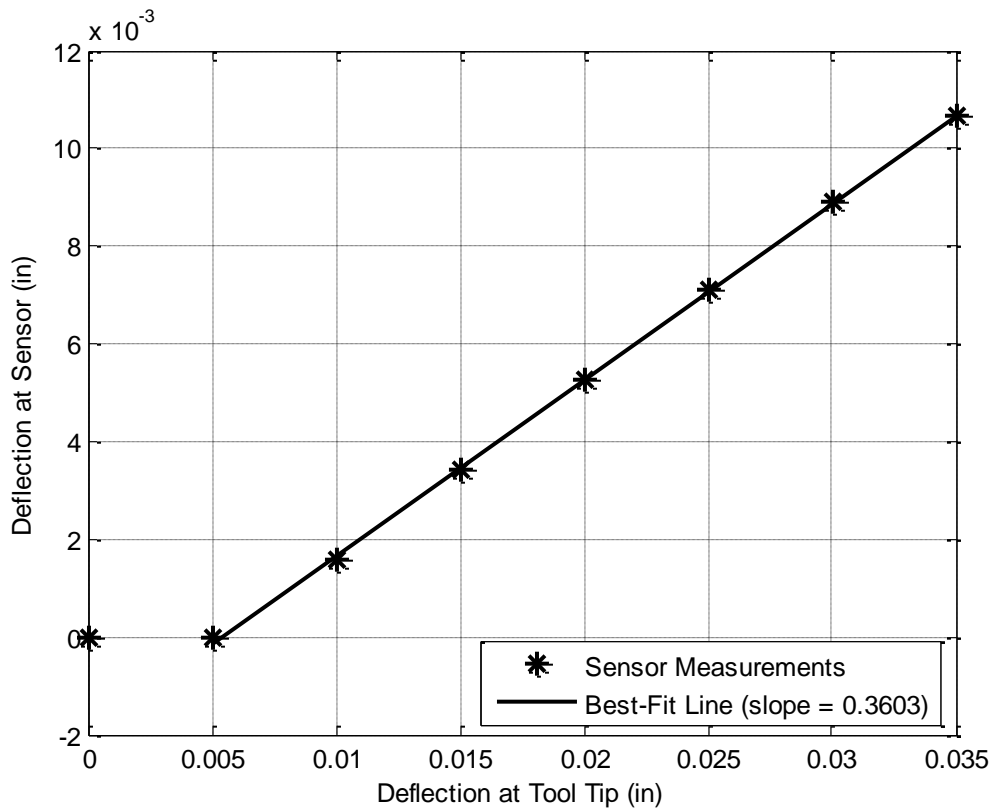


Figure 3.2. Tool deflection measured at sensor given various deflections at tool tip.

Note that the sensor does not measure any deflection until the tool tip has been deflected 0.01 in, which indicates that the tool may not have actually been in contact with

the workpiece until the workpiece had been translated 0.005 in. The slope of the line in Fig. 3.2 gives the inverse of the desired conversion factor, so the conversion factor from the measured deflection to the tip deflection is about 2.78. The data in Fig. 3.2 indicate that there is a linear relationship over small tip deflections between the deflection at the tool tip and the deflection at the sensor, validating the use of a constant conversion factor for determining tip deflections from the measured deflections at the sensor. Unless otherwise noted, the conversion factor found here is used for multiplying all experimental measurements in this study.

To process the tool deflection data required 1) acquiring voltage measurements from the signal processor for the capacitive sensors, 2) multiplying the voltage measurements by a calibration factor (found by measuring the gap between the tool and sensors with a feeler gauge, as in [43]) to find the corresponding deflection values at the sensor, 3) multiplying the deflection values by the conversion factor discussed previously to convert the deflection at the sensor to the deflection at the tool tip, and 4) finding the mean voltage waveform for one non-cutting revolution (i.e., a revolution prior to tool engagement with the workpiece) by averaging data over an integer number of non-cutting revolutions in a one-second sample of data. This mean waveform, which was assumed to be caused by any unbalance, runout (i.e., eccentricity in mounting), and out-of-roundness in the tool, was then rescaled as necessary and subtracted from each revolution of measured tool deflections throughout the entire trial. Subtracting this waveform was necessary both to determine the voltage baseline for the center of tool rotation, from which to calculate voltage differences and corresponding tool deflections throughout the trial, and to determine the mean non-cutting tool contour, which should be removed from

all the deflection data to aid in correlation with simulated tool deflections (which typically assume no unbalance or out-of-roundness, though occasionally runout is included, as in Sections 5.1 and 7.1). Unless otherwise noted, all experimental data used in this study has been processed as described here.

3.2. Measuring Cutting Forces

To determine the cutting force coefficients of various tool-workpiece combinations, first the cutting forces were measured with a Kistler 9124B rotating multicomponent dynamometer. A stator relayed measurements from the dynamometer to a Kistler 5223B signal conditioner, which had five outputs: force along x -axis, force along y -axis, force along z -axis, moment about z -axis, and a zero count, which pulsed to indicate the onset of a new revolution. Each signal was represented as a voltage, and the voltages were conveyed to a feed-through signal conditioner connected to a data acquisition card in a laptop computer equipped with LabVIEW®.

The x - and y -axes of the dynamometer were rotating while the machine was slot-milling (full radial immersion) with a two-fluted tool (see Fig. 3.3), so the average force along each axis over one revolution was assumed to be zero. This assumption is based on the belief that each tooth experiences nearly the same forces as the other as it cuts, so the forces during one tooth path approximately balance the forces in the opposite direction on the next tooth path. Hence, the mean voltage offsets in the three force measurement channels were determined by averaging the voltage in each channel over one revolution. These offsets were subtracted from their respective channels, and each signal was multiplied by the sensitivity of the dynamometer for that measurement, where the

sensitivities were determined experimentally by calibration of the dynamometer with known forces and moments (as in [43]).



Figure 3.3. Spindle-mounted dynamometer while slot-milling.

Because the x - and y -axes of the dynamometer rotated with it, the force measurements along these axes had to be converted via coordinate transformation into the tangential and radial forces acting on the tool, which required finding the angle of the dynamometer with respect to the cutting teeth of the tool. Given that slot-milling means the full radius of the tool is engaged in material, a two-fluted tool theoretically always has one tooth cutting (unless vibration has caused the tool to leave contact with the material). As one tooth leaves the cut and the other tooth enters, the theoretical tangential and radial forces acting on the tool are zero (unless vibration has caused the tool to engage the material unexpectedly). Furthermore, the forces acting along the x - and y -axes of the dynamometer must be zero. Therefore, either of the two points in a revolution at which the forces along the x - and y -axes are nearly zero (simultaneously) can serve as a

reference point for angular displacement, in order to determine the angle θ_{dyn} of the dynamometer with respect to the cutting teeth of the tool. In practice, the forces do not always go to zero simultaneously, but the angular displacement at which their functions intersect can serve as an approximation. Using the sign convention that positive indicates that the dynamometer zero-count occurs before (or leads) the selected intersection and negative indicates that the dynamometer zero-count occurs after (or lags) the selected intersection, the angle θ_{dyn} can be found from the amount of time elapsed from the zero-count to the intersection, as a fraction of the time elapsed from the zero-count to the next zero-count (one revolution). Then the tangential and radial cutting forces experienced by the active cutting tooth can be found as

$$F_t(t) = |F_x(t) \cos \theta_{dyn} + F_y(t) \sin \theta_{dyn}| \quad (3.1)$$

$$F_r(t) = |-F_x(t) \sin \theta_{dyn} + F_y(t) \cos \theta_{dyn}| \quad (3.2)$$

where $F_t(t)$ and $F_r(t)$ are the tangential and radial cutting forces applied to the active tooth at time t (N), and $F_x(t)$ and $F_y(t)$ are the forces along the x - and y -axes of the dynamometer at time t (N). Note that θ_{dyn} (rad) remains constant for all t . Absolute values are used in Eqs. (3.1)-(3.2) to find the forces applied to the active tooth in the positive radial and tangential directions, though $F_x(t)$ and $F_y(t)$ vary positively and negatively over each revolution. Ensuring that $F_t(t)$ and $F_r(t)$ are positive allows the average magnitudes of the tangential and radial forces to be found over one revolution

which, in turn, aids in finding the cutting force coefficients. Note also that averaging the forces over one revolution reduces the effect of any tool runout on the measured forces.

According to Altintas [17], cutting forces may be expressed as linear functions of chip thickness (see also Eqs. (2.1)-(2.2)), as

$$F_{tp}(\theta_p) = K_{tc}bw_p(\theta_p) + K_{te}b \quad (3.3)$$

$$F_{rp}(\theta_p) = K_{rc}bw_p(\theta_p) + K_{re}b \quad (3.4)$$

where K_{tc} and K_{rc} are the first-order tangential and radial cutting coefficients (N/m²), and K_{te} and K_{re} are the zeroth-order tangential and radial cutting coefficients (N/m), also called edge coefficients. If $w_p(\theta_p)$ is approximated by the static chip thickness term of the traditional chip thickness model (Eq. (2.7)), $h \sin \theta_p$, then for a two-fluted tool (all tools in this study bear two flutes), two chips are produced in one revolution, and the average magnitudes of the tangential and radial cutting forces over one revolution can be found by integrating Eqs. (3.3)-(3.4) as

$$\bar{F}_t = \frac{1}{2\pi} \int_0^{2\pi} |K_{tc}b(2h \sin \theta) + K_{te}b| d\theta = \frac{4bK_{tc}}{\pi} h + bK_{te} \quad (3.5)$$

$$\bar{F}_r = \frac{1}{2\pi} \int_0^{2\pi} |K_{rc}b(2h \sin \theta) + K_{re}b| d\theta = \frac{4bK_{rc}}{\pi} h + bK_{re} \quad (3.6)$$

where \bar{F}_t and \bar{F}_r are the average magnitudes of the tangential and radial forces over one revolution (N), and θ has been substituted for θ_p as the absolute angular displacement of the entire tool (rad). The chip thickness has been doubled because the average force over the entire revolution is desired (so that runout effects might be minimized), which means that the workpiece feed is advanced twice as far as for a single tooth (where h is the feed per tooth). Note from the right-hand sides of Eqs. (3.5)-(3.6) that these average-magnitude forces are linear functions of feed rate h . Hence, these average magnitudes were found experimentally at several different feed rates (0.025, 0.050, 0.075, 0.100, 0.125, and 0.150 mm per tooth) for each tool-workpiece combination for which cutting coefficients were desired, and then slopes were found for the best-fit lines through the average-magnitude forces as functions of feed rate, such that

$$\bar{F}_t \cong \bar{F}_{tc}h + \bar{F}_{te} \quad (3.7)$$

$$\bar{F}_r \cong \bar{F}_{rc}h + \bar{F}_{re} \quad (3.8)$$

where \bar{F}_{tc} and \bar{F}_{rc} are the slopes of the best-fit lines representing the average-magnitude tangential and radial forces as functions of feed (N/m), and \bar{F}_{te} and \bar{F}_{re} are the vertical intercepts of the best-fit lines (N). By comparing the best-fit lines in Eqs. (3.7)-(3.8) with the linear functions of feed in Eqs. (3.5)-(3.6), the relationships for evaluating the cutting coefficients are derived as

$$K_{tc} = \frac{\pi \bar{F}_{tc}}{4b} \quad (3.9)$$

$$K_{te} = \frac{\bar{F}_{te}}{b} \quad (3.10)$$

$$K_{rc} = \frac{\pi \bar{F}_{rc}}{4b} \quad (3.11)$$

$$K_{re} = \frac{\bar{F}_{re}}{b} \quad (3.12)$$

Note that for this study, the edge coefficients K_{te} and K_{re} are neglected in the force model (see Section 2.1 and Eqs. (2.1)-(2.2)) for simplicity and because of the relatively small magnitude of the constant terms in Eqs. (3.7)-(3.8) with respect to the linear terms. Therefore, the linear cutting force coefficients K_{tc} and K_{rc} are denoted as K_t and K_r , respectively, when they appear in the force model throughout this paper (as in Eqs. (2.1)-(2.2)).

CHAPTER 4: FILTER DESIGN

4.1. Overview of Kalman Filters

The original Kalman filter, introduced in 1960 [44], has been employed to recursively update estimates of the states of a linear dynamic system based on noisy measurements. The filter operates by comparing an internal model of the system dynamics, which estimates the values of the states, to external measurements that are linearly related to one or more states. The external measurements are assumed to include Gaussian noise, and the filter is derived to optimally remove this noise. Parameters of the filter can be tuned to initially give greater weight to either the predictions of the internal model or to the external measurements when estimating state values. The estimated variances of the process noise and measurement noise are also updated on each iteration to determine whether to place more trust on the internal model or external measurements.

Though the Kalman filter performs optimally for linear systems with Gaussian noise, many dynamic systems are nonlinear, including the milling system in this study. Modal parameters serve as coefficients of position and velocity states, so if modal parameters are being estimated as states themselves, the system equations include products of the states, making the system nonlinear. Similarly, the system equations include products of the cutting force coefficients with chip thickness, which serves as a system input, so if cutting force coefficients are estimated as states instead of modal parameters, the system remains nonlinear.

To accommodate nonlinear systems, the Extended Kalman Filter (EKF) was developed, which uses a first-order Taylor series to linearize the system about current

state estimates. The EKF has been applied to the nonlinear problem of estimating modal parameters from simulated or experimental tool deflection measurements [35] and has been shown in some circumstances to give estimates that are within a few percent of the values found experimentally by impulse-response test. Highly nonlinear systems require small time steps, which are computationally expensive, in order for the EKF to accurately reflect nonlinearities with a first-order approximation of the system. To more accurately estimate states and parameters in nonlinear systems, various alternative filters have been proposed, such as the Unscented Kalman Filter (UKF) [45-47], higher-order versions of the EKF (such as [48]), divided-difference filters [49], quadrature Kalman filters [50], [51], cubature Kalman filters [52], and many others. Many similarities exist among the different filters, especially in their attempts to eliminate the need to derive Taylor terms (Jacobian, Hessian, etc.), to improve numerical stability, and to increase computational efficiency. There is some debate as to which filter performs best and under what conditions (e.g., see [53]), but the UKF has received much attention and has been demonstrated to be more accurate than the EKF in a number of nonlinear problems. Variants of the UKF, including the Square-Root Unscented Kalman Filter (SR-UKF) [54], have also been developed to improve numerical stability, reduce computational complexity, and guarantee that the state covariance matrices are positive semi-definite. Though future research might consider using these alternative filters for parameter estimation, the EKF is employed in the following chapters for its simplicity of implementation and because of confidence in the EKF due to its use in previous milling literature (e.g., Kennedy [35]).

This chapter addresses the problem of designing a filter to estimate system parameters relevant to chatter stability. Section 4.2 discusses the relevance of modal parameters and cutting force coefficients to chatter stability. Sections 4.3 and 4.4 address the use of an EKF to estimate modal parameters (as in [35]) and cutting force coefficients, respectively. Section 4.5 considers the observability of the systems in Sections 4.3 and 4.4.

4.2. Effect of Modal Parameters and Cutting Coefficients on Stability

To understand why an EKF should be used to estimate modal parameters or cutting force coefficients, it is important to know how these parameters affect the chatter stability boundaries of the tool-workpiece system. This analysis can be simply conducted by modifying each parameter in turn and recalculating the stability boundary by using Time Finite Element Analysis (TFEA) (see [11] for a discussion of TFEA).

Figure 4.1 gives an example of the effect of modifying the modal parameters, one at a time, on the stability boundaries calculated by TFEA. Figure 4.2 shows the effect of scaling all three modal parameters at once on the stability boundaries calculated by TFEA for the same system. These examples use a tool diameter of 0.5 in (12.7 mm) and a radial depth of cut of 0.015 in (0.382 mm).

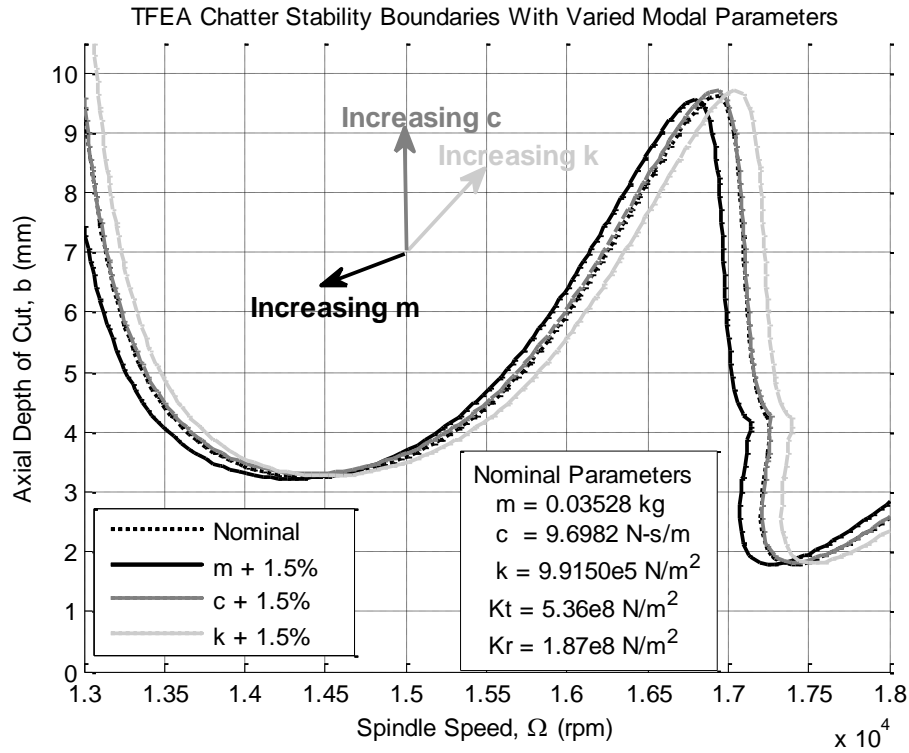


Figure 4.1. Example in Kennedy [35] of varying each modal parameter individually to affect chatter stability boundaries, as calculated with TFEA.

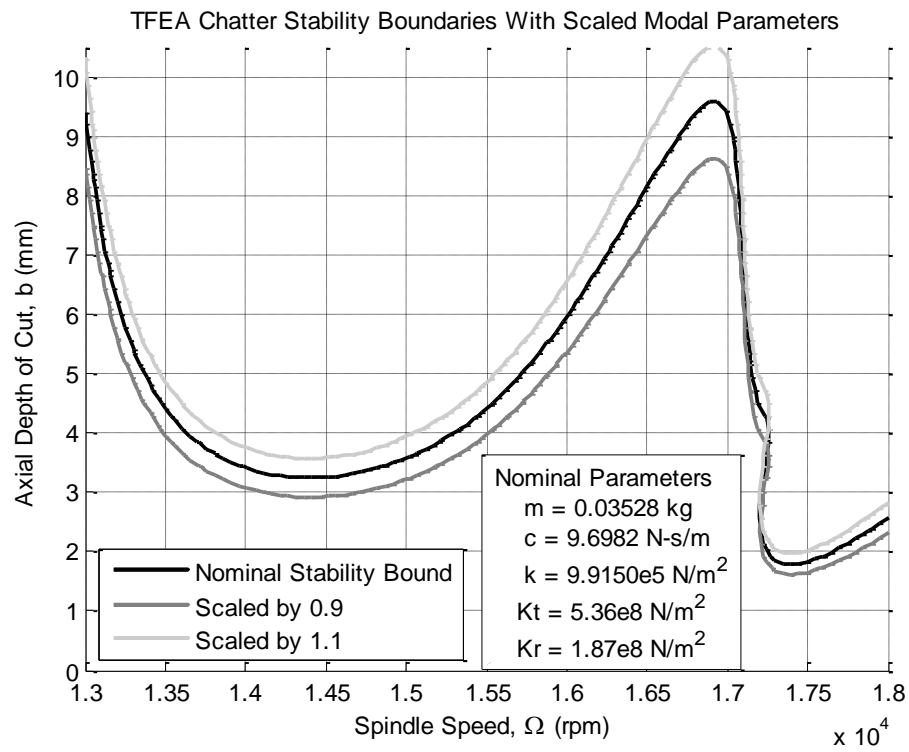


Figure 4.2. Example of scaling all three modal parameters by the same factor to affect chatter stability boundaries, as calculated with TFEA.

Because the tool-workpiece system is modeled as a simple two-degree-of-freedom mass-spring-damper system (Eqs. (2.5)-(2.6)), scaling all three modal parameters at once by a given factor is equivalent to dividing the forcing function along that axis by the same factor, which is also equivalent to dividing the tangential and radial cutting force coefficients by that factor, according to Eqs. (2.3)-(2.4). Figure 4.3 shows the effect of varying the two cutting force coefficients individually on the stability boundary of the same nominal system as in Figs. 4.1-4.2. Note that Fig. 4.2 shows primarily a vertical displacement in the stability boundaries when all the modal parameters are scaled at once, which is effectively scaling the two cutting force coefficients at once. In Fig. 4.3, however, it is shown that varying the cutting force coefficients individually allows the stability boundaries to be shifted vertically and horizontally.

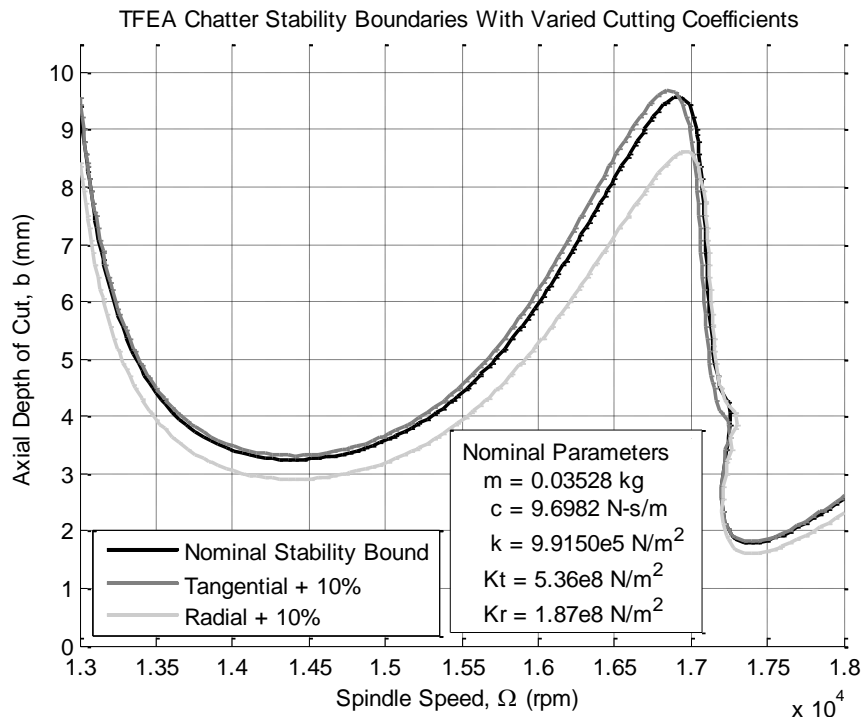


Figure 4.3. Example of varying each cutting coefficient individually to affect chatter stability boundaries, as calculated with TFEA.

Figure 4.3 does not exhibit the same magnitude of horizontal displacement of the boundaries as Fig. 4.1, even though the cutting force coefficients have been varied more severely in Fig. 4.3 than the modal parameters in Fig. 4.1. It remains to be seen, then, whether varying the cutting force coefficients provides as much freedom to modify the stability boundaries as varying the modal parameters. Even if the coefficients do provide reduced boundary mobility, they may provide enough freedom to accommodate realistic cutting scenarios, and the benefit of having an observable system (see Section 4.5 for how to check observability, guaranteeing convergence of the coefficient estimates) may outweigh the cost of having reduced boundary mobility.

4.3. Using an EKF to Estimate Modal Parameters

Kennedy [35] assumes the modal parameters of the tool-workpiece dynamic system are equal along both axes (i.e., $m_x = m_y$, $c_x = c_y$, and $k_x = k_y$) and proceeds to implement an EKF to estimate the deflection and velocity of the tool along the x -axis (x and \dot{x}) and the three modal parameters (m_x , c_x , and k_x) based on measurements of the tool deflection along the x -axis. For simplicity Kennedy omits measurements of tool deflection along the y -axis from the EKF, affecting the observability of the system as will be discussed in Section 4.5. The EKF state and measurement update equations are defined in Kennedy as

$$\mathbf{x}_k = f_{k-1}(\mathbf{x}_{k-1}, \mathbf{u}_{k-1}, \mathbf{w}_{k-1}) \quad (4.1)$$

$$\mathbf{y}_k = h_k(\mathbf{x}_k, \mathbf{v}_k) \quad (4.2)$$

where \mathbf{x}_k is the state vector and \mathbf{y}_k is the measurement vector on iteration k of the filtering process, \mathbf{u}_{k-1} and \mathbf{w}_{k-1} are the input vector and process noise vector on the previous iteration, \mathbf{v}_k is the measurement noise vector, and f_{k-1} and h_k are the process and measurement update functions, respectively. The elements of \mathbf{x}_k represent the states on iteration k where $x_{1,k}$ is tool deflection (x), $x_{2,k}$ is tool velocity (\dot{x}), $x_{3,k}$ is m_x , $x_{4,k}$ is c_x , and $x_{5,k}$ is k_x . For a given time step T (sec), the updates are given as

$$\mathbf{x}_k = \begin{bmatrix} x_{2,k-1}T + x_{1,k-1} \\ \frac{T}{x_{3,k-1}} \left(-x_{2,k-1}x_{4,k-1} - x_{1,k-1}x_{5,k-1} + u_{x,k-1} + w_{x,k-1} \right) + x_{2,k-1} \\ w_{M,k-1}T + x_{3,k-1} \\ w_{C,k-1}T + x_{4,k-1} \\ w_{K,k-1}T + x_{5,k-1} \end{bmatrix} \quad (4.3)$$

$$\mathbf{y}_k = \mathbf{H}_k \mathbf{x}_k + v_{x,k} = x_{1,k} + v_{x,k} \quad (4.4)$$

where $u_{x,k-1}$ is the system input or cutting force along the x -axis on the previous iteration, and $w_{x,k-1}$, $w_{M,k-1}$, $w_{C,k-1}$, and $w_{K,k-1}$ are the process noise variables added to the tool deflection, modal mass, modal damping, and modal stiffness, respectively. Kennedy maintains the values of these noise variables at zero. \mathbf{H}_k is a partial derivative matrix that is defined later, and $v_{x,k}$ is the measurement noise added to the measured tool deflection along the x -axis. This noise variable is also maintained at zero.

A discrete EKF uses the following equations, described by Simon [55]:

$$\hat{\mathbf{x}}_k^- = f_{k-1}(\hat{\mathbf{x}}_{k-1}^+, \mathbf{u}_{k-1}, \mathbf{0}) \quad (4.5)$$

$$\mathbf{P}_k^- = \mathbf{F}_{k-1} \mathbf{P}_k^+ \mathbf{F}_{k-1}^T + \mathbf{L}_{k-1} \mathbf{Q}_{k-1} \mathbf{L}_{k-1}^T \quad (4.6)$$

$$\mathbf{K}_k = \mathbf{P}_k^- \mathbf{H}_k^T (\mathbf{H}_k \mathbf{P}_k^- \mathbf{H}_k^T + \mathbf{M}_k \mathbf{R}_k \mathbf{M}_k^T)^{-1} \quad (4.7)$$

$$\hat{\mathbf{x}}_k^+ = \hat{\mathbf{x}}_k^- + \mathbf{K}_k (\mathbf{y}_k - \mathbf{H}_k \hat{\mathbf{x}}_k^-) \quad (4.8)$$

$$\mathbf{P}_k^+ = (\mathbf{I} - \mathbf{K}_k \mathbf{H}_k) \mathbf{P}_k^- \quad (4.9)$$

where $\hat{\mathbf{x}}_k^-$ and $\hat{\mathbf{x}}_k^+$ are the *a priori* (or previous) and *a posteriori* (or updated) state estimate vectors on iteration k , respectively, \mathbf{P}_k^- and \mathbf{P}_k^+ are the *a priori* and *a posteriori* covariance matrices of the estimation error on iteration k , respectively, \mathbf{K}_k is the Kalman filter gain matrix on iteration k , and \mathbf{F}_{k-1} , \mathbf{L}_{k-1} , \mathbf{H}_k , and \mathbf{M}_k are various matrix partial derivatives that are defined later (on iterations $k-1$, $k-1$, k , and k , respectively). \mathbf{Q}_{k-1} is the process noise covariance matrix on iteration $k-1$, and \mathbf{R}_k is the measurement noise covariance matrix on iteration k . Note that a superscript T indicates the matrix transpose operation (not to be confused with the time step T), and \mathbf{I} denotes the identity matrix with dimensions matching $\mathbf{K}_k \mathbf{H}_k$. Finally, a superscript -1 indicates the matrix inverse operation, which should be implemented in a numerically efficient manner, as with the MATLAB backslash operator. The matrix partial derivatives employed in Eqs. (4.5)-(4.9) are defined for this application in Kennedy [35] as

$$\mathbf{F}_{k-1} = \frac{\partial f_{k-1}}{\partial \mathbf{x}} \Big|_{\hat{\mathbf{x}}_{k-1}^+} = \begin{bmatrix} 1 & T & 0 & 0 & 0 \\ -\frac{\hat{x}_{5,k-1}^+ T}{\hat{x}_{3,k-1}^+} & 1 - \frac{\hat{x}_{4,k-1}^+ T}{\hat{x}_{3,k-1}^+} & F_{3,3} & -\frac{\hat{x}_{2,k-1}^+ T}{\hat{x}_{3,k-1}^+} & -\frac{\hat{x}_{1,k-1}^+ T}{\hat{x}_{3,k-1}^+} \\ 0 & 0 & 1 & 0 & 0 \\ 0 & 0 & 0 & 1 & 0 \\ 0 & 0 & 0 & 0 & 1 \end{bmatrix} \quad (4.10)$$

$$\mathbf{L}_{k-1} = \frac{\partial f_{k-1}}{\partial \mathbf{w}} \Big|_{\hat{\mathbf{x}}_{k-1}^+} = \begin{bmatrix} 0 & 0 & 0 & 0 \\ \frac{T}{\hat{x}_{3,k-1}^+} & 0 & 0 & 0 \\ 0 & T & 0 & 0 \\ 0 & 0 & T & 0 \\ 0 & 0 & 0 & T \end{bmatrix} \quad (4.11)$$

$$\mathbf{H}_k = \frac{\partial h_k}{\partial \mathbf{x}} \Big|_{\hat{\mathbf{x}}_k^-} = [1 \ 0 \ 0 \ 0 \ 0] \quad (4.12)$$

$$\mathbf{M}_k = \frac{\partial h_k}{\partial v} \Big|_{\hat{\mathbf{x}}_k^-} = [1] \quad (4.13)$$

where $\hat{x}_{1,k-1}^+$ and similar expressions indicate respective elements of the *a posteriori* (updated) state estimate vector, and $F_{3,3}$ is defined as

$$F_{3,3} = \frac{T}{(\hat{x}_{3,k-1}^+)^2} (\hat{x}_{2,k-1}^+ \hat{x}_{4,k-1}^+ + \hat{x}_{1,k-1}^+ \hat{x}_{5,k-1}^+ - u_{x,k-1} - w_{x,k-1}) \quad (4.14)$$

Per Kennedy's model, the noise vector for process noise, \mathbf{w} , holds four variables (noise in tool deflection and noise in each modal parameter), so the covariance matrix of process noise, \mathbf{Q}_k , is a 4×4 matrix. The noise vector for measurement noise, \mathbf{v} , holds

only one element (i.e., the noise in tool deflection along the x -axis). The covariance matrix of measurement noise, \mathbf{R}_k , therefore, has only one element as well. These matrices affect the weight applied to the internal model and the external measurements of the EKF in estimating state values. Decreasing process noise covariance indicates that the internal model of the EKF is more accurate and causes the EKF to give greater weight to the estimated states found by its internal model. Decreasing measurement noise covariance indicates that the measurements are more accurate and causes the EKF to give greater weight to simulated or experimental tool deflection measurements. The EKF operates iteratively as many times as desired, propagating the estimates by time step T on each iteration.

Sections 1.5 and 4.5 discuss the observability of the EKF estimating modal parameters. Given only x -axis tool deflection measurements, only one modal parameter is observable, which means the EKF estimate is guaranteed to converge for only one modal parameter. Kennedy discusses this fact but holds that, in practice, all three estimates converge. In the interest of developing a robust parameter estimation system, however, guaranteed convergence is desired such that the EKF can be applied to a wide variety of tool-workpiece combinations and cutting conditions. One approach to improving the observability of the system is to allow the EKF to consider y -axis tool deflection measurements as well as those along the x -axis. By adding another measurement, the EKF has more information on which to base its parameter estimates. Now two modal parameters can be observed, guaranteeing the convergence of EKF estimates of these parameters. Though only two modal parameters are observable, the two-measurement EKF is presented here as estimating all three parameters in order to

remain as general as possible. Any one or more parameter estimates can be removed from the EKF and replaced with a constant.

To modify the EKF to include y -axis tool deflection measurements, \mathbf{x}_k in Eq. (4.1) is revised to include tool deflection along the y -axis (y) and tool velocity along the y -axis (\dot{y}). Hence, the elements of \mathbf{x}_k are defined such that $x_{1,k}$ is tool deflection along the x -axis, (x), $x_{2,k}$ is tool velocity along the x -axis (\dot{x}), $x_{3,k}$ is tool deflection along the y -axis (y), $x_{4,k}$ is tool velocity along the y -axis (\dot{y}), $x_{5,k}$ is m_x , $x_{6,k}$ is c_x , and $x_{7,k}$ is k_x . For simplicity of estimation, the modal parameters in the x -direction are assumed to be the same as those along the y -axis. For a given time step T (sec), the update equations (Eqs. (4.3)-(4.4)) are rewritten as

$$\mathbf{x}_k = \begin{bmatrix} x_{2,k-1}T + x_{1,k-1} \\ \frac{T}{x_{5,k-1}} \left(-x_{2,k-1}x_{6,k-1} - x_{1,k-1}x_{7,k-1} + u_{x,k-1} + w_{x,k-1} \right) + x_{2,k-1} \\ x_{4,k-1}T + x_{3,k-1} \\ \frac{T}{x_{5,k-1}} \left(-x_{4,k-1}x_{6,k-1} - x_{3,k-1}x_{7,k-1} + u_{y,k-1} + w_{y,k-1} \right) + x_{4,k-1} \\ w_{M,k-1}T + x_{5,k-1} \\ w_{C,k-1}T + x_{6,k-1} \\ w_{K,k-1}T + x_{7,k-1} \end{bmatrix} \quad (4.15)$$

$$\mathbf{y}_k = \mathbf{H}_k \mathbf{x}_k + \mathbf{v}_k = \begin{bmatrix} x_{1,k} + v_{x,k} \\ x_{3,k} + v_{y,k} \end{bmatrix} \quad (4.16)$$

where $u_{y,k-1}$ is the system input or cutting force along the y -axis on the previous iteration, $w_{y,k-1}$ is the process noise variable added to the tool deflection along the y -

axis, \mathbf{v}_k is the measurement noise vector, and $v_{y,k}$ is the measurement noise added to the measured tool deflection along the y-axis. This noise variable is maintained at zero.

The standard equations for a discrete EKF (Eqs. (4.5)-(4.9)) remain the same for the two-measurement version, but the matrix partial derivatives employed in those equations (Eqs. (4.10)-(4.13)) are revised to accommodate the new measurement. The new matrix partial derivatives are defined as

$$\mathbf{F}_{k-1} = \left. \frac{\partial f_{k-1}}{\partial \mathbf{x}} \right|_{\hat{\mathbf{x}}_{k-1}^+} = \begin{bmatrix} 1 & T & 0 & 0 & 0 & 0 & 0 \\ -\frac{\hat{x}_{7,k-1}^+}{\hat{x}_{5,k-1}^+} T & 1 - \frac{\hat{x}_{6,k-1}^+}{\hat{x}_{5,k-1}^+} T & 0 & 0 & F_{2,5} & -\frac{\hat{x}_{2,k-1}^+}{\hat{x}_{5,k-1}^+} T & -\frac{\hat{x}_{1,k-1}^+}{\hat{x}_{5,k-1}^+} T \\ 0 & 0 & 1 & T & 0 & 0 & 0 \\ 0 & 0 & -\frac{\hat{x}_{7,k-1}^+}{\hat{x}_{5,k-1}^+} T & 1 - \frac{\hat{x}_{6,k-1}^+}{\hat{x}_{5,k-1}^+} T & F_{4,5} & -\frac{\hat{x}_{4,k-1}^+}{\hat{x}_{5,k-1}^+} T & -\frac{\hat{x}_{3,k-1}^+}{\hat{x}_{5,k-1}^+} T \\ 0 & 0 & 0 & 0 & 1 & 0 & 0 \\ 0 & 0 & 0 & 0 & 0 & 1 & 0 \\ 0 & 0 & 0 & 0 & 0 & 0 & 1 \end{bmatrix} \quad (4.17)$$

$$\mathbf{L}_{k-1} = \left. \frac{\partial f_{k-1}}{\partial \mathbf{w}} \right|_{\hat{\mathbf{x}}_{k-1}^+} = \begin{bmatrix} 0 & 0 & 0 & 0 & 0 \\ \frac{T}{\hat{x}_{5,k-1}^+} & 0 & 0 & 0 & 0 \\ 0 & 0 & 0 & 0 & 0 \\ 0 & \frac{T}{\hat{x}_{5,k-1}^+} & 0 & 0 & 0 \\ 0 & 0 & T & 0 & 0 \\ 0 & 0 & 0 & T & 0 \\ 0 & 0 & 0 & 0 & T \end{bmatrix} \quad (4.18)$$

$$\mathbf{H}_k = \left. \frac{\partial h_k}{\partial \mathbf{x}} \right|_{\hat{\mathbf{x}}_k^-} = \begin{bmatrix} 1 & 0 & 0 & 0 & 0 & 0 & 0 \\ 0 & 0 & 1 & 0 & 0 & 0 & 0 \end{bmatrix} \quad (4.19)$$

$$\mathbf{M}_k = \left. \frac{\partial h_k}{\partial \mathbf{v}} \right|_{\hat{\mathbf{x}}_k^-} = \begin{bmatrix} 1 & 0 \\ 0 & 1 \end{bmatrix} \quad (4.20)$$

where $\hat{x}_{1,k-1}^+$ and similar expressions indicate respective elements of the *a posteriori* (updated) state estimate vector, and $F_{2,5}$ and $F_{4,5}$ are defined as

$$F_{2,5} = \frac{T}{(\hat{x}_{5,k-1}^+)^2} (\hat{x}_{2,k-1}^+ \hat{x}_{6,k-1}^+ + \hat{x}_{1,k-1}^+ \hat{x}_{7,k-1}^+ - u_{x,k-1} - w_{x,k-1}) \quad (4.21)$$

$$F_{4,5} = \frac{T}{(\hat{x}_{5,k-1}^+)^2} (\hat{x}_{4,k-1}^+ \hat{x}_{6,k-1}^+ + \hat{x}_{3,k-1}^+ \hat{x}_{7,k-1}^+ - u_{y,k-1} - w_{y,k-1}) \quad (4.22)$$

Now the noise vector for process noise, \mathbf{w} , holds five variables (noise in tool deflection along each axis and noise in each modal parameter), so the covariance matrix of process noise, \mathbf{Q}_k , is a 5×5 matrix. The noise vector for measurement noise, \mathbf{v} , holds two elements (i.e., the noise in tool deflection along each axis). The covariance matrix of measurement noise, \mathbf{R}_k , therefore, is a 2×2 matrix.

4.4. Using an EKF to Estimate Cutting Force Coefficients

As discussed in Section 1.5, an EKF can be used to estimate cutting force coefficients instead of modal parameters, reducing the number of parameters to estimate from three to two (in addition to the system states of tool deflection and velocity). This modification has the advantage that now, if measurements of the tool deflection along the y-axis are also considered by the EKF, the system can be fully observed (see Section 4.5).

Meanwhile, similar to using three modal parameter estimates, information about chatter stability boundary variations can be found by estimating two cutting force coefficients. The new approach may characterize the tool-workpiece dynamic system in a manner equivalent to modal parameter estimation. The effects of modal parameters and cutting force coefficients on chatter stability boundaries are examined in Section 4.2. To modify the EKF to estimate cutting force coefficients instead of modal parameters requires redefining \mathbf{x}_k from Eq. (4.1). To make the cutting force coefficients observable, measurements are included along both the x - and y -axes, but the EKF can also be implemented with measurements along only one axis. The elements of \mathbf{x}_k are defined such that $x_{1,k}$ is tool deflection along the x -axis (x), $x_{2,k}$ is tool velocity along the x -axis (\dot{x}), $x_{3,k}$ is tool deflection along the y -axis (y), $x_{4,k}$ is tool velocity along the y -axis (\dot{y}), $x_{5,k}$ is K_t , and $x_{6,k}$ is K_r . For a given time step T (sec), the EKF update equations (compare Eqs. (4.3)-(4.4) and Eqs. (4.15)-(4.16)) are written as

$$\mathbf{x}_k = \begin{bmatrix} x_{2,k-1}T + x_{1,k-1} \\ \frac{T}{m_x}(-x_{2,k-1}c_x - x_{1,k-1}k_x + F_{x,k-1} + w_{x,k-1}) + x_{2,k-1} \\ x_{4,k-1}T + x_{3,k-1} \\ \frac{T}{m_y}(-x_{4,k-1}c_y - x_{3,k-1}k_y + F_{y,k-1} + w_{y,k-1}) + x_{4,k-1} \\ w_{K_t,k-1}T + x_{5,k-1} \\ w_{K_r,k-1}T + x_{6,k-1} \end{bmatrix} \quad (4.23)$$

$$\mathbf{y}_k = \mathbf{H}_k \mathbf{x}_k + \mathbf{v}_k = \begin{bmatrix} x_{1,k} + v_{x,k} \\ x_{3,k} + v_{y,k} \end{bmatrix} \quad (4.24)$$

where $w_{K_t, k-1}$ and $w_{K_r, k-1}$ are the process noise variables added to the tangential and radial cutting coefficients, respectively. The values of these noise variables are maintained at zero. Note that, for simplicity, the modal parameters are assumed to be equal along the x - and y -axes. Also note that in Section 4.3 the system inputs $u_{x, k-1}$ and $u_{y, k-1}$ represented cutting forces along the x - and y -axes, respectively. Now the system input $u_{p, k-1}$ is chip thickness for each tooth p , and the previous inputs $u_{x, k-1}$ and $u_{y, k-1}$ have been renamed $F_{x, k-1}$ and $F_{y, k-1}$, where these forces are evaluated per Eqs. (2.3) and (2.4) except now in discrete time steps. The tangential and radial cutting forces (Eqs. (2.1) and (2.2)), which appear in Eqs. (2.3) and (2.4), are now evaluated as products of the cutting force coefficient estimates and the chip thickness input, as $x_{5, k-1} b u_{p, k-1}^\gamma$ and $x_{6, k-1} b u_{p, k-1}^\gamma$, respectively (where b is axial depth of cut and γ is still assumed to equal one).

As with the EKFs in Section 4.3, the standard update equations for a discrete EKF are still Eqs. (4.5)-(4.9), but the matrix partial derivatives employed in those equations (Eqs. (4.10)-(4.13) or Eqs. (4.17)-(4.20)) are revised to accommodate the cutting force coefficients. The new matrix partial derivatives are defined as

$$\mathbf{F}_{k-1} = \left. \frac{\partial f_{k-1}}{\partial \mathbf{x}} \right|_{\hat{\mathbf{x}}_{k-1}^+} = \begin{bmatrix} 1 & T & 0 & 0 & 0 & 0 \\ -\frac{k_x}{m_x} T & 1 - \frac{c_x}{m_x} T & 0 & 0 & \frac{\partial \dot{x}}{\partial K_t} & \frac{\partial \dot{x}}{\partial K_r} \\ 0 & 0 & 1 & T & 0 & 0 \\ 0 & 0 & -\frac{k_y}{m_y} T & 1 - \frac{c_y}{m_y} T & \frac{\partial \dot{y}}{\partial K_t} & \frac{\partial \dot{y}}{\partial K_r} \\ 0 & 0 & 0 & 0 & 1 & 0 \\ 0 & 0 & 0 & 0 & 0 & 1 \end{bmatrix} \quad (4.25)$$

$$\mathbf{L}_{k-1} = \left. \frac{\partial f_{k-1}}{\partial \mathbf{w}} \right|_{\hat{\mathbf{x}}_{k-1}^+} = \begin{bmatrix} 0 & 0 & 0 & 0 \\ \frac{T}{m_x} & 0 & 0 & 0 \\ 0 & 0 & 0 & 0 \\ 0 & \frac{T}{m_y} & 0 & 0 \\ 0 & 0 & T & 0 \\ 0 & 0 & 0 & T \end{bmatrix} \quad (4.26)$$

$$\mathbf{H}_k = \left. \frac{\partial h_k}{\partial \mathbf{x}} \right|_{\hat{\mathbf{x}}_k^-} = \begin{bmatrix} 1 & 0 & 0 & 0 & 0 & 0 \\ 0 & 0 & 1 & 0 & 0 & 0 \end{bmatrix} \quad (4.27)$$

$$\mathbf{M}_k = \left. \frac{\partial h_k}{\partial \mathbf{v}} \right|_{\hat{\mathbf{x}}_k^-} = \begin{bmatrix} 1 & 0 \\ 0 & 1 \end{bmatrix} \quad (4.28)$$

where the partial derivatives in the matrix in Eq. (4.25) are computed from the second and fourth rows of Eq. (4.23) as

$$\frac{\partial \ddot{x}}{\partial K_t} = \sum_{p=1}^n \frac{T}{m_x} (-\cos \theta_{p,k-1}) b u_{p,k-1} \quad (4.29)$$

$$\frac{\partial \ddot{x}}{\partial K_r} = \sum_{p=1}^n \frac{T}{m_x} (-\sin \theta_{p,k-1}) b u_{p,k-1} \quad (4.30)$$

$$\frac{\partial \ddot{y}}{\partial K_t} = \sum_{p=1}^n \frac{T}{m_y} (\sin \theta_{p,k-1}) b u_{p,k-1} \quad (4.31)$$

$$\frac{\partial \ddot{y}}{\partial K_r} = \sum_{p=1}^n \frac{T}{m_y} (-\cos \theta_{p,k-1}) b u_{p,k-1} \quad (4.32)$$

where $\theta_{p,k-1}$ and $w_{p,k-1}$ are the angular displacement and chip thickness, respectively, for tooth p on iteration $k - 1$. Note that here w indicates chip thickness instead of process noise. Also note that when chip thickness is zero, as when tooth p is not cutting, these partial derivatives equal zero for that tooth. The effects of the cutting force coefficients, therefore, are only present in \mathbf{F}_{k-1} (Eq. (4.25)) when one or more teeth are cutting. Only when one or more teeth are cutting can the EKF estimate the cutting force coefficients. When no teeth are cutting, the EKF only maintains the previous estimate of the coefficients. This fact is directly related to the observability of the coefficients, which is discussed again in Section 4.5, and follows from the fact that, given the cutting force model employed in this study, no information can be discerned about the cutting force coefficients unless the tool is actually cutting. Approaches to computing cutting force coefficients based on tooth geometry do exist [17], but these approaches are unnecessary when the goal is estimating updated coefficient values to accommodate changes in the tool-workpiece system.

Given the EKF definition of Eqs. (4.23)-(4.32), the noise vector for process noise, \mathbf{w} , holds four variables (noise in tool deflection along each axis and noise in each cutting force coefficient), so the covariance matrix of process noise, \mathbf{Q}_k , is a 4×4 matrix. The noise vector for measurement noise, \mathbf{v} , holds two elements (i.e., the noise in tool deflection along each axis). The covariance matrix of measurement noise, \mathbf{R}_k , therefore, is a 2×2 matrix.

Note that cutting coefficients may vary from one tooth to another, as when one tooth is more worn than the other. Two EKFs can be run in parallel to estimate the cutting coefficients of each tooth separately, at least in the case of a milling tool with two

flutes. For greater numbers of flutes, it is still possible to estimate cutting coefficients of each tooth separately if only one tooth is engaged at a time (as when radial immersion is sufficiently small). Even if there are only intermittent windows of time in which only one tooth is cutting, the cutting coefficients for that tooth may be estimated separately from the other teeth. The smaller the window of time, however, the longer the EKF may take (i.e., the more information it may require) to converge to an accurate estimate. If no such windows of single-tooth cutting exist, then it appears to be impossible to maintain observability of separate cutting coefficients for each tooth, given that there would be more unknown parameters to estimate than there were measurements available (see Section 4.5 for a discussion of observability).

An approach to estimating asymmetric cutting force coefficients in this multiple-tooth-cutting scenario (instead of estimating a single set of coefficients for all teeth) might be to estimate separate sets of coefficients for the smallest number of teeth cutting as possible. For example, if two is the least number of teeth cutting at an instant, then separate cutting force coefficients could be estimated for every window of time in which only two teeth are engaged (rather than three or more). This approach would result in estimates for each pair of adjacent teeth. Each tooth would be represented in two different sets of estimates (or three sets if three were the least number of teeth cutting at an instant), one for each pair of adjacent teeth in which the tooth lay. By averaging these two (or more) adjacent sets of estimates, the coefficients for the given tooth might be estimated, and in this way, the respective contributions of each tooth to the estimates might be discovered. It is unknown whether this approach would provide accurate estimates for each tooth, but it is proposed here for consideration in high-radial-

immersion cutting scenarios and scenarios in which the tool has more than two cutting flutes. This approach is unnecessary for this study and is, therefore, not included in any results.

To estimate cutting force coefficients separately for each tooth, two EKFs were run in parallel. One estimated the deflections and velocities of the tool along both axes, as well as the cutting force coefficients for the first tooth. The second EKF estimated the same tool deflections and velocities, as well as the cutting force coefficients for the second tooth. The cutting force coefficient estimates from the first EKF were used to calculate the cutting forces applied by the first tooth, and the estimates from the second EKF were used to calculate the forces applied by the second tooth. This EKF structure differed from the structure used when modal parameters were estimated by requiring a different input.

Where cutting force was considered an external input to the model when modal parameters were being estimated, chip thickness was considered the model input when cutting force coefficients were estimated. In both instances, tool deflection estimates were not used in the calculation of chip thickness, so the feedback effect inherent in the system was omitted from the EKF structure. Introducing feedback into the EKF structure would require the inclusion of delayed states in the structure, increasing the complexity of the EKF. The performance effects of including delayed states in an EKF were unknown, so instead chip thickness was considered a model input and all delayed states used for chip thickness calculation were based on state measurements and not estimates. The effect of including feedback in the EKF structure remains an important consideration for future research efforts, as it could improve accuracy and reliability of EKF estimates.

4.5. Observability

The observability of a dynamic system denotes whether a historical knowledge of system outputs can provide enough information to determine current system states. Analogous to the degrees of freedom of a system, observability is dependent on the number of independent equations describing the system and how the estimated states and parameters relate to those equations. A time-invariant linear system, such as a Kalman filter defined for a linear (or linearized) system in terms of non-varying relationships between its states, has the observability matrix [56]

$$\mathbf{O} = \begin{bmatrix} \mathbf{H} \\ \mathbf{HF} \\ \mathbf{HF}^2 \\ \vdots \\ \mathbf{HF}^{N-1} \end{bmatrix} \quad (4.33)$$

where \mathbf{F} and \mathbf{H} are partial derivative matrices that describe the relationships between the update equation and the states, and the measurement equation and the states, respectively. N indicates the total number of states in the system. For the Kalman filter, therefore, N is the number of states and parameters being estimated. Note that the rows of \mathbf{O} represent the equations for the theoretical values of successive measurements, where the first measurement is the matrix product of \mathbf{H} and the initial state vector \mathbf{x}_0 , the second measurement is the matrix product of \mathbf{H} and the updated state vector \mathbf{x}_1 (which equals $\mathbf{F}\mathbf{x}_0$), the third measurement is the matrix product of \mathbf{H} and the next updated state vector \mathbf{x}_2 (which equals $\mathbf{F}^2\mathbf{x}_0$), and so forth. For a system to be observable, N must equal the

rank of \mathbf{O} which, for a Kalman filter, means the number of estimated states and parameters must equal the number of independent equations (or independent measurement updates) represented by \mathbf{O} .

For the EKF described in Kennedy [35], \mathbf{F} and \mathbf{H} are described by Eqs. (4.10) and (4.12), respectively, and the resulting rank of \mathbf{O} is 3, compared to $N = 5$. It is clear that this system is not observable. If only one modal parameter is estimated instead of all three, then the system becomes observable. Kennedy argues that in practice the three parameter estimates still converge and recommends the use of the three-parameter EKF over a one-parameter EKF to provide a more accurate characterization of the tool-workpiece dynamic system. To guarantee convergence over a wider range of circumstances, however, observability is required.

By adding measurements of tool deflection along the y -axis to the EKF and extending the state estimate vector to include deflection and velocity along the y -axis, the rank of \mathbf{O} can be increased to 6, where N has been increased to 7. The corresponding EKF is described in Section 4.3, where \mathbf{F} and \mathbf{H} are described by Eqs. (4.17) and (4.19), respectively. Again the system is not observable, but if two modal parameters are estimated instead of three, the system becomes observable. Furthermore, if two cutting force coefficients are estimated instead of modal parameters, the system should remain observable. This situation is achieved with the EKF described in Section 4.4, in which \mathbf{F} and \mathbf{H} are described by Eqs. (4.25) and (4.27), respectively, and the resulting rank of \mathbf{O} is 6, compared to $N = 6$. Note that the cutting force coefficients cease to be observable when no teeth are in contact with the workpiece.

It is also possible that an alternative pair of parameters (e.g., modal stiffness and radial cutting coefficient) could be estimated with maintained observability, which raises the question of which pair results in the best characterization of the system and exhibits the best convergence. This question must be addressed through testing the EKF on simulated and experimental tool deflection data, and through comparing the resulting calculations of stability boundaries with experimental data to determine if the system characterization is accurate.

CHAPTER 5: SIMULATION RESULTS

5.1. System Parameter Identification

Numerical simulations were conducted using the traditional chip thickness model given in Section 2.2 to provide measurement data for testing EKF. Simulated data was desired in order to evaluate the performance of the EKF by comparing the system parameters used in the simulation with the parameter estimates produced by the EKF. Then the EKF could be tested with similar experimental data to determine if it produced similar parameter estimates. First, however, appropriate system parameters (i.e., modal parameters and cutting force coefficients) had to be identified to run simulations that agreed well with experimental data.

To identify the modal parameters of the system, the response of a milling tool to a hammer impulse was analyzed by a procedure similar to the one in Kennedy [35] while the tool was mounted in the spindle. The tool was composed of tungsten carbide and had two flutes with a helix angle of 30 deg. Modal parameters of the system along the x -axis were found to be $m_x = 0.03211$ kg, $c_x = 13.39$ kg/s, and $k_x = 1.023 \times 10^6$ N/m. The modal parameters along the y -axis were assumed to be equal to those along the x -axis to simplify parameter estimation. This assumption reduces the number of unknown parameters that must be estimated by an EKF when estimating modal parameters as in Section 4.3, and it reduces the number of measurements that must be taken prior to running the EKF. Given that the workpiece lies primarily in the positive y -direction, it is possible that the tool-workpiece system has greater rigidity in the y -direction than in the x -direction. This rigidity would exist only when the tool is in contact with the

workpiece, but in low-radial-immersion milling, the proportion of time in which the tool is contacting the workpiece is very small with respect to the time it is allowed to vibrate freely. Any asymmetry of the modal parameters between the two axes might be due to asymmetry of the spindle, but any such asymmetry is neglected for this study.

The modal parameters from the hammer test were used in simulations as initial parameter guesses in order to find an offset angle between the simulated and experimental data (to allow the EKF to run on experimental data). These guesses were later updated to the modal parameter estimates from the EKF, and the simulations were run again for comparison with the experimental data. The EKF estimates and the hammer test values were significantly different, and the reason for these differences is not entirely clear. It should be noted, however, that the hammer test was conducted with a stationary spindle, and modal parameters change with spindle speed. In particular, it has been shown that spindle bearing stiffness varies with spindle speed [21, 22], so the effects of spindle speed on modal mass and damping may also be significant.

Using a force dynamometer according to the procedure outlined in Section 3.2, the cutting force coefficients of the same tool, when cutting Aluminum 6061-T6511, were found to be $K_t = 5.89 \times 10^8 \text{ N/m}^2$ and $K_r = 3.19 \times 10^8 \text{ N/m}^2$. Using these cutting force coefficients in a simulation resulted in tool deflections that were significantly smaller in magnitude than those of a similar experimental test, and the simulated bifurcation (transition from chatter-free to chatter milling) occurred at a slightly lower axial depth of cut than in the experiment (3.5 mm in the simulation, 3.8 mm in the experiment). The experimental test also exhibited greater tool deflections in the x -direction over one half of each revolution than over the other half, whereas the simulation

exhibited almost exactly the same deflections over each tooth path. This discrepancy might be caused by tooth asymmetry (e.g., the two teeth have worn unevenly) or runout (i.e., eccentricity in the tool mounting). Numerical optimization was employed, therefore, to attempt to reconcile the differences between the single-revolution deflection behavior of the simulation and experiment.

Despite the discrepancies between the simulation and experiment, using these hammer-test modal parameters and dynamometer cutting force coefficients in the simulation allowed the simulated and experimental trajectories to be synchronized over one revolution which, in turn, provided information regarding when the teeth are engaged in the workpiece in the experimental data. This information was not previously known because the tachometer pulse was not necessarily simultaneous with tooth engagement. Based on this synchronization, the EKF could be run in phase with the experimental data, meaning that the EKF model could calculate cutting forces for the same time steps as those in which the teeth were, in fact, engaged in the workpiece. Without knowing the offset angle between the simulation and the experiment (i.e., the angle between $\theta_1 = 0$ and the tachometer pulse), the EKF would be calculating cutting forces out of phase with the experimental measurements. Synchronization was accomplished by minimizing the error between the simulated and experimental tool trajectories for one revolution by testing every possible phase angle at one-degree increments.

It may not always be the case that the modal parameters from the hammer test and the cutting force coefficients from the dynamometer test result in a good enough correlation between the simulation and experiment to allow the offset angle to be found immediately. If the offset angle is not found with sufficient accuracy from these

parameter values, it is possible that numerical optimization could be used to synchronize the simulated and experimental tool trajectories well enough to find this angle. In fact, numerical optimization was used in this study as a preliminary means of finding parameter values that result in good correlation between the simulation and experiment, but it was found to be unnecessary for identifying the parameter values in the data used in this study. The numerical optimization approach is discussed later and may prove useful in synchronization of future data.

Using the offset angle discovered through the synchronization process, the EKF in Section 4.4 was run on experimental data (see Section 6.2 for more details about this trial) to estimate cutting force coefficients. The resulting estimates were $K_{t1} = 2.48 \times 10^8 \text{ N/m}^2$, $K_{t2} = 6.64 \times 10^9 \text{ N/m}^2$, $K_{r1} = 2.20 \times 10^8 \text{ N/m}^2$, and $K_{r2} = 4.15 \times 10^9 \text{ N/m}^2$, where the first and second tooth are designated by subscript numerals. Running the simulation again with the estimated coefficients (and estimated modal parameters described later) produced a simulated tool trajectory that correlated well with the experimental data. It is interesting to note that the coefficients found with the dynamometer fall between the extremes of the two teeth as found with optimization or the EKF. That is, the tangential coefficient $K_t = 5.89 \times 10^8 \text{ N/m}^2$ (dynamometer) falls between $K_{t1} = 2.48 \times 10^8 \text{ N/m}^2$ (EKF) and $K_{t2} = 6.64 \times 10^9 \text{ N/m}^2$ (EKF), and the radial coefficient $K_r = 3.19 \times 10^8 \text{ N/m}^2$ (dynamometer) falls between $K_{r1} = 2.20 \times 10^8 \text{ N/m}^2$ (EKF) and $K_{r2} = 4.15 \times 10^9 \text{ N/m}^2$ (EKF). The dynamometer force measurements, however, showed approximately the same force for each tooth, which means the tool probably deflected similarly over each half revolution and did not exhibit the asymmetry observed in the tool deflection measurements used for parameter estimation. Perhaps

tooth asymmetry, whether in the form of runout or uneven wear, was less severe in the dynamometer trials than in the trials used to measure tool deflection.

Not only might different amounts of runout or wear produce a discrepancy between the simulation conducted with the dynamometer values of cutting force coefficients and the experiment, but there might be other sources of error as well. In particular, the spindle speed used during dynamometer tests was 200 rpm, in order to increase the apparent resolution of force measurements (i.e., more time steps per revolution at a sampling rate of 40 kHz) and to minimize the loads applied to the dynamometer, which was mounted on the spindle of the machining center. This spindle speed is much different from the 15,000 rpm used in the deflection measurement trials, and cutting coefficients are likely to vary over this range. It is clear, for instance, that tool temperature varies over this range, which is part of the motivation for high-speed milling in the first place [57], and it is quite possible that cutting coefficients would vary over this range as well (if only as a result of the temperature and built-up edge variations). Moreover, this difference in speeds may explain why tooth asymmetry appeared more severe in the deflection measurement trials, given that runout deflection would be exacerbated by the high centrifugal inertial forces of high-speed milling.

Due to the discrepancies between the simulation and experiment, it was decided to use the EKF to estimate the system parameters from experimental tool deflection data and then check for correlation of the simulation with the experiment to confirm the validity of these values. Hence, cutting force coefficient estimates produced by the EKF were found first and set to be constant, while EKFs based on those in Section 4.3 were used to estimate modal parameters from the same experimental data. Note that the modal

parameters were not estimated first because it was believed, based on numerical optimization attempts, that the dynamometer values of cutting force coefficients resulted in worse correlation of the simulation with the experiment than the hammer-test values of modal parameters did (apart from increasing damping to avoid early bifurcation, as already mentioned). The second EKF described in Section 4.3 estimates all three modal parameters based on deflection measurements along both the x - and y -axes. As discussed in Section 4.3, however, these measurements allow only two modal parameters to be estimated with observability. Therefore, to maintain observability for this study, the modal parameters were estimated two at a time (see Sections 4.3 and 6.1 for details on removing rows and columns of the EKF structure to do this).

First only the modal mass and stiffness were estimated (given that stability boundaries seem to be least sensitive to the value of modal damping, as in Fig. 4.1 in Section 4.2) and then only modal mass and modal damping, after changing the EKF to assume a constant modal stiffness equal to the newest stiffness estimate. The second modal mass estimate was within a percent of the estimate from the first EKF run, and all the resulting modal parameter estimates were $m_x = 0.03134$ kg (from the first run), $c_x = 22.21$ kg/s, and $k_x = 9.840 \times 10^5$ N/m. Damping changed the most significantly of the three modal parameters from the hammer-test values, increasing more than 65 percent from $c_x = 13.39$ kg/s, while mass and stiffness both decreased by less than 4 percent from $m_x = 0.03211$ kg and $k_x = 1.023 \times 10^6$ N/m. As it was already observed that the initial parameter guesses (such as the damping found with the hammer test) resulted in an earlier bifurcation than was observed in the experiment, it is interesting to note that the EKF estimated a larger damping value than was found with the hammer test, which tends

to delay bifurcation. It is also interesting to note that the EKF estimated a lower stiffness than the hammer test, which seems to be consistent with observations in [21] that bearing radial stiffness decreases with rotation speed. Even the amount of decrease estimated here seems rather conservative compared to the amounts described in that study (where increasing speed from zero to 12,000 rpm, for example, results in more than a 20 percent decrease in bearing stiffness).

Details of how the simulation was conducted, along with a comparison of the two chip thickness models in Chapter 2, are described in Section 5.2, and a comparison of the simulated and experimental data is given in Section 5.3. The modal parameter and cutting force coefficient estimates produced by the EKF from experimental data are used in the simulations in the sections following this one, unless otherwise noted.

As mentioned earlier, numerical optimization was used as a preliminary approach to finding a set of cutting coefficients that minimized the error between the tool trajectories of the simulation and experiment over a single revolution. The process is described here because of its usefulness in fitting simulated data to experimental data by modifying system parameters used in the simulation, but numerical optimization requires far more computational cost than EKF parameter estimation because of the large number of simulations that must be conducted.

The MATLAB `fmincon` function was used to adjust the radial and tangential cutting force coefficients of each tooth independently to minimize error. Adjusting cutting force coefficients to match experimental data is essentially what the EKF in Section 4.4 does, so numerically optimizing the cutting force coefficients of the simulation is a reasonable approach to producing simulated data that mirrors the

experiment and can be easily analyzed by the EKF. As discussed in Section 4.4, the EKF can estimate cutting force coefficients separately for each tooth, so running the simulation with asymmetric cutting force coefficients should not impede the EKF from running smoothly. Numerical optimization produced a fairly good match between simulated and experimental single-revolution tool trajectories at an axial depth of cut of about 2 mm. The cutting coefficients selected by the optimization algorithm were similar to values that were later estimated by the EKF. The corresponding EKF estimates, except for K_{t1} , all fell within 25 percent of the values found by numerical optimization (K_{t1} was more than double the value found by optimization). Both the optimized coefficients and the estimated coefficients produced simulated tool trajectories that correlated well with the experimental data. The actual values are omitted here because they (and the EKF estimates they were compared with) were found by using an outdated conversion factor for converting experimental tool deflection at the sensor to the tip (see Section 3.1 for the factor used in this study).

Before proceeding, it is noted here that modifying the modal parameters in a simulation can have similar results to modifying the cutting force coefficients. The fact that adjusting either set of system parameters could have similar results on chatter stability (as computed with TFEA) was considered in Section 4.2, but this has been observed in numerical simulations as well. In [58], for instance, it was observed that two different approaches resulted in a good correlation of bifurcation point and vibration magnitude between the simulation and experiment. The first approach involved running the simulation with the modal parameters found by a hammer test but reducing the values of cutting coefficients used in the simulation by 50 percent from those found with a

dynamometer (note that the given dynamometer values were actually incorrect, being twice the real dynamometer values, but the comparison of approaches remains applicable). The second approach involved using the values of cutting force coefficients found with the dynamometer in the simulation, but adjusting the modal parameters used in the simulation from those found with the hammer test. Modal mass was increased by 20 percent, and modal damping was increased by 70 percent. Both approaches resulted in a similar bifurcation point and similar magnitude of vibration. The effect of these two approaches on the shape of the tool trajectory over one revolution was not discussed, but it is possible that either approach might result in good correlation between simulation and experiment.

5.2. Comparison of Chip Thickness Models

The chip thickness models described in Sections 2.2 and 2.3 were used to simulate incline cuts (i.e., cuts in which axial depth of cut steadily increases) in order to compare the axial depths of cut (or bifurcation points) at which chatter began between the two models. The axial depth of cut varied in each simulation from 0 mm at the beginning to whatever value was desired (usually between 2 and 5 mm, depending on whether bifurcation was desired or not), and each simulation assumed a 0.382 mm radial depth of cut, 0.0635 mm per tooth feed rate, 15,000 rpm spindle speed, and tool radius of 0.25 in (6.35 mm). Due to the sensitivity of the bifurcation point to initial conditions, it was important that each trial begin at the same axial depth of cut of 0 mm. The cutting conditions were selected for ease of comparison with simulations conducted by Kennedy [35], as well as to allow for experimental validation with the tools and workpieces on

hand. The conditions also provided a well-marked bifurcation point in simulations using the chip thickness models described in Sections 2.2 and 2.3.

The numerical integration method selected for these simulations was a symplectic Euler method [59]. This method works well for stiff systems and systems with rapid oscillation, better preserving the energy of the system than the original Euler approach and even some Runge-Kutta methods. The symplectic Euler method also exhibits better numerical convergence and can use a larger time step in this application than the original Euler method, which improves computational efficiency.

The simulations are conducted with a time step defined by 800 steps per tooth pass, which results in a good, converged solution without requiring an unreasonable computational cost. The resulting time step is 2.5×10^{-6} s for a spindle speed of 15,000 rpm. The axial depth of cut increases at a rate of 1 mm per 1,290 revolutions, which results in the total feed being 986 mm while the feed rate is 0.0635 mm per tooth. This total feed matches the length of a workpiece that is used for experimental tests. The modal parameters and cutting force coefficients were set to the values identified in Section 5.1.

Figure 5.1 illustrates the difference in bifurcation points between the traditional and numerical chip thickness models. To more clearly illustrate the bifurcation, the tool deflection is plotted in red at the same angle in each revolution and is denoted x_n . The bifurcation points using the traditional and the numerical models are about 2.0 and 1.8 mm, respectively. Poincaré maps are given to the right of the deflection-vs.-depth plots, showing the deflection on one revolution (x_n) plotted against the deflection on the previous revolution (x_{n-1}) over twenty revolutions at axial depths of cut of 1 mm and 3

mm. From these maps it is clear that the tool is chatter-free at 1 mm and exhibits chatter at 3 mm, as the once-per-revolution points lie in close vicinity to each other (nearly coinciding) when no chatter is present, but the points separate into a rounded cloud when chatter is present. Reconfiguration of the points indicates that the tool no longer has the same deflection at the same angle in every revolution (i.e., tool deflection no longer has the same period as tool rotation), but rather the tool is found at various deflections for the same angle of each revolution. This reconfiguration is characteristic of a bifurcation or transition from the absence to the presence of chatter. The presence of chatter is characterized by multiple distinct points, rather than just one, and typical point configurations include four distinct points (or clusters of points), a deformed ellipse composed of more than four points, and a cloud of numerous points.

Figure 5.2 compares the two models by showing tool deflection and chip thickness as a function of rotation angle for one revolution at an axial depth of cut of 1 mm. Because this is a lower depth of cut than the bifurcation point in both simulations, no chatter is present in the figure. It is evident from the plot that both models produce nearly the same tool deflections and chip thicknesses for this revolution. Figure 5.3 shows the differences between the two models for this revolution. The greatest differences lie in the chip thickness where the traditional model significantly overshoots the numerical model, but only briefly.

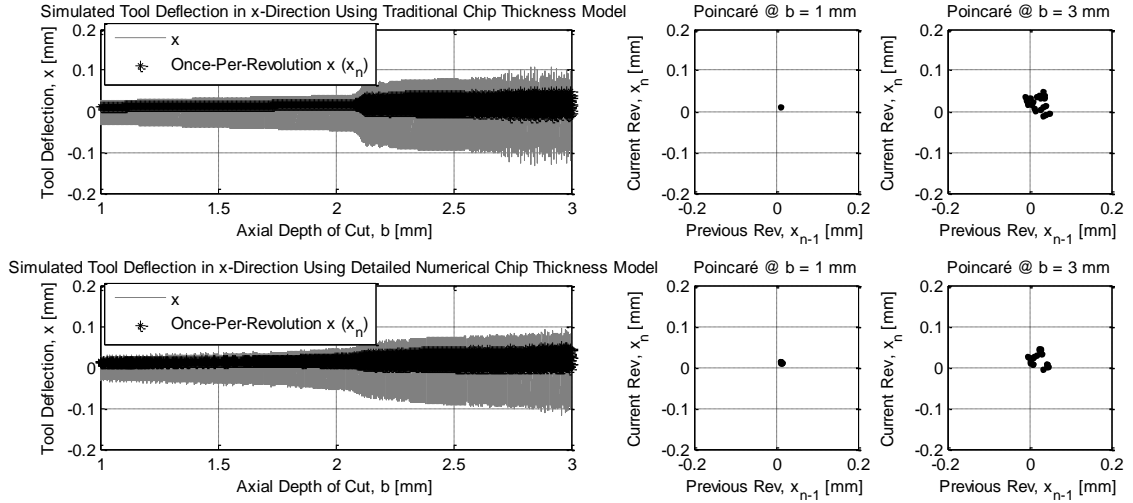


Figure 5.1. Comparison between simulations of an incline cut using traditional (top) and numerical (bottom) chip thickness models.

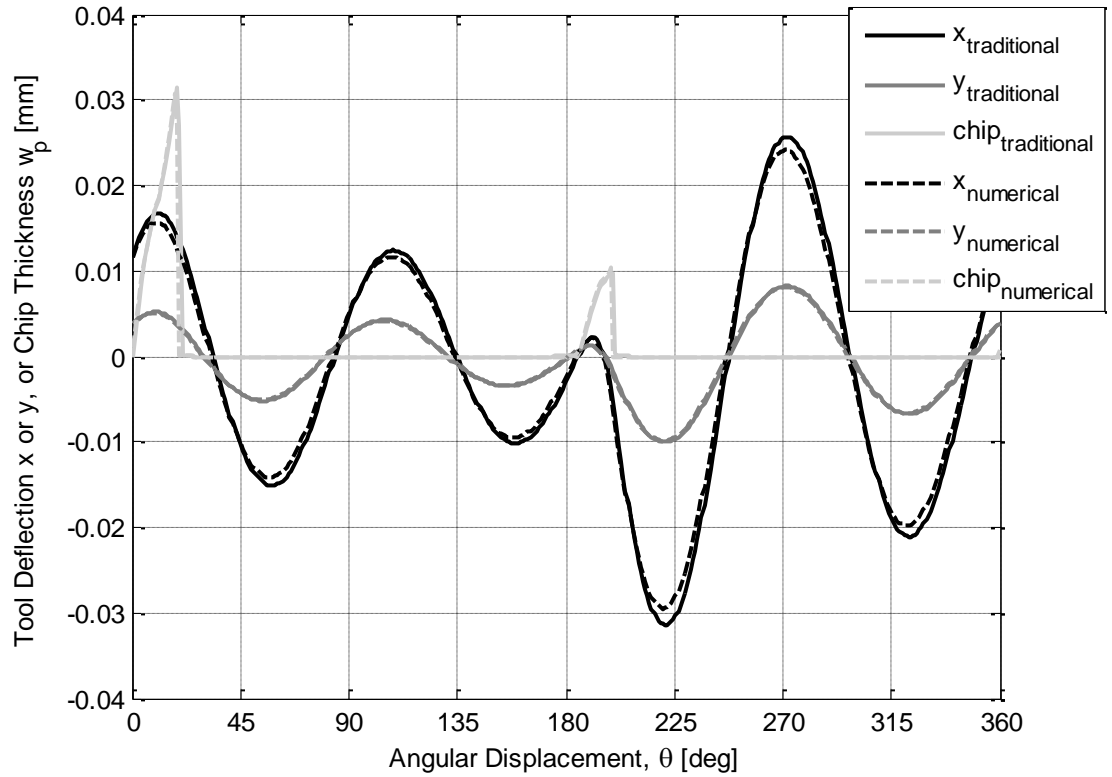


Figure 5.2. Comparison of traditional and numerical chip model simulations over one revolution near 1 mm axial depth of cut.

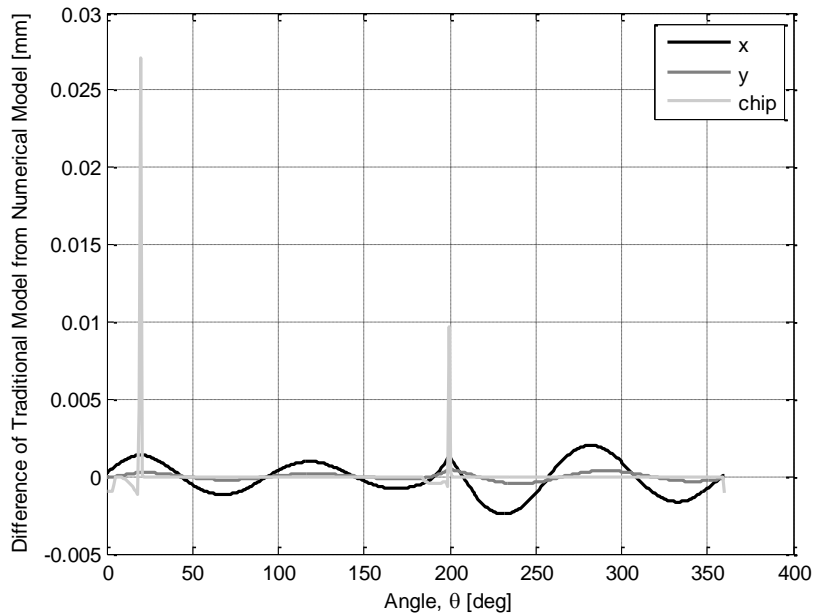


Figure 5.3. Differences of traditional chip model simulation from numerical chip model simulation over one revolution near 1 mm axial depth of cut.

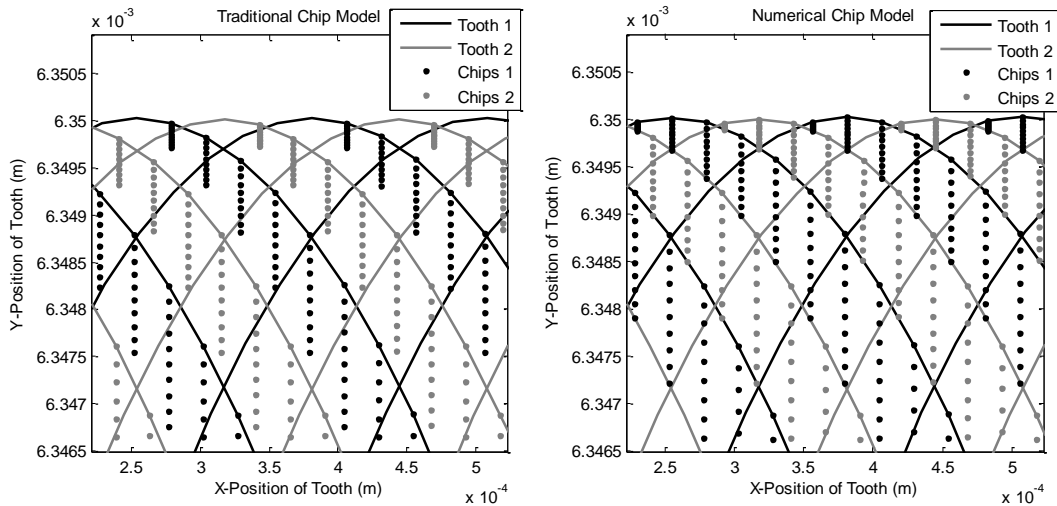


Figure 5.4. Example of simulated tooth paths and chip thicknesses using traditional and numerical chip thickness models.

Figure 5.4 shows examples of consecutive tooth paths of the tool, as simulated by the traditional and numerical models, along with the corresponding chip thickness (plotted along a line extending to the tool center) at each time step in the simulations. These tooth paths occur near the beginning of the simulation and are chatter-free with an

axial depth of cut near zero. The greatest difference between the traditional model on the left and the numerical model on the right lies in the magnitude of the chip thicknesses. The traditional model repeatedly underestimates the actual distance between one tooth pass and the next, while the numerical model finds the distance more accurately by conducting a numerical search. Because the results of the two chip thickness models are so similar, and because the numerical model requires about sixteen times as much computational time (e.g., more than an hour instead of a few minutes for a simulation from 0 mm to 6 mm depth of cut), the traditional chip thickness model is used throughout this study unless otherwise noted.

The numerical chip thickness model did result in once-per-revolution deflection patterns that were significantly different from the traditional model, despite having all the same system parameters. Figures 5.5-5.6 display the once-per-revolution plots in more detail than in Fig. 5.1. The numerical model appears to display a sort of secondary bifurcation not present at the same depth as the traditional model. The initial bifurcation is characterized by a transition from a nearly periodic orbit to a more complicated yet still orderly orbit, but the secondary bifurcation transitions from the orderly orbit to a more chaotic sort. Secondary bifurcations have been observed in experimental data, so the ability of the numerical chip thickness model to produce such bifurcations may be a desirable feature. The traditional model has produced similar bifurcation phenomena, however, and might do so in this situation as well if given a great enough axial depth of cut. Note in Section 7.2 that the addition of certain inertial forces to the dynamic model can also produce complex bifurcation phenomena with the traditional chip thickness model. The numerical chip thickness model did result in a rougher orbit in Fig. 5.6 than

the traditional model prior to bifurcation, perhaps due to the complicated effects of asymmetric cutting force coefficients on the numerical tooth-workpiece intersection calculations.

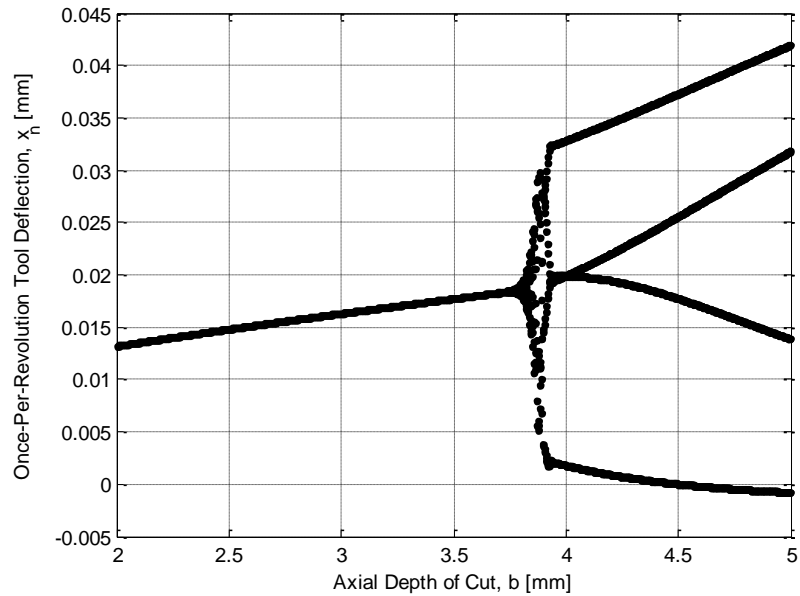


Figure 5.5. Once-per-revolution tool deflection results of simulation with traditional chip thickness model and system parameters from Section 5.1.

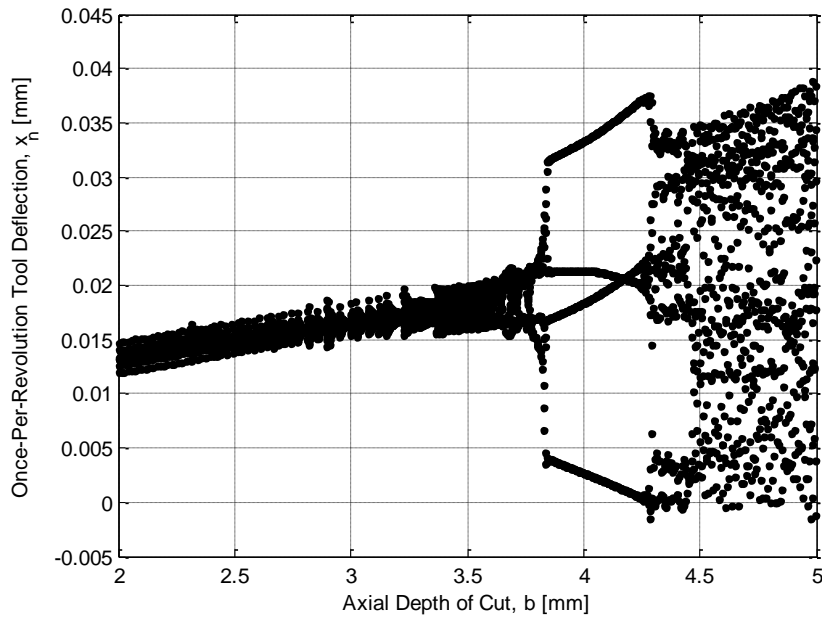


Figure 5.6. Once-per-revolution tool deflection results of simulation with numerical chip thickness model and system parameters from Section 5.1.

5.3. Comparison of Simulations to Experiments

Several experimental milling cuts were conducted with the experimental setup shown in Section 3.1. All the trials used the same tool radius, radial depth of cut, feed rate, spindle speed, and axial depth of cut as the simulations in Section 5.2, except for the decline cuts, which had a decreasing axial depth of cut instead of an increasing one. Bifurcation points for the simulations and experimental trials are given in Table 5.1. Three trials had an axial depth of cut that increased (incline cut) from 0 mm to 6 mm, and three had an axial depth of cut that decreased (decline cut) from 6 mm to 0 mm. The bifurcation points given for the simulation trials in Table 5.1 are found by running simulations with system parameters estimated by EKFs, using the procedure described in Section 5.1 to identify system parameters (i.e., finding the offset angle between the simulation and experiment using the hammer-test and dynamometer parameters, then estimating cutting force coefficients using the hammer-test parameters, then estimating modal mass and stiffness using the hammer-test modal damping and the new force coefficient estimates, and then estimating modal damping using the new mass, stiffness, and coefficient estimates). Note that, as in Chapter 6, initial EKF parameter estimates were randomized to check the repeatability of the EKF. A single set of randomized initial estimates was used in finding the values in this section to reduce the effect of randomization on parameter identification. These randomized initial values were approximately $K_{t1} = 1.493 \times 10^8 \text{ N/m}^2$, $K_{r1} = 2.315 \times 10^8 \text{ N/m}^2$, $K_{t2} = 4.257 \times 10^9 \text{ N/m}^2$, $K_{r2} = 3.106 \times 10^9 \text{ N/m}^2$, $m_x = 0.02270 \text{ kg}$, $c_x = 40.56 \text{ kg/s}$, and $k_x = 1.162 \times 10^6 \text{ N/m}$.

The first incline cut trial was used to find the system parameters in Section 5.1, and the corresponding simulations in Fig. 5.1 exhibit the same bifurcation points (both 3.8 mm) as the experimental trial. Tool deflection measured for the experimental incline trials is plotted against axial depth of cut in Fig. 5.7 for comparison to the simulation results in Fig. 5.1. The magnitude of tool deflection in the simulations in Fig. 5.1 also correlates well with that of the first incline experimental trial (based on which the system parameters were identified in Section 5.1). Furthermore, the Poincaré maps of the simulations in Fig. 5.1, especially those of the traditional chip thickness model, reflect the behavior of the Poincaré maps of the first trial in Fig. 5.7 at 2 mm and 5 mm axial depth of cut (again with points plotted over twenty revolutions on each map). The similarities of both models to the experimental results, coupled with the wide variation in bifurcation points in the experimental results, seem to indicate that either chip thickness model can be used to simulate tool deflection under these cutting conditions with reasonable accuracy.

Table 5.1. Bifurcation points of six experimental cuts, three with increasing axial depth of cut (incline) and three with decreasing axial depth of cut (decline), compared to simulation results for the system parameters identified in Section 5.1 from the first incline trial.

Bifurcation Points (mm)			
SIMULATION (Traditional)			
Trial #	1	2	3
Incline Cut (0 to 6 mm)	2.0	>6	4.0
Decline Cut (6 to 2 mm)	>6	3.0	2.3
SIMULATION (Numerical)			
Trial #	1	2	3
Incline Cut (0 to 6 mm)	1.8	>6	3.6
Decline Cut (6 to 2 mm)	>6	3.2	2.5
EXPERIMENT			
Trial #	1	2	3
Incline Cut (0 to 6 mm)	3.8	3.1	3.0
Decline Cut (6 to 0 mm)	2.9	2.5	2.5

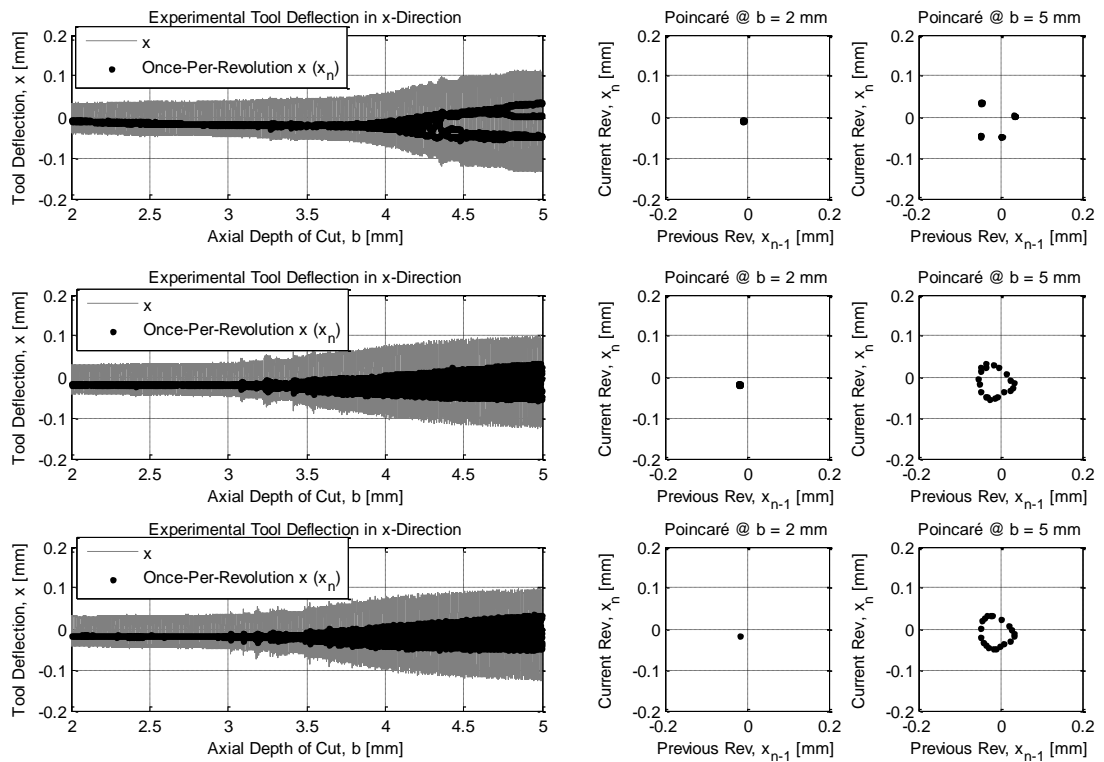


Figure 5.7. Experimental tool deflection results for incline cuts #1 (top), #2 (middle), and #3 (bottom) from Table 5.1.

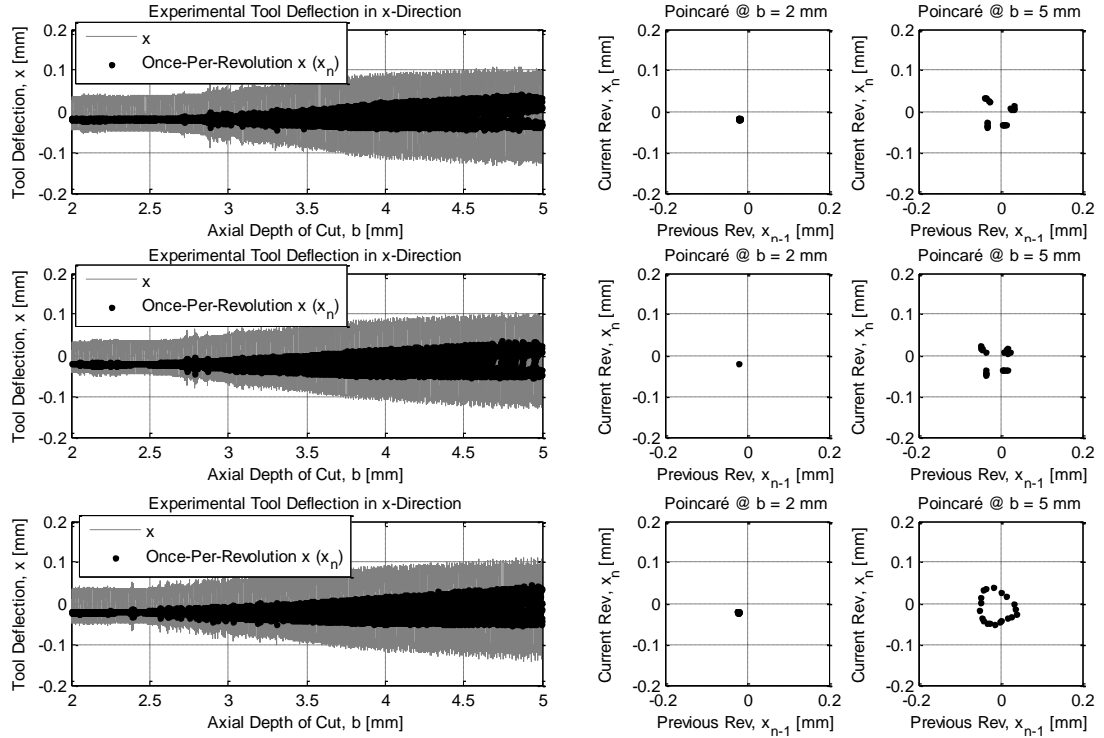


Figure 5.8. Experimental tool deflection results for decline cuts #1 (top), #2 (middle), and #3 (bottom) from Table 5.1.

Figure 5.8 shows the decline trials for comparison to the incline trials in Fig. 5.7. The bifurcation points are consistently shallower than those in the incline trials, but the Poincaré plots are similar in character to those of the incline trials, exhibiting either a deformed ellipse or four clusters of points. Hysteresis is clearly evident in the experimental bifurcation points given in Table 5.1, as they depend on whether the axial depth of cut is increasing or decreasing. Hysteresis is known to appear in milling bifurcations and is exhibited by numerical simulations of milling as conducted by Radhakrishnan [40] and Kennedy [35]. As in those studies, the chip thickness models here have been observed to display hysteresis and to bifurcate early if given a perturbation. Due to the gradual and sometimes tentative nature of the bifurcations

exhibited in Figs. 5.7 and 5.8, bifurcation points listed in Table 5.1 should be considered approximations.

Note that the experimental data that was used to identify system parameters in Section 5.1 and for running the EKF in Chapter 6 was resampled to a time step of 5×10^{-7} s from the original experimental time step of 1×10^{-5} s before running the EKF. Resampling was conducted with the aim of estimating system parameters more accurately (by increasing the number of EKF iterations over the same time interval) and producing more accurate bifurcation points in the simulations. In most trials the resampling accomplished these goals, but in the first incline trial, the resulting bifurcation point was significantly shallower and less accurate than it would have been with the original step size. Higher-resolution resampling could potentially improve the estimation accuracy even further in general, but the EKF estimates produced by high-resolution resamplings are sometimes unreasonable (e.g., negative). For instance, resampling a slightly different section of experimental data from the first incline trial to 5×10^{-7} s resulted in negative modal parameter estimates from the EKF. A more in-depth discussion of the effects of resampling is given in Section 6.1.

It is noted here that, as in Section 5.1, the initial offset angles for the experimental trials were found by running a simulation with system parameters based on the hammer and dynamometer tests. These parameter values served as the guesses for any constant (non-estimated) parameters when running the EKF to estimate parameter values from the experimental measurements. Because the hammer-test and dynamometer values were significantly different from the EKF parameter estimates, the initial offset angles used to run the EKF may be somewhat different from the actual offset angles which, in turn, may

contribute to the errors between simulated and experimental bifurcation points in Table 5.1 (and influence the corresponding system parameter estimates in Table 5.2). Typically the offset angle found with the EKF parameter estimates was only a degree or so different from the initial guess of the offset angle found with the hammer-test and dynamometer parameter values, so this potential source of error seems to be limited in effect.

The traditional chip model simulation (used in Table 5.1) and the experimental data from the first incline cut are compared in Fig. 5.9 for a single revolution at an axial depth of cut near 2 mm. The experimental data has been shifted by an offset angle, as discussed in Section 5.1, to align the tachometer pulse in the experimental data with $\theta_1 = 0$ in the simulation. The general shapes of the simulated and experimental trajectories are similar, though the simulated trajectory matches with the experiment much more closely over the second half of the revolution than over the first half. The corresponding plots comparing simulated and experimental data for the other five trials are shown in Figs. 5.10-5.14.

The offset angles for Figs. 5.9-5.14 were 147, 131, 318, 126, 136, and 139 deg, respectively. It seems that the experimental results for the third incline trial were slightly closer to the simulation conducted with the initial system parameter guesses (based on the hammer test and dynamometer measurements) when the experimental results were shifted by the opposite offset angle (about 180 deg different) from the angle used to shift the experimental results of the other trials. Because the simulation conducted with the initial parameter guesses included no tooth asymmetry, it seems to be nearly a matter of chance as to which simulated tooth aligns most closely with which experimental tooth. The offset angle affects which tooth has the more significant force coefficient estimates.

The largest tool deflections of the comparison revolution from each trial (as shown in Figs. 5.9-5.14) correspond with the more significant tooth in each trial in Table 5.2, indicating that the EKF accommodates the deflection asymmetry with asymmetric tooth coefficient estimates. It remains unclear, however, why the offset angles vary so greatly from one trial to another. For example, the first incline trial has a much different offset angle than the other trials, but it falls closer to the majority of the other trials than to the outlier (318 deg). Nevertheless, the EKF estimated that the second tooth was more significant for this trial, unlike most of the other trials.

Though attempts were made to maintain the same conditions for each trial, it is possible that the piece of tape applied to the tool to reflect the laser tachometer fell off between trials (especially due to oil leakage from the spindle), in which case a new piece of tape may have been applied at a different angle. It is not believed that the tape was reapplied between these trials, but if it were, this might explain why the offset angles vary. Though it is expected that runout would cause one tooth to consistently gouge the workpiece more deeply than the other, regardless of initial conditions, perhaps the deflection magnitude of each tooth is also affected by the initial condition (i.e., which tooth entered the cut first). If initial condition plays such a significant role, it might be expected that the more significant tooth would be different in each trial.

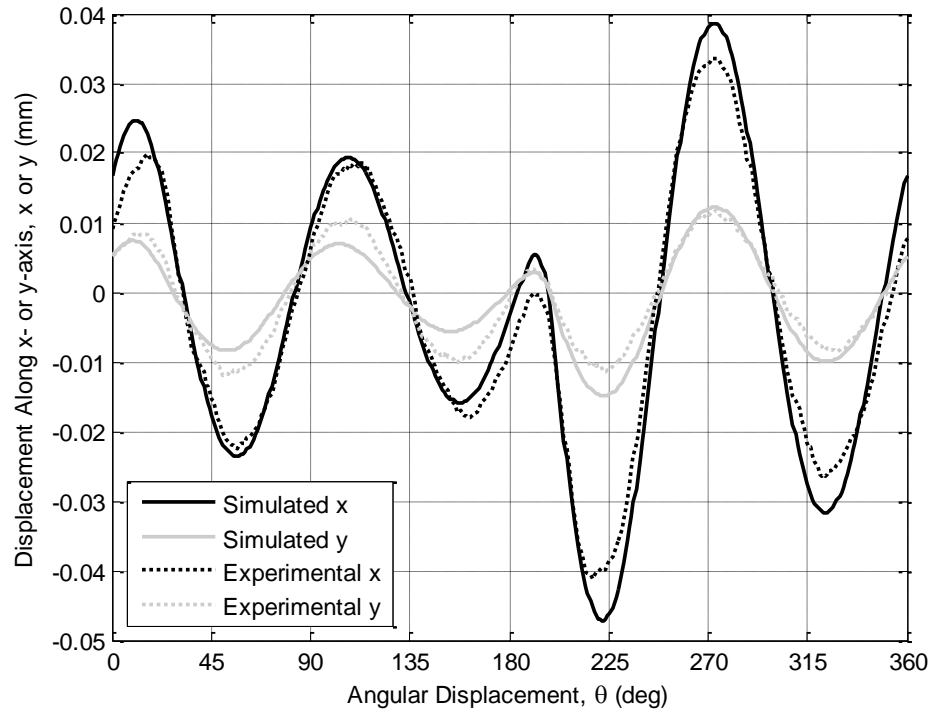


Figure 5.9. Comparison of simulated and experimental (from incline trial #1) tool deflection trajectories over a single revolution at an axial depth of cut near 2 mm.

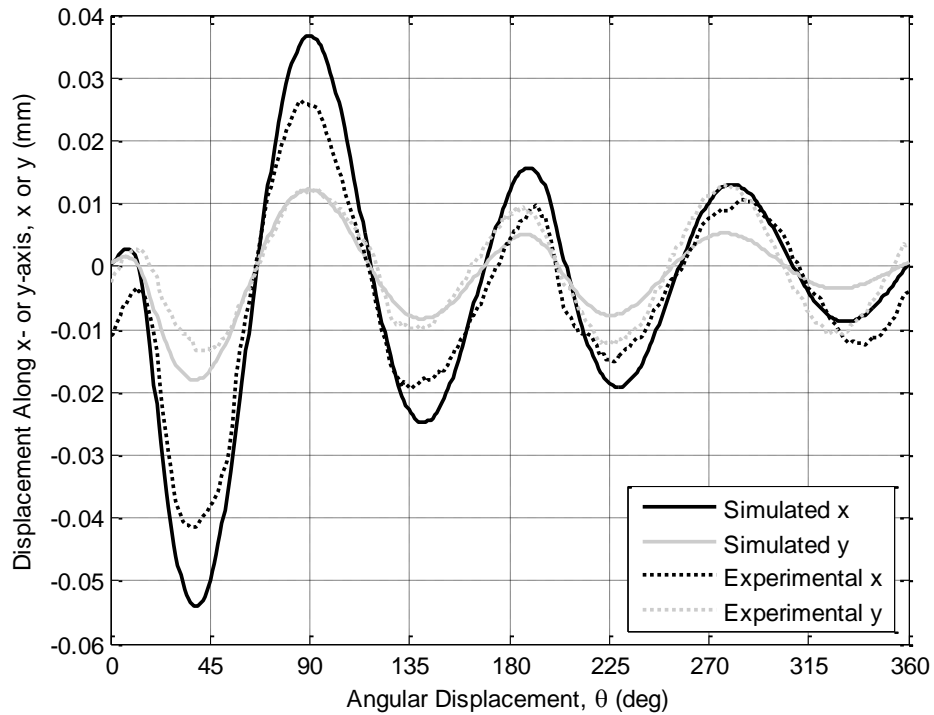


Figure 5.10. Comparison of simulated and experimental (from incline trial #2) tool deflection trajectories over a single revolution at an axial depth of cut near 2 mm.

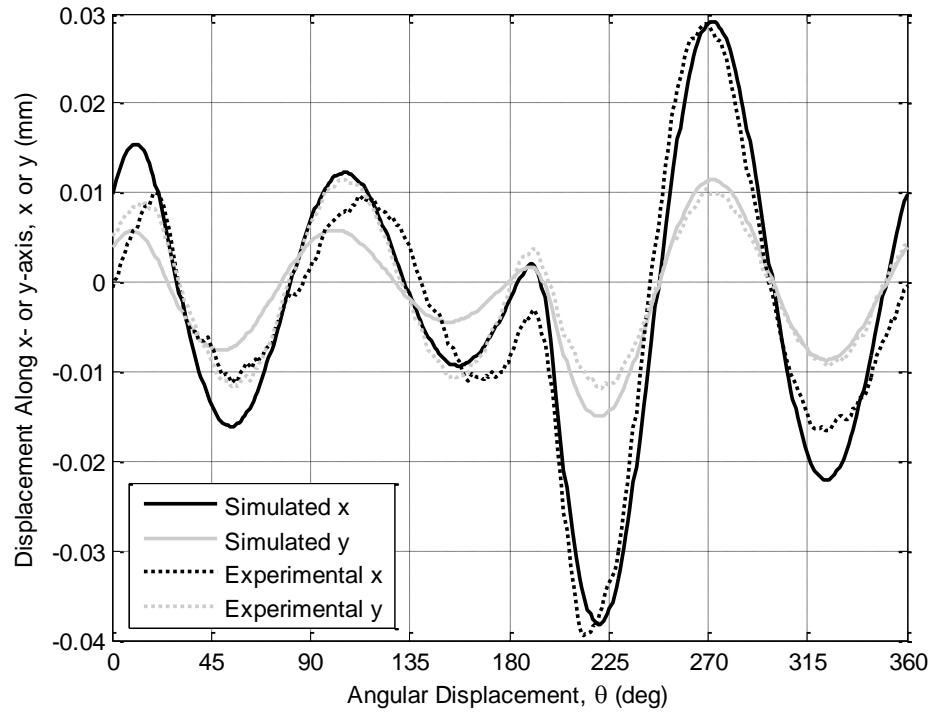


Figure 5.11. Comparison of simulated and experimental (from incline trial #3) tool deflection trajectories over a single revolution at an axial depth of cut near 2 mm.

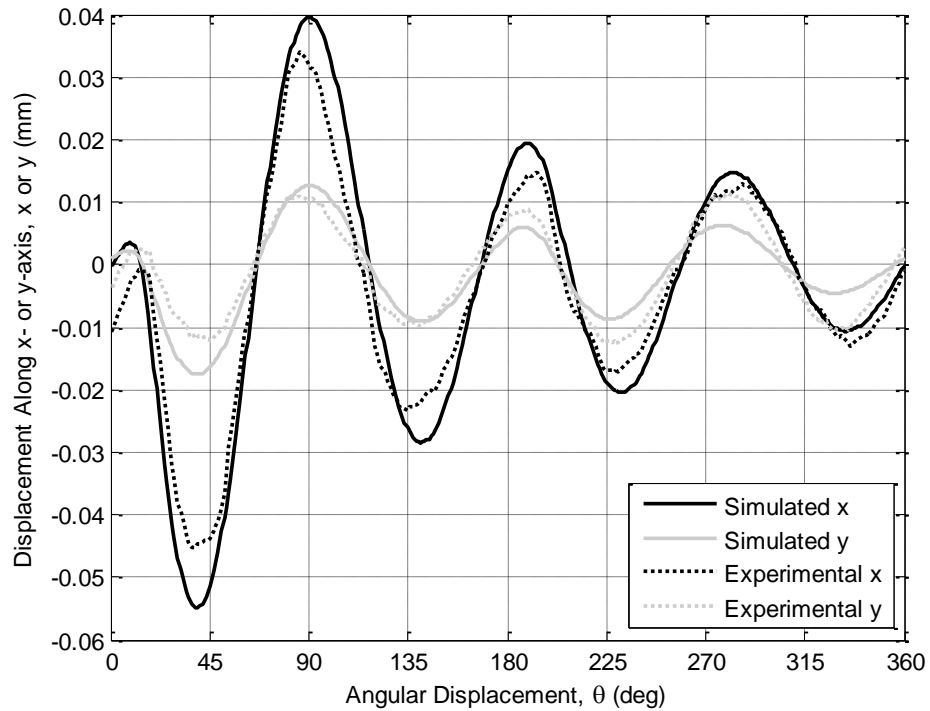


Figure 5.12. Comparison of simulated and experimental (from decline trial #1) tool deflection trajectories over a single revolution at an axial depth of cut near 2 mm.

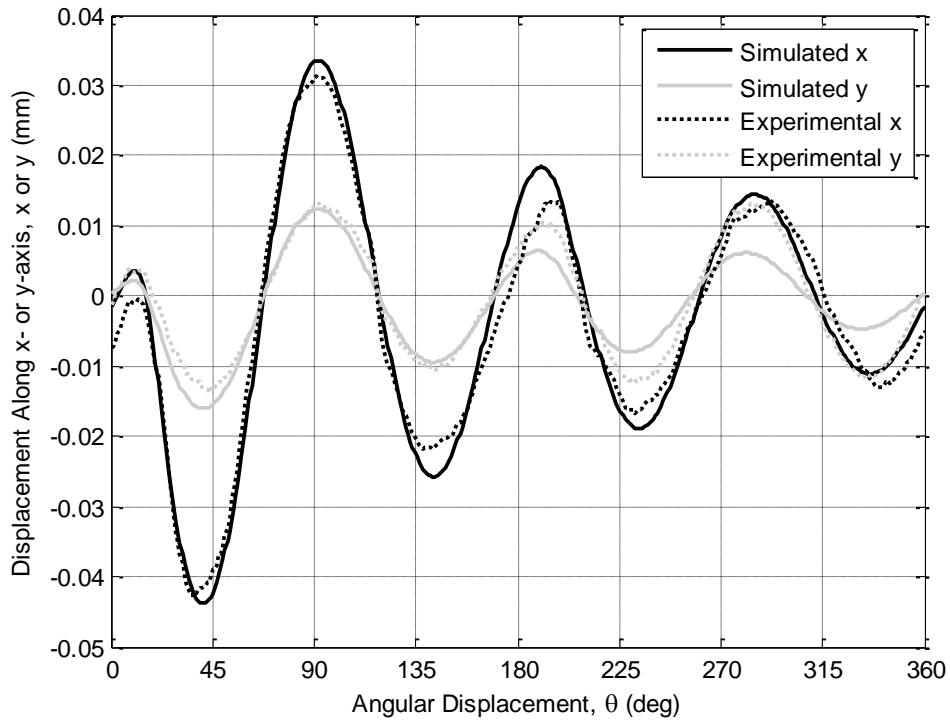


Figure 5.13. Comparison of simulated and experimental (from decline trial #2) tool deflection trajectories over a single revolution at an axial depth of cut near 2 mm.

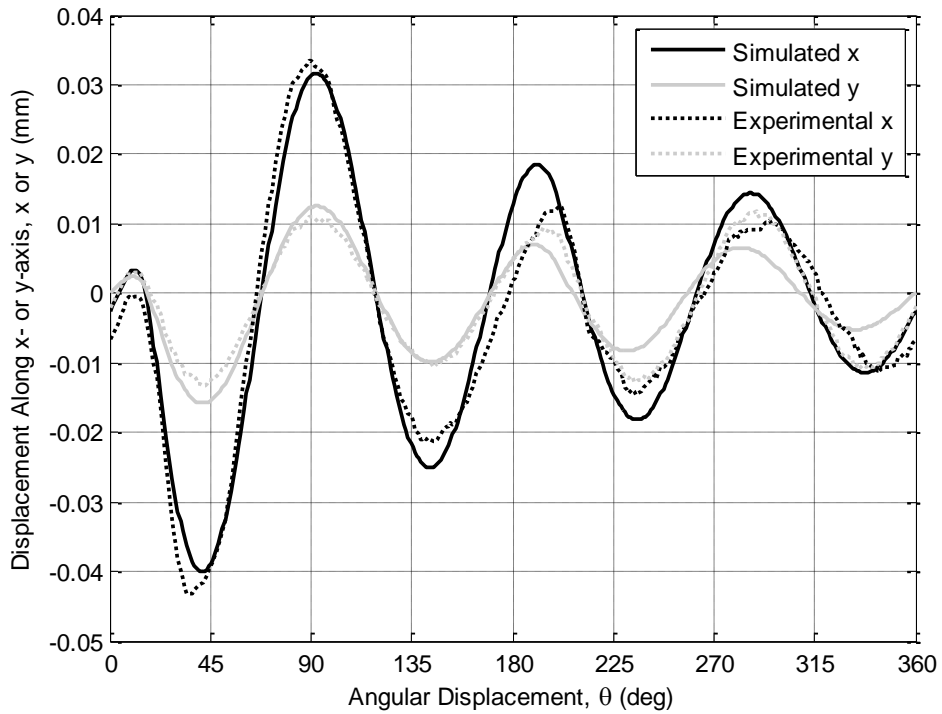


Figure 5.14. Comparison of simulated and experimental (from decline trial #3) tool deflection trajectories over a single revolution at an axial depth of cut near 2 mm.

TFEA stability analysis [11] and the Altintas/Budak method [10], which uses Fourier-series expansions of force coefficients, were also used to calculate the bifurcation point of the tool-workpiece system, but these approaches yielded bifurcation points that were significantly different (either higher or lower, depending on the parameters used) from those in Table 5.1. This difference could be due to significant tooth asymmetry in the experimental trial used in Section 5.1 (i.e., incline trial #1). It was not immediately clear how such asymmetry should be accounted for in these approaches, as they assume a single pair of cutting force coefficients. If tooth asymmetry could be included in these approaches, however, they would potentially provide much faster predictions of chatter stability than the numerical tooth-trajectory simulations used in this chapter. Though these analytical approaches could provide an approximate location of the bifurcation boundary, the width of the hysteresis zone would remain unknown. One advantage of numerical trajectory simulations, therefore, lies in the ability to simulate hysteresis.

Table 5.2 gives the resulting system parameter estimates corresponding to the simulated bifurcation points given in Table 5.1. Light gray cells indicate the cutting force coefficients of the more significant tooth. The more significant tooth always had a greater tangential coefficient estimate than a radial coefficient estimate. The less significant tooth always shared this relationship between coefficients except in the case of the third decline trial, in which the estimated radial coefficient was slightly greater than the estimated tangential coefficient. The reason for such a vast difference between the cutting force coefficient estimates of the two teeth in each trial remains unclear. Though tool asymmetry is likely present in the experimental trials, the magnitude of difference here (sometimes a factor of twenty from the less to the more significant tooth) seems to

be implausible. Perhaps the EKF is compensating for some fundamental oversight in the model (such as a lack of inertial forces, as discussed in Chapter 7, or a lack of feedback effects in the EKF structure, as discussed in Section 4.4).

Despite the wide variation in estimated cutting force coefficients for the various trials (from 3.978×10^9 N/m² to 6.641×10^9 N/m² for the tangential coefficients of the most significant teeth, and from 2.852×10^9 N/m² to 4.154×10^9 N/m² for the corresponding radial coefficients), the modal mass and stiffness estimates varied surprisingly little. Modal mass ranged from 0.03107 kg to 0.03172 kg (except the outlier of the first decline trial at 0.02726 kg), and modal stiffness ranged from 0.9558×10^6 N/m to 0.9840×10^6 N/m (except the outlier of the first decline trial at 0.8487×10^6 N/m), both differences of less than 3 percent (the outliers were still less than 15 percent lower than the other trials). Modal damping varied more widely from 22.21 kg/s to 42.22 kg/s, but this should be expected given the lower sensitivity of stability boundaries to modal damping than to the other modal parameters (see Section 4.2). Furthermore, these extreme values appeared to be outliers, where the other trials ranged from 26.20 to 31.66 kg/s.

Table 5.2. System parameter estimates from experimental trials. Light gray cells indicate cutting force coefficients of the more significant tooth.

System Parameter Estimates	Trial #					
	Incline			Decline		
	1	2	3	1	2	3
Tangential Coefficient Tooth 1 K_{t1} (10^9 N/m ²)	0.2483	6.638	0.2785	6.165	5.089	4.786
Radial Coefficient Tooth 1 K_{r1} (10^9 N/m ²)	0.2196	4.129	0.2668	3.759	3.488	3.478
Tangential Coefficient Tooth 2 K_{t2} (10^9 N/m ²)	6.641	0.3854	3.978	0.2794	0.2896	0.2330
Radial Coefficient Tooth 2 K_{r2} (10^9 N/m ²)	4.154	0.2946	2.852	0.2516	0.2525	0.2376
Modal Mass m_x (10^{-3} kg)	31.34	31.07	31.72	27.26	31.40	31.69
Modal Damping c_x (kg/s)	22.21	42.22	30.25	31.66	29.47	26.20
Modal Stiffness k_x (10^6 N/m)	0.9840	0.9558	0.9630	0.8487	0.9717	0.9830

It should be noted that the simulated bifurcation points in Table 5.1 can be modified by adjusting the modal damping of the simulations to attempt to match the bifurcation behavior of the experimental trials. For instance, by replacing the estimated damping in the first incline trial (22.21 kg/s) with a greater damping value of 28 kg/s, a deeper bifurcation depth was observed in the simulation (3.6 mm, which is much closer to the experimental value of 3.8 mm, instead of 2.1 mm with the EKF estimated damping value). Similarly, by replacing the estimated damping in the second incline trial (42.22 kg/s) with a smaller damping value of 30 kg/s, a shallower bifurcation depth was observed in the simulation (3.5 mm, which is much closer to the experimental value of 3.3 mm, instead of >6 mm with the EKF estimated damping value). The resulting bifurcation behavior is sometimes unexpected, however.

For example, by replacing the estimated damping in the first decline trial (31.66 kg/s) with a lower damping value of 26 kg/s, a much shallower bifurcation depth was observed, but chatter was maintained only briefly before disappearing again. Figure 5.15 illustrates the once-per-revolution tool deflection behavior that results from this decreased damping in the simulation. The result appears to indicate the presence of a chatter island or overhanging stability lobe, an occurrence of chatter over a limited range of axial depths of cut and above which chatter disappears until the next stability boundary is reached. Such islands and lobes exist in analytical stability diagrams in literature (e.g., see overhanging lobe in stability diagrams in [19]), but it may be difficult to generate an analytical stability diagram for this particular case, given the difficulty of implementing asymmetric teeth in the analytical methods used to produce such diagrams. Nevertheless, whereas the simulated bifurcation point was greater than 6 mm axial depth of cut (i.e., no chatter is present in the trial) with the estimated system parameters, chatter appears and disappears in the simulation with the reduced modal damping (disappearing near 2.9 mm, which is close to the experimental bifurcation point of 2.8 mm).

The first decline experimental trial does not indicate the presence of a chatter island or overhanging lobe (unless the island or lobe is larger than can be viewed throughout the range of depths employed in the trial), so there appears to be a fundamental difference between the bifurcation behavior of the simulation in Fig. 5.15 and the behavior exhibited in the experiment. Therefore, adjusting damping to modify the bifurcation point of the simulation may not be the best approach to reconciling the simulation with the experiment. Furthermore, damping seems to have a more complex effect on stability boundaries than was found in Section 4.2 (Fig. 4.1), since further

reduction of damping resulted in an expansion, not just a translation, of the chatter zone, as in Fig. 5.16. Perhaps to achieve more accurate system parameter estimates would require a revision of the EKF structure (e.g., including inertial forces or feedback effects).

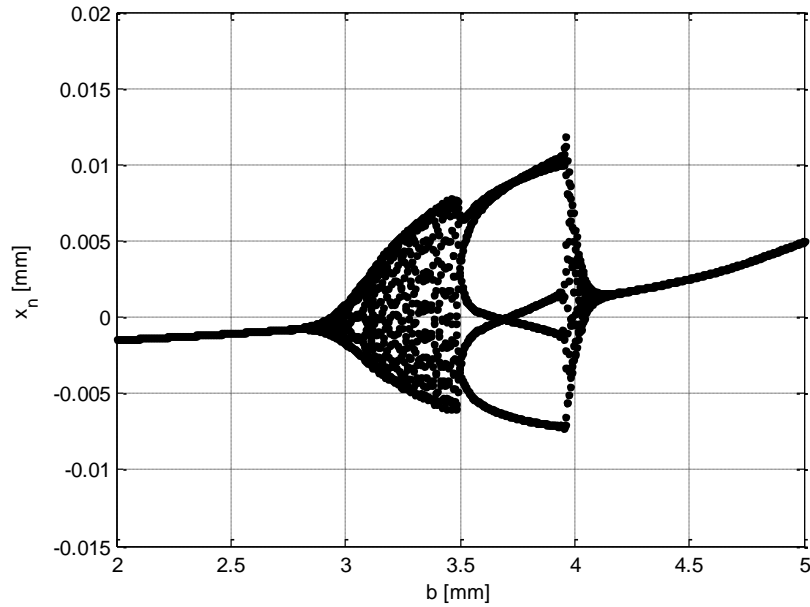


Figure 5.15. Once-per-revolution tool deflection results of simulation with system parameters from Table 5.2 for decline trial #1, except damping is reduced to 26 kg/s.

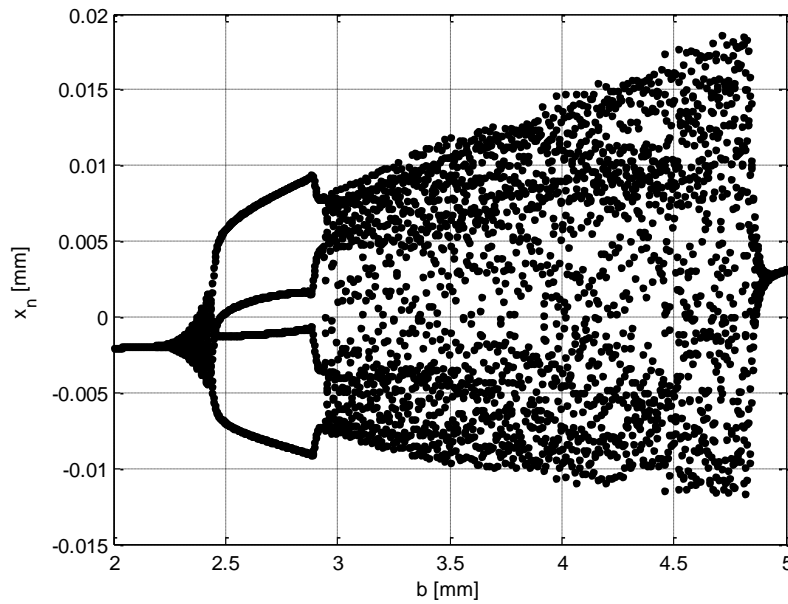


Figure 5.16. Once-per-revolution tool deflection results of simulation with system parameters from Table 5.2 for decline trial #1, except damping is reduced to 24 kg/s.

CHAPTER 6: ESTIMATES

6.1. EKF Modal Parameter Estimation

Two EKF structures were described in Section 4.3 to estimate modal parameters. The first structure used only x -axis measurements, and the second used both x - and y -axis measurements. Both structures were tested on simulated and experimental data to determine how well they converged on the values given in Table 5.2 (Section 5.3) for the first incline trial.

First the x -only structure was tested. The covariance matrices of process and measurement noise, \mathbf{Q}_k and \mathbf{R}_k , respectively, had to be defined. The values chosen for these matrices were based directly on the values used in Kennedy [35], so the matrices were

$$\mathbf{Q}_k = \begin{bmatrix} 10^{14} & 0 & 0 & 0 \\ 0 & 0.1 & 0 & 0 \\ 0 & 0 & 0.1 & 0 \\ 0 & 0 & 0 & 0.1 \end{bmatrix} \quad (6.1)$$

and

$$\mathbf{R}_k = [5]. \quad (6.2)$$

Kennedy found that the values selected for these matrices resulted in good tool deflection estimates by the EKF (i.e., the estimates matched the experimental measurements well),

indicating that the experimental measurements were sufficiently weighted, while the modal parameters could still be estimated accurately (compared to the values used in the simulation), indicating that the internal model was also sufficiently weighted. Decreasing the measurement noise would place additional weight on the external measurements, whereas decreasing the process noise would place additional weight on the internal model.

Before running the EKF, the *a posteriori* covariance matrix of estimation error \mathbf{P}_k^+ also had to be given an initial value. Again the values chosen were those in Kennedy [35]. These values were selected for this study with the purpose of producing system parameter estimates that converged accurately and repeatedly in less than 0.2 s to values as close to those used in the simulation as possible, even when given a wide range of initial parameter estimates. The length of measurement data given to the EKF (0.2 s) was also selected based on Kennedy and the desire to estimate system parameters in a real-time estimation system soon after beginning a cut. The initial value of \mathbf{P}_k^+ used here was

$$\mathbf{P}_k^+ = \begin{bmatrix} 10^{12} & 0 & 0 & 0 & 0 \\ 0 & 10^{12} & 0 & 0 & 0 \\ 0 & 0 & 10^8 & 0 & 0 \\ 0 & 0 & 0 & 10^{22} & 0 \\ 0 & 0 & 0 & 0 & 5 \times 10^{13} \end{bmatrix}. \quad (6.3)$$

The initial value of \mathbf{P}_k^+ can speed up or slow down convergence of parameter estimates. Increasing initial covariances results in increasingly erratic behavior of the parameter estimates, resulting in severely inaccurate estimates before finally settling down, whereas decreasing initial covariances results in slowing down the motion of the parameter

estimates. If initial covariance is decreased excessively, the parameter estimates move slowly enough that they will not converge within the desired 0.2 s.

To make the simulated tool deflection measurement data more realistic and to demonstrate the ability of the EKF to remove noise, Gaussian noise was added to the measurement data with a standard deviation of 5×10^{-7} m. A sample of measurement data that was 0.2 s long and had an axial depth of cut near 2 mm was selected for input to the EKF. This selected data was re-sampled by spline-fit interpolation to have a time step of 5×10^{-7} s (one fifth of the original time step of 2.5×10^{-6} s) to improve accuracy of estimates. The EKF uses a locally linearized version of the nonlinear system, so a smaller step size improves the accuracy of estimates (until numerical precision error takes over) by providing a higher-resolution approximation of the nonlinear system.

The initial estimates of tool deflection and velocity given to the EKF were set at zero, but the initial estimates of the modal parameters were given the same randomized values that were used in Chapter 5 (approximately $K_{t1} = 1.493 \times 10^8$ N/m², $K_{r1} = 2.315 \times 10^8$ N/m², $K_{t2} = 4.257 \times 10^9$ N/m², $K_{r2} = 3.106 \times 10^9$ N/m², $m_x = 0.02270$ kg, $c_x = 40.56$ kg/s, and $k_x = 1.162 \times 10^6$ N/m). The errors of these initial values (especially the initial force coefficient values) with respect to the corresponding estimated values of Table 5.2 vary from nearly -100 percent to well above 1000 percent, depending on the parameter and the trial. The ability of the EKF to recover from extremely inaccurate initial guesses indicates that it does not require accurate knowledge of the parameters beforehand and could potentially operate even with extremely worn tools or unusual cutting conditions. The initial state and parameter estimates were assigned to $\hat{\mathbf{x}}_{k-1}^+$ prior

to the first iteration of the EKF, and force coefficients were set equal to those in Table 5.2 for the first incline trial.

The modal parameter estimates produced by the EKF from simulated measurements are displayed in Fig. 6.1. The modal parameter estimates are represented in terms of percent error from the values used in the simulation corresponding to the first incline trial (see Section 5.1 for how these parameters were identified). The time axis in these figures represents the part of the sample of selected data (0.2 s long) that was the current input to the EKF at the time of the corresponding parameter estimate. No estimates are shown for a time of zero or a time of 0.2 s because the data sample was cropped by two revolutions at the beginning and end during data processing.

The EKF modal parameter estimates in Fig. 6.1 converge in less than 0.2 s (of measurement data) to errors less than 2.5 percent. The greatest steady-state error occurs in the modal damping estimate. As shown in Fig. 4.1 in Section 4.2, modal damping also appeared to have the least effect of the three parameters on stability boundaries for a 1.5 percent change in the parameter. It is possible that damping also has the least effect of the three parameters on tool deflection in general, in which case the decreased sensitivity of tool deflection to modal damping may explain why the estimation error of modal damping is greater than that of the other parameters. It should also be noted that the modal mass and stiffness estimates are very closely correlated in their behavior in Fig. 4.1 and lie nearly on top of one another through most of the plot. The reason for this phenomenon is unknown, but similar phenomena have been observed when including y-axis measurements in the EKF structure and estimating all three parameters, as well as when including y-axis measurements and only estimating modal mass and stiffness.

Hence, the correlation of the modal mass and stiffness estimates does not appear to be associated with the observability of the entire system.

For comparison, Fig. 6.2 shows the EKF estimates of modal parameters when given simulated tool deflection measurements along both the x - and the y -axes (i.e., using the second EKF structure described in Section 4.3). As in Fig. 6.1, the estimates converge to less than 2.1 percent error within 0.2 s of measurement data. The initial estimates in Fig. 6.2 are the same as those used in Fig. 6.1, but there still remain larger errors in the early part of the plot. Modal damping is again the parameter with the greatest estimation error overall, and the modal mass and modal stiffness estimates appear to track together quite closely as before.

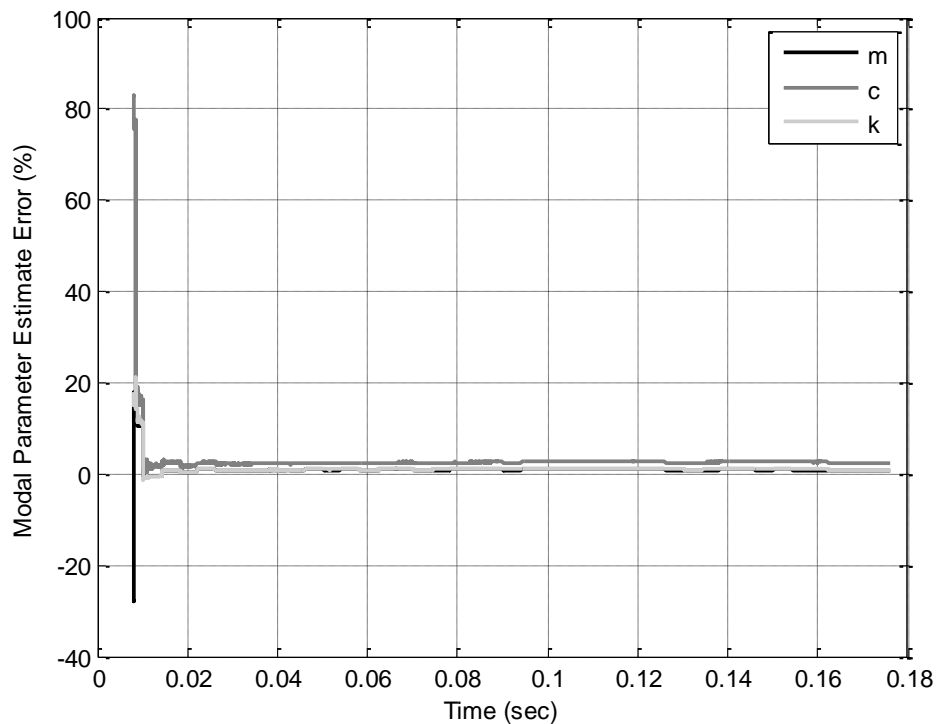


Figure 6.1. Modal parameter estimates when the EKF is given simulated tool deflection measurements along only the x -axis.

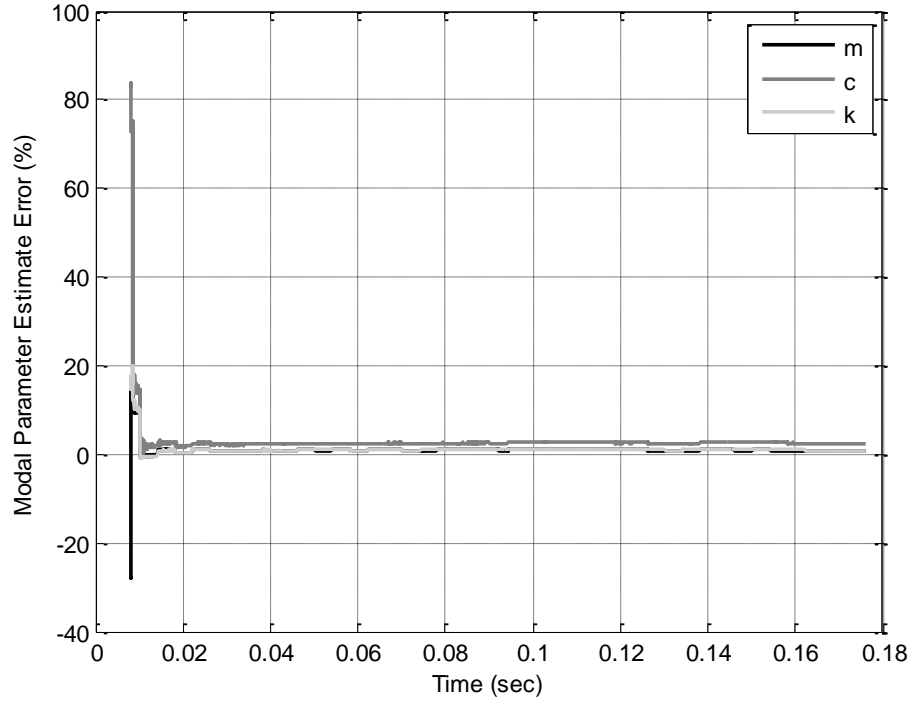


Figure 6.2. Modal parameter estimates when the EKF is given simulated tool deflection measurements along both the x - and y -axes.

The second EKF structure described in Section 4.3 made use of y -axis measurements to improve observability of the system. The covariance matrices of process and measurement noise, \mathbf{Q}_k and \mathbf{R}_k , respectively, were again defined based on the values used in Kennedy [35] (see Eqs. (6.1) and (6.2)), except that the matrices were expanded to allow for tool deflection estimation and measurement along the y -axis as well. The resulting matrices were

$$\mathbf{Q}_k = \begin{bmatrix} 10^{14} & 0 & 0 & 0 & 0 \\ 0 & 10^{14} & 0 & 0 & 0 \\ 0 & 0 & 0.1 & 0 & 0 \\ 0 & 0 & 0 & 0.1 & 0 \\ 0 & 0 & 0 & 0 & 0.1 \end{bmatrix} \quad (6.4)$$

and

$$\mathbf{R}_k = \begin{bmatrix} 5 & 0 \\ 0 & 5 \end{bmatrix}. \quad (6.5)$$

Again the initial values of the *a posteriori* covariance matrix of estimation error \mathbf{P}_k^+ reflected those in Kennedy [35], but the matrix was expanded to allow for the *y*-axis states. The initial value of \mathbf{P}_k^+ used here was

$$\mathbf{P}_k^+ = \begin{bmatrix} 10^{12} & 0 & 0 & 0 & 0 & 0 & 0 \\ 0 & 10^{12} & 0 & 0 & 0 & 0 & 0 \\ 0 & 0 & 10^{12} & 0 & 0 & 0 & 0 \\ 0 & 0 & 0 & 10^{12} & 0 & 0 & 0 \\ 0 & 0 & 0 & 0 & 10^8 & 0 & 0 \\ 0 & 0 & 0 & 0 & 0 & 10^{22} & 0 \\ 0 & 0 & 0 & 0 & 0 & 0 & 5 \times 10^{13} \end{bmatrix}. \quad (6.6)$$

Gaussian noise, measurement re-sampling, and initial estimates were all applied as before.

To test the EKF structures on experimental data, tool deflection measurements were recorded from two capacitive sensors with the experimental setup described in Section 3.1. A laser tachometer provided a voltage pulse at the same point in each revolution, which allowed the deflection data to be paired with the corresponding angular displacement of the tool at each time step. All three sensors were recorded in LabVIEW[®] at 100 kHz, which means the time step was 1×10^{-5} s. As with the simulated data given to the EKF, a 0.2-s sample of experimental data was selected with axial depth of

cut near 2 mm. The simulated and experimental data were synchronized over a single revolution, as described in Section 5.1, so the EKF could calculate cutting forces at the same time steps in which teeth were engaged in the experiment. The selected data was re-sampled as the simulated data to a smaller time step of 5×10^{-7} s (5 percent of the original experimental time step) to attempt to improve estimation accuracy.

The noise covariance matrices were selected as before in Eqs. (6.1) and (6.2), and the *a posteriori* covariance matrix of estimation error was initialized as before in Eq. (6.3). The state and parameter estimates were initialized with the same values used in Fig. 6.1. The resulting EKF estimates of modal parameters, given experimental tool deflection measurements, are shown in Fig. 6.3. Percent error is again defined in terms of the values used in the simulation and identified in Section 5.1. Two revolutions have again been cropped from the beginning and the end of the data during processing as in Fig. 6.1.

The modal parameter estimates in Fig. 6.3, based on experimental measurements, exhibit more severe error swings than those in Figs. 6.1 and 6.2, which were based on simulated measurements. The modal damping estimate, in particular, exhibits error as great as 136 percent and as low as -125 percent (i.e., the damping estimate is actually a negative value) briefly, and converges a bit more slowly than the other parameters. It seems the EKF has more difficulty extracting accurate modal parameter estimates from the experimental deflection measurements than from the simulated measurements. Nevertheless, all three parameter estimates end the trial within 2.3 percent of the values identified in Section 5.1, with damping at -0.2 percent. The modal mass and stiffness estimation errors correlated fairly well again, as when the EKF used simulated data.

Figure 6.4 shows the modal parameter estimates produced by running the second EKF structure, which uses measurements from both axes, on the same experimental data as in Fig. 6.3. The experimental data was prepared as before for the first (i.e., the x -only) EKF, using the same initial estimates as before. Estimation error is again given with respect to the parameter values used in the simulation and identified in Section 5.1. The parameter estimates behaved much like those in Fig. 6.3 (i.e., with only x -axis experimental measurements). Mass and stiffness estimates ended more accurately this time (within 1.6 percent of the simulation values), and the final damping estimate was slightly worse at about -3.7 percent. Nevertheless, the maximum damping errors were somewhat less extreme. Once again the modal mass and stiffness estimates correlated well in behavior.

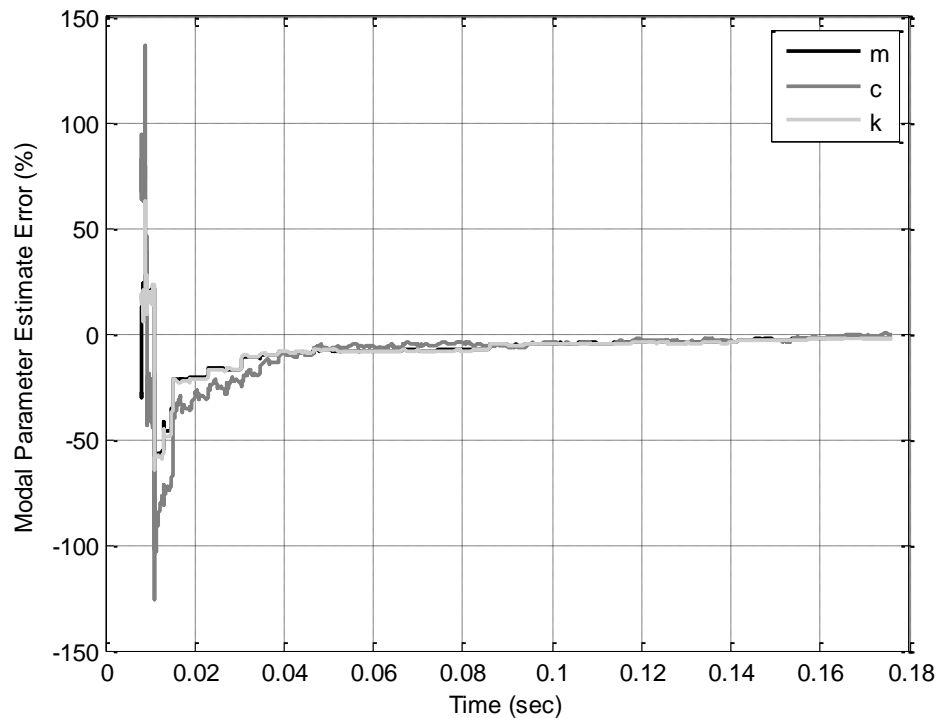


Figure 6.3. Modal parameter estimates when the EKF is given experimental tool deflection measurements along only the x -axis.

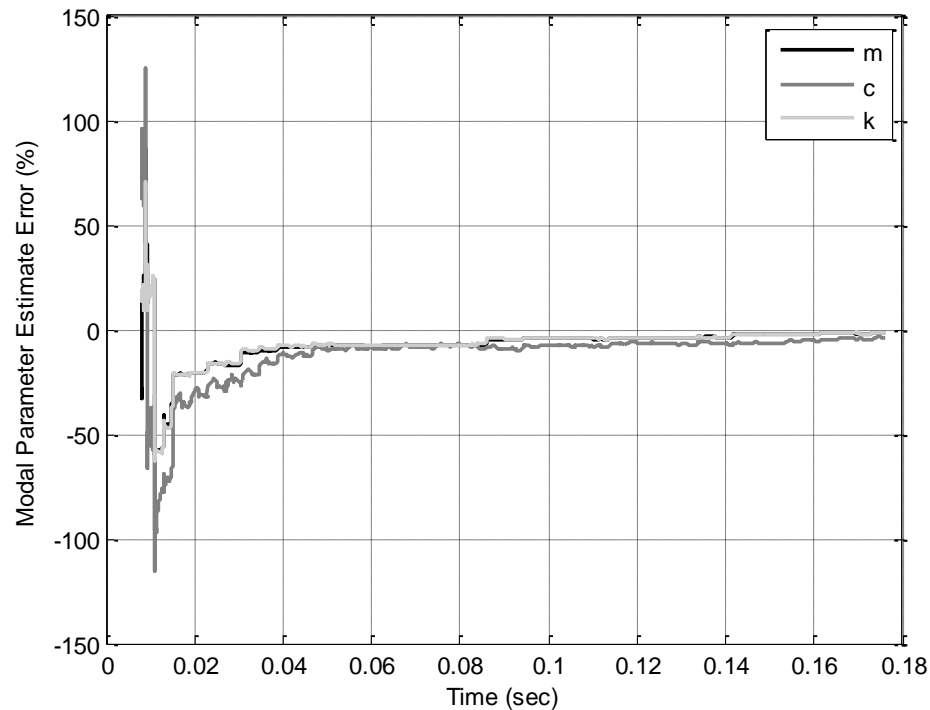


Figure 6.4. Modal parameter estimates when the EKF is given experimental tool deflection measurements along both the x - and y -axes.

All the tests so far in this section have involved unobservable systems. In each instance (Figs. 6.1-6.4) the number of unknown parameters to estimate has been greater than the number of measurements being used (i.e., three modal parameters being estimated with measurements along only one or two axes). Therefore, to properly compare EKF performance in modal parameter estimation and cutting force coefficient estimation (as in Section 6.2), tests should be run with an observable system. For this purpose, the second EKF (i.e., using both axes) is tested on simulated and experimental data to estimate only two modal parameters.

Given that, of the three modal parameters, damping appears to have the least effect on stability and its estimation shows the greatest error, damping is here omitted from the EKF structure. Now the system becomes observable, having two unknown

parameters to estimate (mass and stiffness) and two measurements (one along each axis). Omission of damping from the EKF structure was accomplished by removing the rows and columns pertaining to damping from Eqs. (4.15) and (4.17)-(4.19), and by replacing any occurrences of the damping estimate, $\hat{x}_{6,k-1}^+$, in these equations and in Eqs. (4.21) and (4.22) with a constant damping parameter, c_x . The constant parameter was set to the value of damping identified in Section 5.1, and the same initial estimates were used as for the previous tests.

Conducting modal mass and stiffness estimation using measurements along both axes, as in Figs. 6.2 and 6.4, only without estimating damping, resulted in the parameter estimates in Figs. 6.5 and 6.6 for simulated and experimental data, respectively. In Fig. 6.5, the mass and stiffness estimates converged to less than 0.8 percent error within 0.2 s, exhibiting very similar behavior as the mass and stiffness estimates did when all three parameters were estimated (see Fig. 6.2). In Fig. 6.6, the mass and stiffness estimates reached final values within 0.1 percent of the values identified in Section 5.1. The maximum errors in Fig. 6.6 were significantly less severe than those in Fig. 6.4, when all three modal parameters were estimated from experimental data. The mass and stiffness estimates continued to exhibit close correlation in both Figs. 6.5 and 6.6.

The estimation procedure for Fig. 6.6 is almost identical to the estimation procedure in Chapter 5 for the first incline trial, which explains the closeness (characterized by a small percent error) of these estimates to the values identified in Chapter 5. The reason any error occurs at all is likely due to slight differences in manually selecting the cut end point from the data for analysis on these separate occasions.

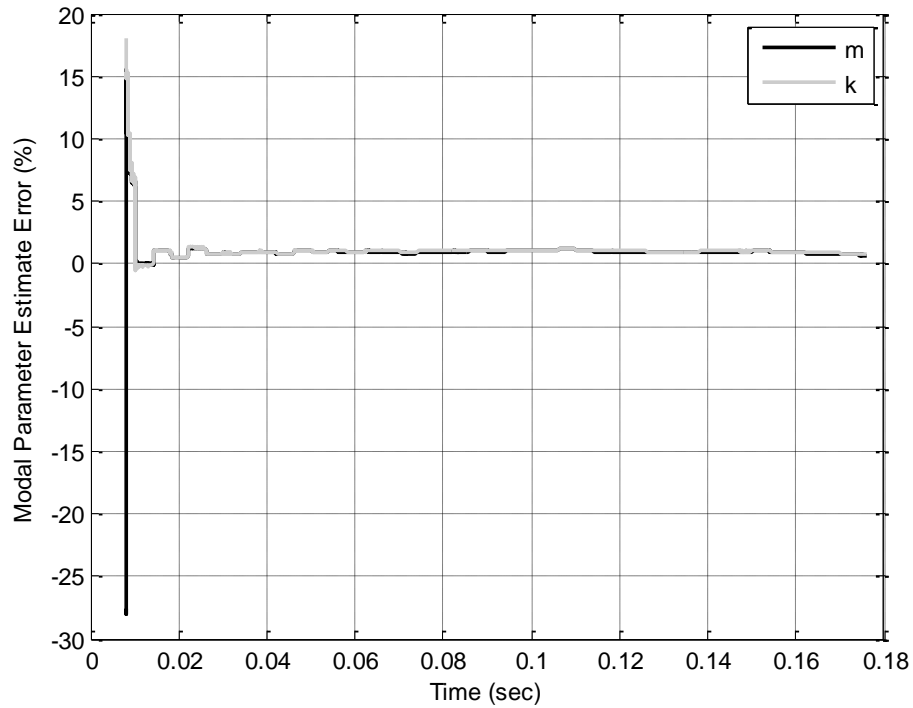


Figure 6.5. Modal mass and stiffness estimates (damping is not estimated) when the EKF is given simulated tool deflection measurements along both the x - and y -axes.

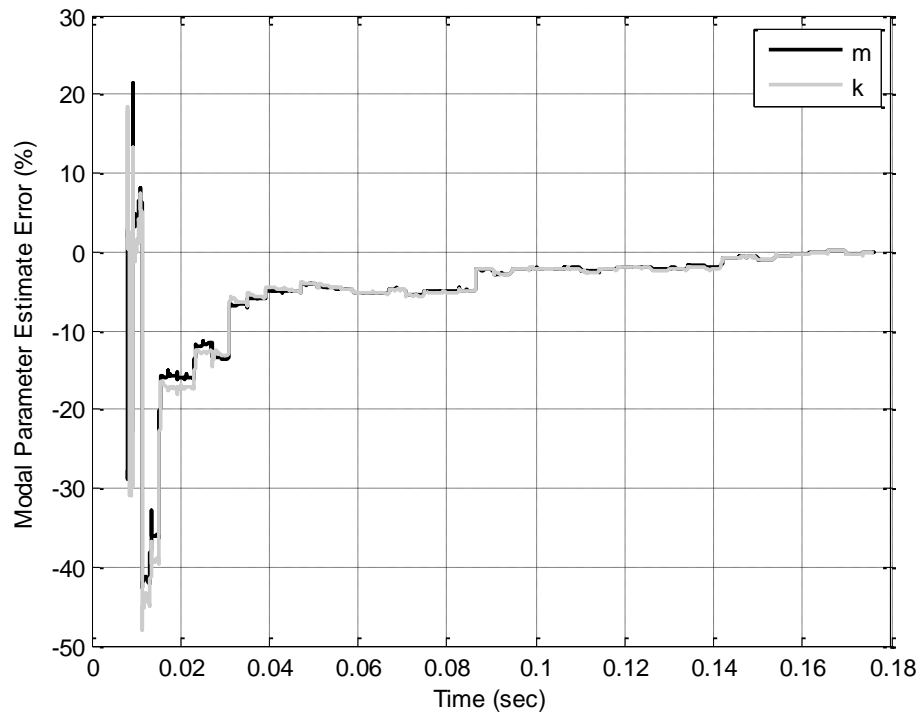


Figure 6.6. Modal mass and stiffness estimates (damping is not estimated) when the EKF is given experimental tool deflection measurements along both the x - and y -axes.

The EKF was also used to estimate modal mass and damping while assuming a constant modal stiffness, once again with an observable system. Omission of stiffness from the EKF structure was accomplished in like manner as the omission of damping was for Figs. 6.5 and 6.6. Instead of replacing the damping estimate, $\hat{x}_{6,k-1}^+$, in system equations with a constant damping parameter, any occurrences of the stiffness estimate, $\hat{x}_{7,k-1}^+$, in the system were replaced with a constant stiffness parameter, k_x . The stiffness parameter was set to the value of stiffness identified in Section 5.1, and the same initial estimates were used as in previous tests.

Modal mass and damping estimation was conducted based on simulated and experimental measurements along both axes, and the resulting estimates are given in Figs. 6.7 and 6.8. Based on simulated measurements, the estimates in Fig. 6.7 behave much as those in Fig. 6.2, with damping ending within 2.5 percent of its identified value instead of 2.1 percent. The modal mass estimate, however, ends closer to its identified value, at about 0.2 percent instead of 0.7 percent error. It is unclear why this improvement exists, except perhaps as a result of the system now being observable, though observability did not improve the estimates of modal mass and stiffness in Fig. 6.5 very significantly over those of Fig. 6.2. The estimates based on experimental data in Fig. 6.8 converge more quickly and have less extreme maximum errors than when all three parameters were estimated in Fig. 6.4. As with Fig. 6.6, the procedure used here is nearly identical to that in Chapter 5, so the final estimates fall within 0.3 percent of the values identified in Chapter 5.

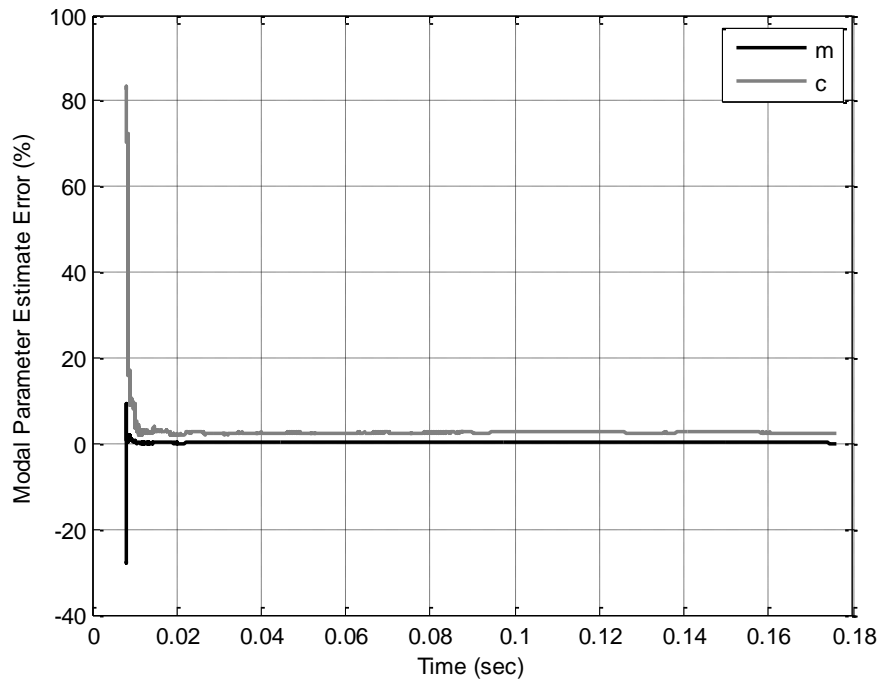


Figure 6.7. Modal mass and damping estimates (stiffness is not estimated) when the EKF is given simulated tool deflection measurements along both the x - and y -axes.

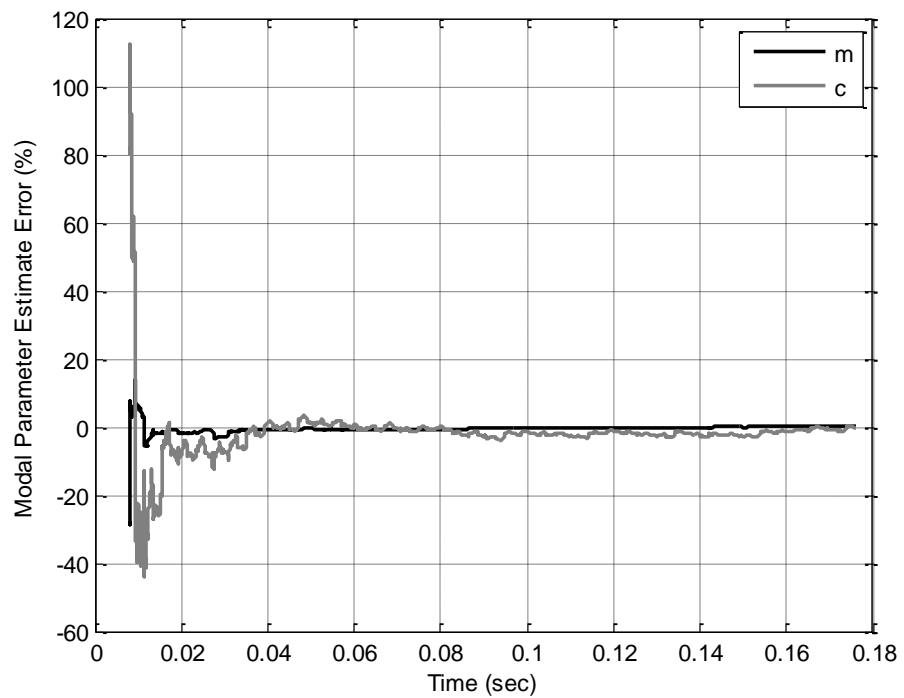


Figure 6.8. Modal mass and damping estimates (stiffness is not estimated) when the EKF is given experimental tool deflection measurements along both the x - and y -axes.

As mentioned in Section 5.3, EKF estimates are affected by sampling rate. Resampling the experimental data to a higher resolution can improve the modal parameter estimates but sometimes actually results in negative estimates. The reason for this error is unclear, but a brief look at the process of resampling the data may provide insight. Recall that noise was added to the simulated tool deflection data and the data was resampled with spline interpolation from its original step size of 2.5×10^{-6} s to a higher-resolution step size of 5×10^{-7} s. The experimental data was also resampled to the same step size from its original step size of 1×10^{-5} s. Figure 6.9 shows an example comparison of the original and resampled noisy data over a very short time span. Note that the spline interpolation has removed much of the roughness of the original noisy data and replaced it with smoother spline fits. The simulated data is also shown resampled with a lower-resolution step size (1×10^{-5} s). This data also exhibits significant roughness.

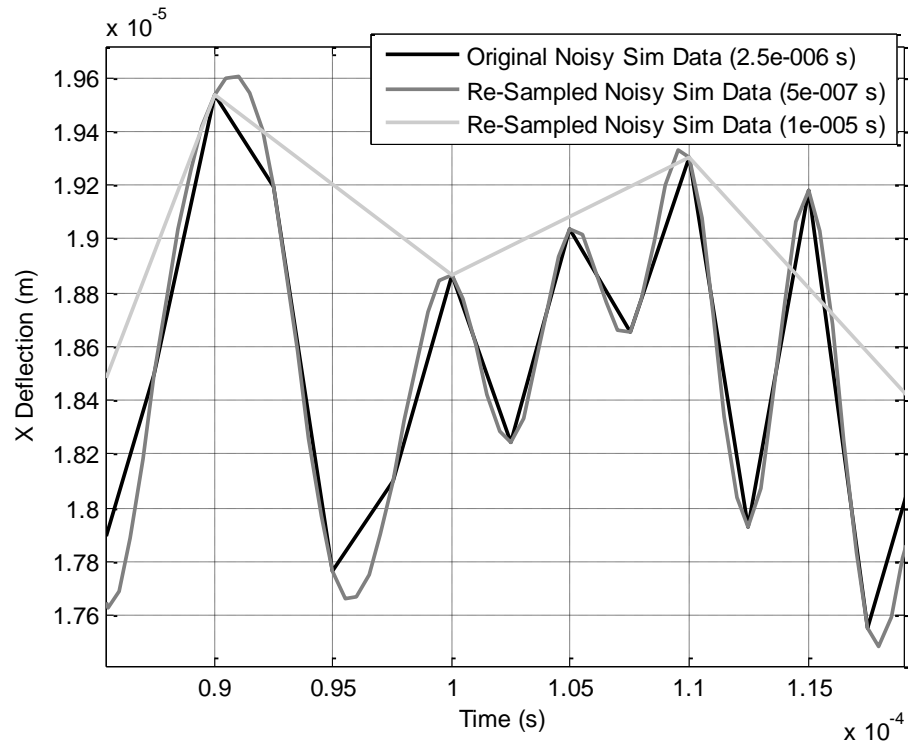


Figure 6.9. Example comparison of original and resampled simulated tool deflection data after the addition of Gaussian noise.

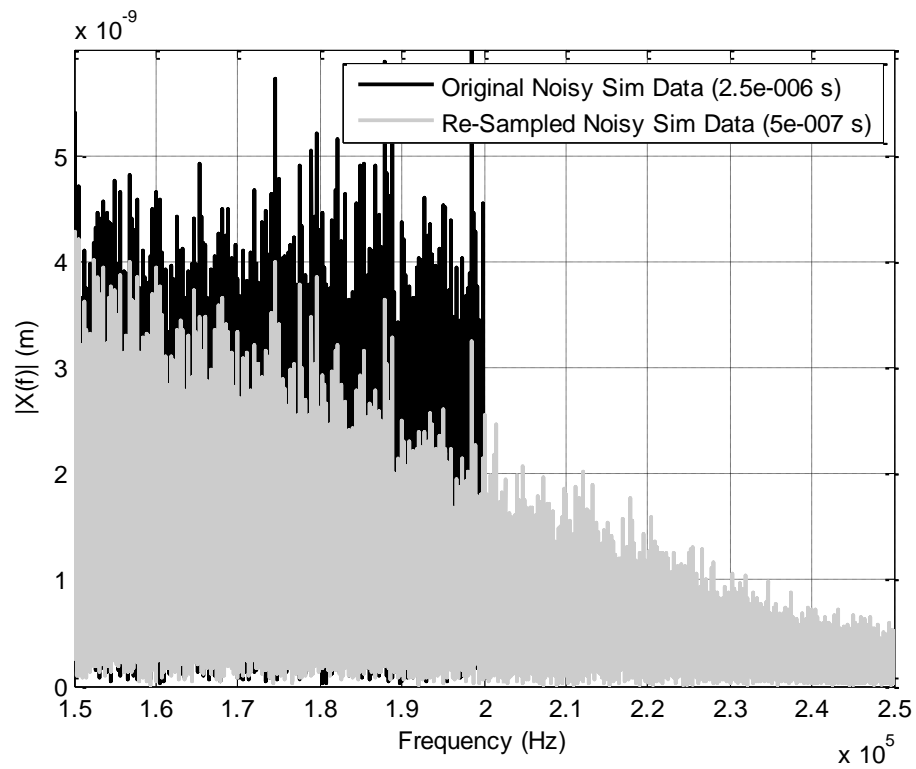


Figure 6.10. Example comparison of single-sided amplitude spectra of original and higher-resolution resampled simulated tool deflection data after addition of Gaussian noise.

Figure 6.10 shows a comparison of the noise floors of the single-sided amplitude spectra of the entire 0.2 s samples of both the original noisy data and the data resampled to a higher-resolution step size of 5×10^{-7} s. Figure 6.10 illustrates that the resampling redistributed the high-frequency noise in the sample. No longer was noise sharply cut off at 2×10^5 Hz (the Nyquist frequency of the original data), but the high-frequency noise prior to this cutoff was diminished in the resampled data. Instead of a sharp cutoff, the resampled data exhibited a gradual dropoff. It is possible that this difference improved the estimation behavior of the EKF.

For comparison, Fig. 6.11 shows the amplitude spectra for the original data and the data resampled to a lower-resolution step size of 1×10^{-5} s. This resampling appeared to raise the noise floor from the original data, as evidenced in Fig. 6.11, where the Nyquist frequency of the resampled data is visible (5×10^4 Hz). This difference in noise characteristics could help explain why the EKF performed less accurately on the lower-resolution simulated data, but if the magnitude of the noise floor made the difference in performance between the original simulated data and the resampled data, then the EKF should also perform better with resampled higher-resolution experimental data than with the original experimental data. As Fig. 6.12 illustrates, the noise floor of the experimental data was decreased by resampling to a higher resolution, as was the case with the simulated data, but the EKF can actually perform less accurately given the higher-resolution resampled data. Therefore, if noise played a role in the different behavior of the EKF given different time steps, it remains unclear what that role was. Perhaps adjusting the process and measurement covariance matrices after resampling would improve EKF performance.

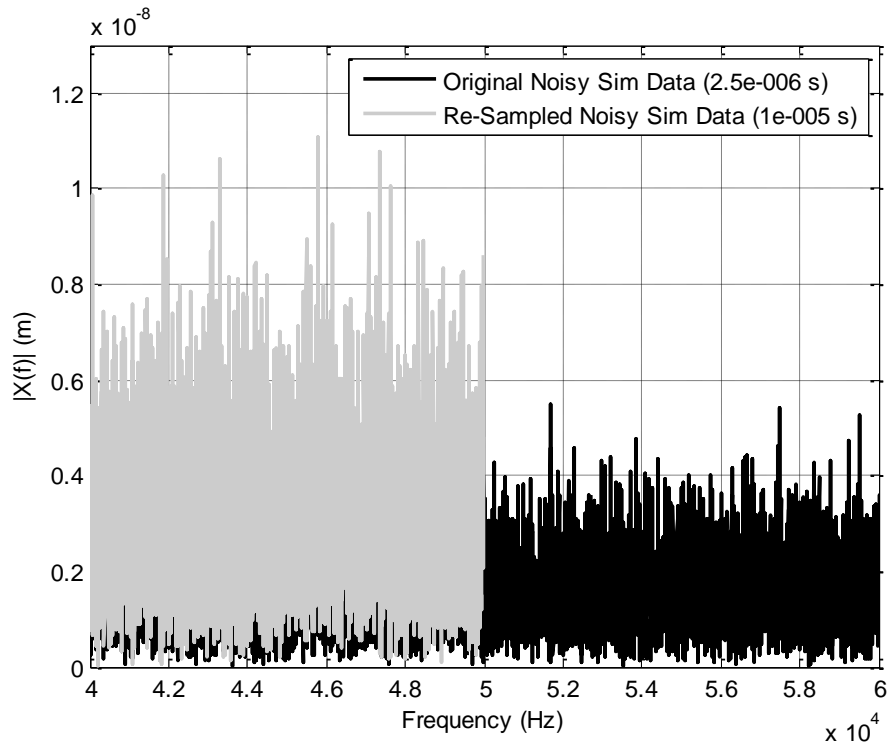


Figure 6.11. Example comparison of single-sided amplitude spectra of original and lower-resolution resampled simulated tool deflection data after addition of Gaussian noise.

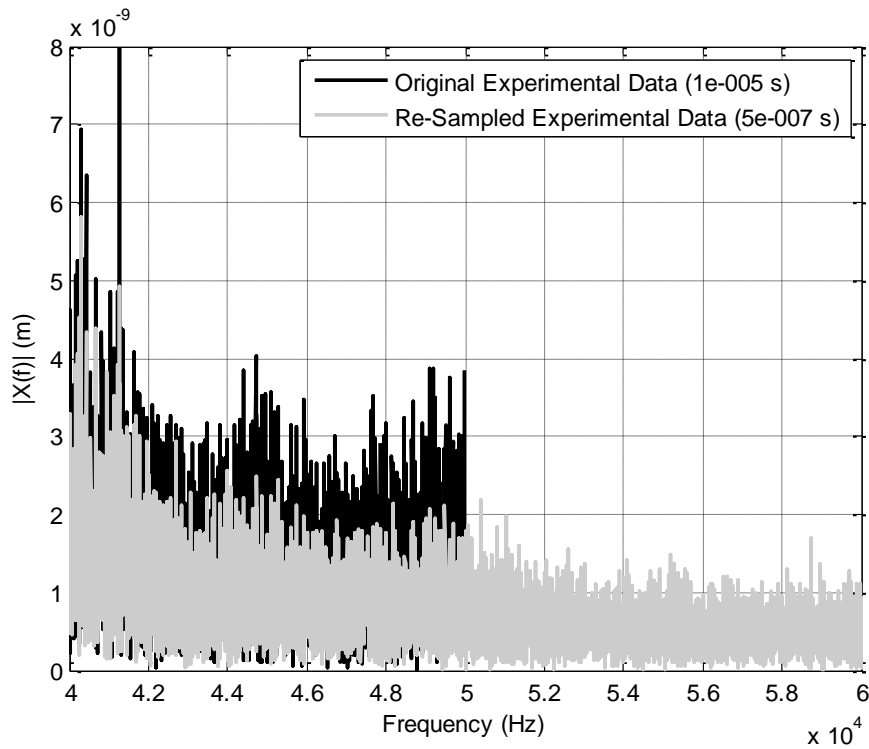


Figure 6.12. Example comparison of single-sided amplitude spectra of original and higher-resolution resampled experimental tool deflection data.

6.2. EKF Cutting Force Coefficient Estimation

The EKF structure described in Section 4.4 was used to estimate cutting force coefficients from simulated and experimental tool deflection measurements along both the x - and y -axes. Tests were run to estimate the cutting force coefficients for the entire tool and also for each tooth separately.

The covariance matrices of process and measurement noise, \mathbf{Q}_k and \mathbf{R}_k , respectively, were defined as in Eqs. (6.4) and (6.5) for direct comparison with the results of the second EKF tested in Section 6.1, which used measurements from both the x - and the y -axes. As in Section 6.1, the values selected for these matrices resulted in good tool deflection estimates by the EKF, indicating that the experimental measurements were sufficiently weighted, while the cutting coefficients could still be estimated accurately (compared to the values used in the simulation), indicating that the internal model was also sufficiently weighted.

As in Section 6.1, the initial values for the *a posteriori* covariance matrix of estimation error \mathbf{P}_k^+ reflected those in Kennedy [35] where possible, but the rows that applied to cutting force coefficient estimation (i.e., the bottom two rows) had to be selected by trial and error. The values in these rows were selected with the purpose of producing cutting force coefficient estimates that converged accurately and repeatedly in less than 0.2 s to values as close to those used in the simulation as possible, even when given a wide range of initial parameter estimates. The length of measurement data given to the EKF (0.2 s) was also selected based on Kennedy [35] and the desire to estimate cutting force coefficients in a real-time estimation system soon after beginning a cut. The initial value of \mathbf{P}_k^+ used here was

$$\mathbf{P}_k^+ = \begin{bmatrix} 10^{12} & 0 & 0 & 0 & 0 & 0 \\ 0 & 10^{12} & 0 & 0 & 0 & 0 \\ 0 & 0 & 10^{12} & 0 & 0 & 0 \\ 0 & 0 & 0 & 10^{12} & 0 & 0 \\ 0 & 0 & 0 & 0 & 10^{29} & 0 \\ 0 & 0 & 0 & 0 & 0 & 10^{29} \end{bmatrix}. \quad (6.7)$$

As in Section 6.1, the initial values of \mathbf{P}_k^+ can speed up or slow down convergence of parameter estimates.

Gaussian noise was again added to the measurement data with a standard deviation of 5×10^{-7} m. A sample of measurement data that was 0.2 s long and had an axial depth of cut near 2 mm was selected for input to the EKF. This selected data was re-sampled by spline-fit interpolation to have a time step of 5×10^{-7} s (one fifth of the original simulation time step of 2.5×10^{-6} s) to improve accuracy of estimates.

The initial estimates of tool deflection and velocity given to the EKF were again set to zero, but the initial estimates of the cutting force coefficients were set to the randomized values used in Sections 5.3 and 6.1. The initial state and parameter estimates were assigned to $\hat{\mathbf{x}}_{k-1}^+$ prior to the first EKF iteration. Modal parameters were set equal to those in Table 5.2 for incline #1.

The cutting coefficient estimates produced by the EKF are displayed in Figs. 6.13 and 6.14, which show the tangential and radial coefficient estimates, respectively. Note that the coefficients were estimated for each tooth separately and are represented in terms of percent error from the values used in the simulation (see Section 5.1 for how these coefficients were identified by running the EKF on experimental data). The time axis in

these figures represents the part of the sample of selected data (0.2 s long) that was the current input to the EKF at the time of the corresponding parameter estimate. No estimates are shown for a time of zero or a time of 0.2 s because the data sample was cropped by two revolutions at the beginning and end during data processing.

The EKF cutting coefficient estimates in Figs. 6.13 and 6.14 converge in less than 0.2 s to within 0.9 percent of the simulation values (and appear as if they might continue to gain accuracy given more measurement data). As mentioned concerning Eq. (6.3), the initial value given to the covariance matrix of estimation error plays a significant role in the time required for convergence of the estimates. Note that, given the initial values in Eq. (6.7) for this matrix, the cutting force coefficient estimates converge very quickly, with all the tangential and radial estimates falling within 2 percent of their respective identified values (see Section 5.1) within 0.025 s of data.

The apparent stepwise behavior shown in Figs. 6.13 and 6.14 should be noted because it illustrates that the cutting force coefficients cease to be observable whenever the respective tooth is disengaged from the workpiece. Only when a tooth is engaged are its cutting force coefficients observable (see Sections 4.4 and 4.5). Once a tooth is engaged, the EKF estimates of its cutting force coefficients may change quickly to reflect the influence of the newest deflection measurements, but the rest of the time, the EKF maintains the latest cutting force coefficient estimates, produced by the last engagement of that tooth. While something of this stepwise behavior could be seen in the modal parameter estimates of Section 6.1, the modal parameter estimates could continue to vary between cuts, whereas the cutting coefficient estimates cannot.

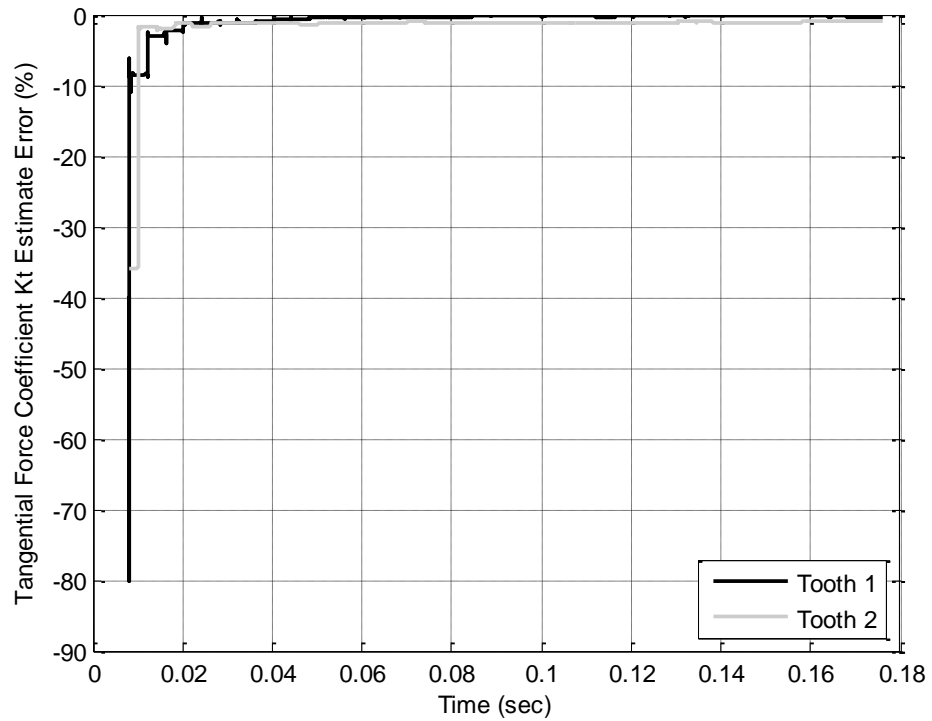


Figure 6.13. Tangential cutting coefficient estimates for each tooth separately when the EKF is given simulated tool deflection measurements along both the x - and y -axes.

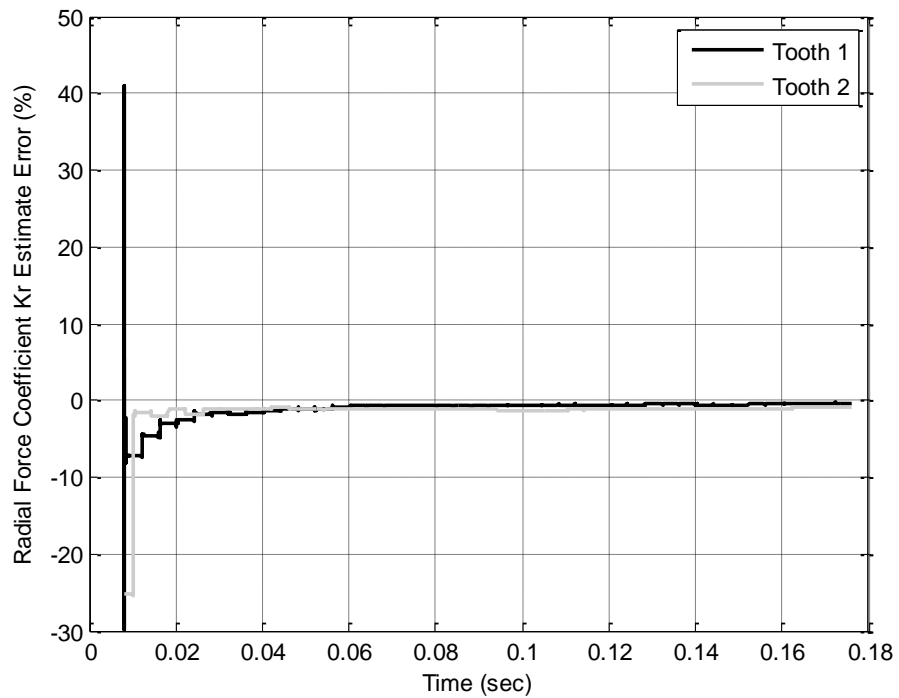


Figure 6.14. Radial cutting coefficient estimates for each tooth separately when the EKF is given simulated tool deflection measurements along both the x - and y -axes.

The EKF was also tested on the same experimental data given to the EKFs in Section 6.1, with the same preparation as before (so without any re-sampling). The noise covariance matrices were selected as in Eqs. (6.4) and (6.5), and the *a posteriori* covariance matrix of estimation error was initialized as in Eq. (6.7) when the EKF was estimating cutting force coefficients from simulated data. The state and parameter estimates were also initialized as for Figs. 6.13 and 6.14.

The cutting coefficient estimates produced by the EKF are displayed in Figs. 6.15 and 6.16, which show the tangential and radial coefficient estimates, respectively. The coefficients are again represented in terms of percent error from the values identified in Section 5.1, and the data sample was again cropped by two revolutions at the beginning and end during data processing. The same type of stepwise behavior as in Figs. 6.13 and 6.14 is evident in these figures, though more pronounced due to the longer settling time and more severe variation in estimates.

The convergence of EKF estimates in Figs. 6.15 and 6.16 does not necessarily reflect upon the accuracy of these estimates with respect to the actual cutting coefficients because the percent error in these figures is in reference to cutting coefficient values found previously (in Section 5.1) by running the EKF on experimental data with a nearly identical procedure. Hence, the final values are within 0.01 percent of their identified values, and the reason for any error to exist is likely that there were slight differences in manually selecting the cut end point from experimental data for analysis on separate occasions. It is reasonable that the EKF would take longer to settle in Figs. 6.15 and 6.16 given the more unpredictable noise of experimental measurements than when given the artificial Gaussian noise of the simulated measurements for Figs. 6.13 and 6.14.

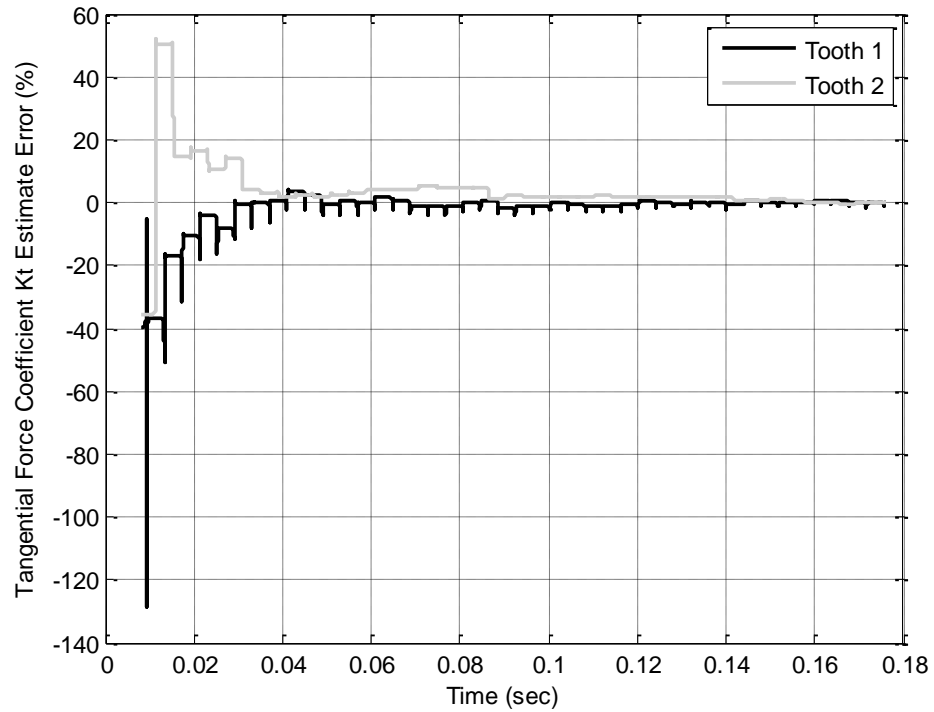


Figure 6.15. Tangential cutting coefficient estimates for each tooth separately when the EKF is given experimental tool deflection measurements along both the x - and y -axes.

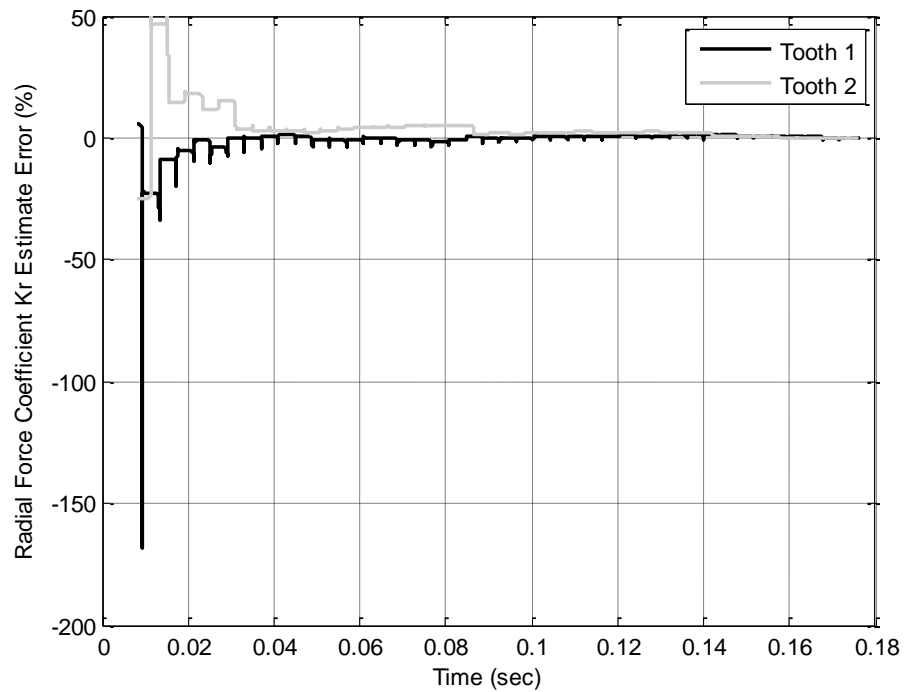


Figure 6.16. Radial cutting coefficient estimates for each tooth separately when the EKF is given experimental tool deflection measurements along both the x - and y -axes.

If only one set of cutting force coefficients is estimated for both teeth, the resulting estimates lie very close to the smaller of the two pairs of cutting force coefficients found for each tooth separately. The initial coefficient estimates were set equal to the means of the corresponding initial estimates of the two teeth used in Figs. 6.13-6.16. Figure 6.17 illustrates the behavior of the estimates for K_t and K_r , which converge with slowly-damped oscillations to mean values near $4.84 \times 10^8 \text{ N/m}^2$ and $3.65 \times 10^8 \text{ N/m}^2$, respectively, which are significantly different from the dynamometer values of $K_t = 5.89 \times 10^8 \text{ N/m}^2$ and $K_r = 3.19 \times 10^8 \text{ N/m}^2$. Also compare the final estimates to the values of cutting force coefficients found by the EKF in Section 5.1: $K_{t1} = 2.48 \times 10^8 \text{ N/m}^2$, $K_{t2} = 6.64 \times 10^9 \text{ N/m}^2$, $K_{r1} = 2.20 \times 10^8 \text{ N/m}^2$, and $K_{r2} = 4.15 \times 10^9 \text{ N/m}^2$. The final values of K_t and K_r are much closer to the values estimated for the first tooth than they are to those for the second.

The force coefficient estimates favoring the first tooth might be explained by the first tooth spending more time engaged in the workpiece than the second tooth. The second tooth often engaged the workpiece late in its pass because the tool was out of contact with the workpiece during the first part of its pass. This behavior is illustrated in Fig. 6.18 by negative chip thicknesses, which indicate the second tooth was not engaged in the workpiece at a time when it was expected to be cutting (i.e., $\theta_{entry} \leq \theta_p(t) \leq \theta_{exit}$ as in Section 2.2). The first tooth may, therefore, have had a greater influence on the cutting force coefficient estimates. Note that these chip thicknesses are calculated directly from the simulated data using the chip thickness model in Section 2.2 and do not reflect the state estimates of the EKF.

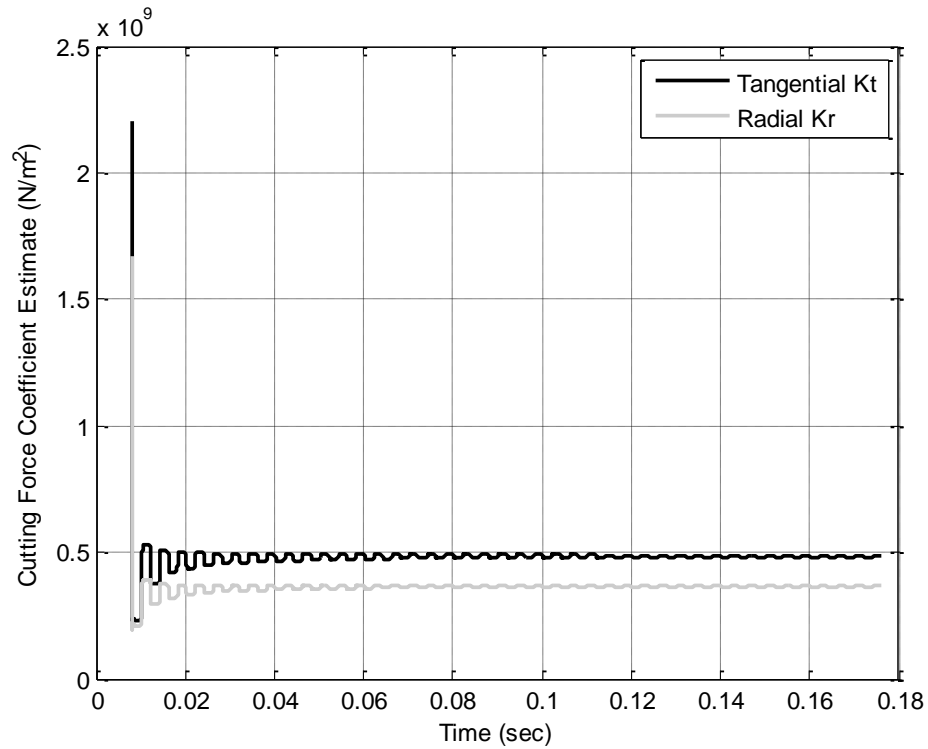


Figure 6.17. Tangential and radial cutting force coefficient estimates for both teeth together when the EKF is given simulated tool deflection measurements along both the x - and y -axes.

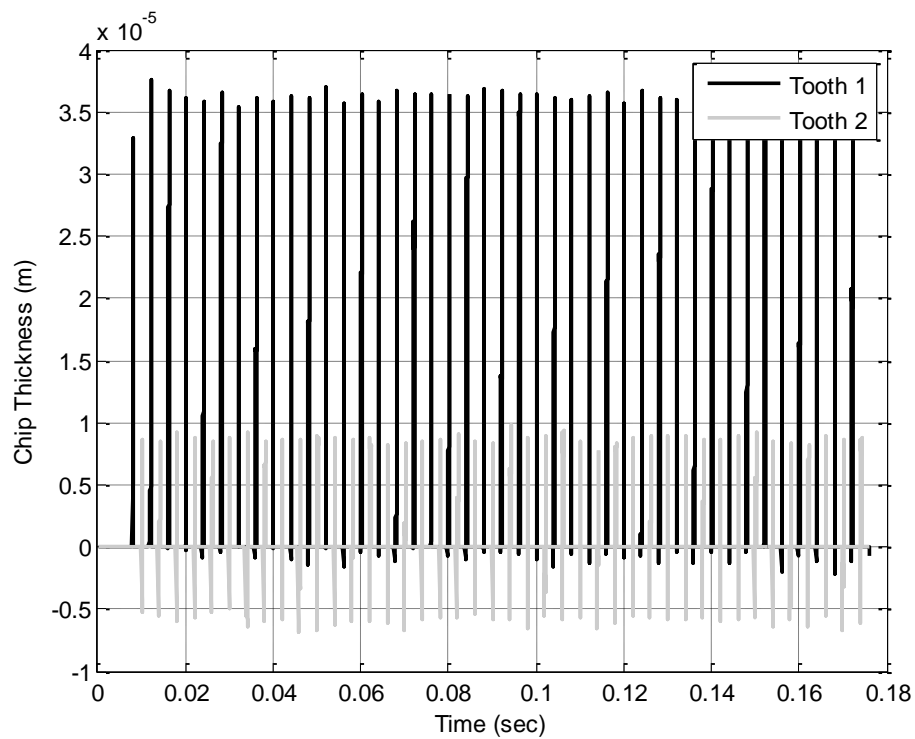


Figure 6.18. Chip thicknesses calculated during EKF iterations from simulated tool deflection measurements along both the x - and y -axes.

The estimates in Fig. 6.17 still exhibit the stepwise behavior mentioned previously, which is due to the cutting force coefficients being observable only when a tooth is engaged in the workpiece. The magnitude of these steps decreases significantly as the EKF settles on a steady-state estimate, though the estimates continue to display the behavior throughout the test.

To illustrate the repeatability of the EKF in producing the same final cutting coefficient estimates given a wide range of initial estimates, the EKF was run ten times consecutively with initial cutting force coefficients that were randomized between -50 and +50 percent of the values identified in Section 5.1. The cutting coefficients for each tooth were estimated separately. Figures 6.19 and 6.20 illustrate the repeatability of the tangential and radial estimates, respectively, displaying very similar behavior on each trial. It is interesting that the estimates for the first tooth typically dropped very low (some even went negative briefly) before recovering to more accurate values. Though the reason for these highly inaccurate values is unclear, the ability to recover from such values is a desirable feature of the EKF. The EKF has been found to recover from even more inaccurate initial estimates, such as -250 or +250 percent error, still ending with estimates within 6 percent or so of the identified values (e.g., consider the high error, sometimes over 1000 percent, of the randomized initial estimates used in Section 5.3 with respect to the final EKF estimates).

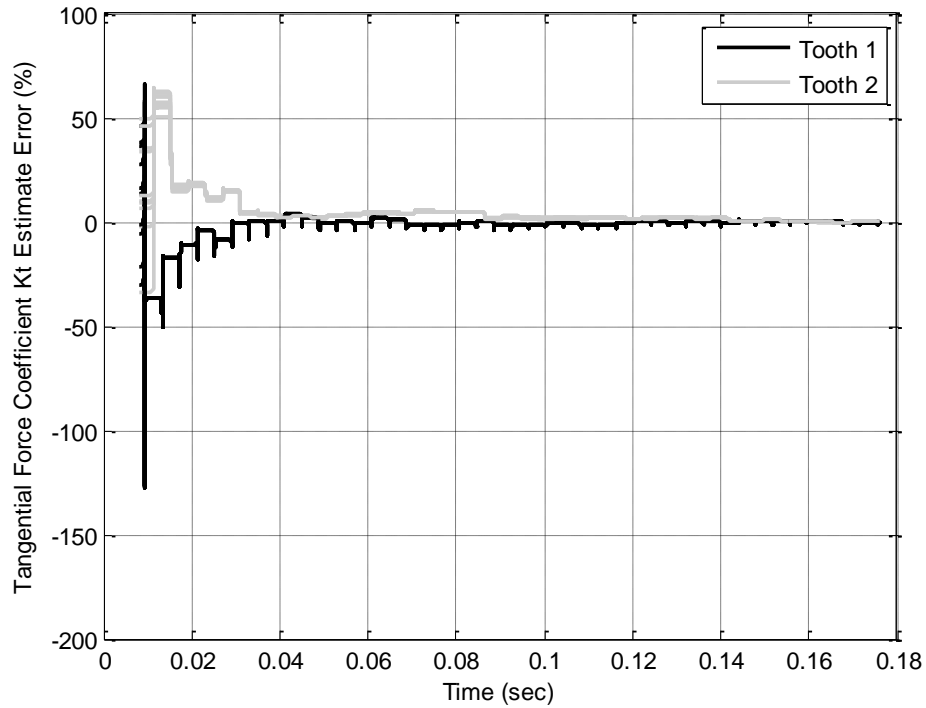


Figure 6.19. Tangential cutting coefficient estimates for each tooth separately on ten consecutive trials based on experimental measurements along both the x - and y -axes.

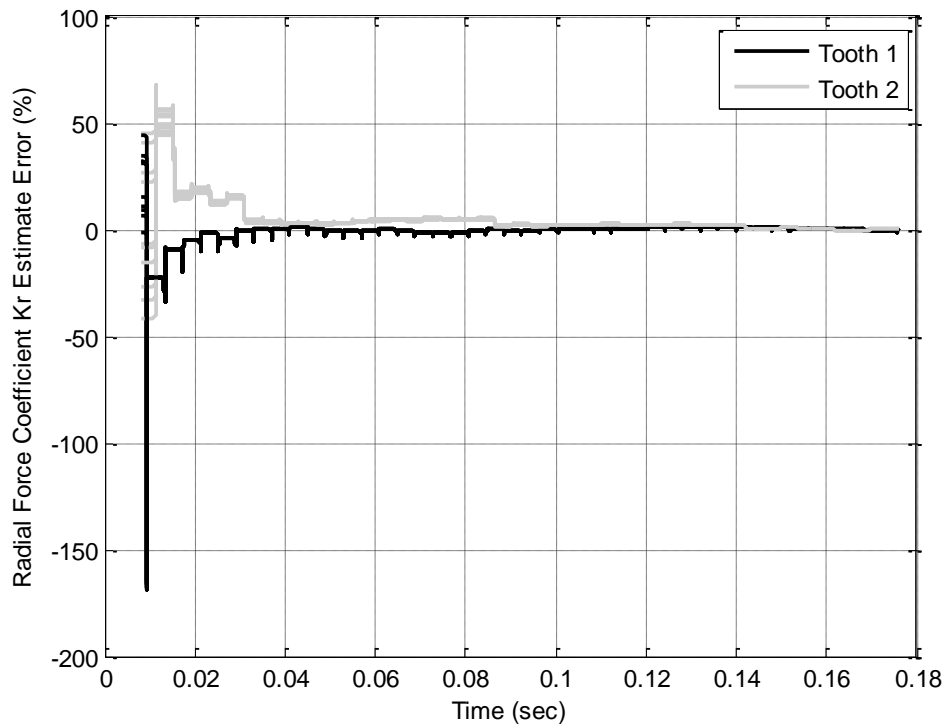


Figure 6.20. Radial cutting coefficient estimates for each tooth separately on ten consecutive trials based on experimental measurements along both the x - and y -axes.

For the reasons discussed in Section 5.1, the actual modal parameters and cutting force coefficients of the tool-workpiece system are unknown at a spindle speed of 15,000 rpm, since high-speed milling conditions are very different from the conditions under which the hammer test for modal parameters and the dynamometer tests for cutting force coefficients were conducted. It is difficult, therefore, to determine whether the EKF can accurately estimate these parameters. When using the EKF estimates of cutting force coefficients from experimental data (as in Section 5.1) to run a simulation, the simulated tool trajectory is very similar to the experimental tool trajectory. This similarity seems to indicate that the EKF can produce useful estimates of the cutting force coefficients. A more thorough test, however, would use these estimates to conduct an analysis of the chatter stability of the tool-workpiece system (e.g., with TFEA) and compare the resulting chatter stability boundaries with experimentally determined bifurcation points over a wide range of cutting conditions. Though the accuracy of the EKF estimates may be difficult to show, the repeatability of the estimates is demonstrated by their convergence to nearly the same final values of cutting force coefficients on multiple trials, despite being given highly varying initial values, as in Figs. 6.19 and 6.20.

The apparent accuracy and repeatability of the EKF as displayed in this study warrant further investigation. The EKF should be tested more thoroughly to determine if it can adapt to new tool-workpiece combinations and cutting conditions, how well it can accommodate tooth asymmetry or measurement noise, and how useful its parameter estimates are for chatter stability analysis.

CHAPTER 7: CENTRIFUGAL AND CORIOLIS FORCES

7.1. Modification of the Dynamic Model

In an attempt to explain the differences observed between the simulated and experimental tool deflection measurements (see, for example, Section 5.1), it was proposed that inertial forces that had not been included in the dynamic model might have a greater effect on experimental data than was previously considered. In particular, due to the high rotational velocity of the tool, any deflection of the tool from center could result in a significant centrifugal or Coriolis inertial force, given that the center of mass of the tool has shifted away from the origin and is now being rotated around the origin at high velocity. Initial calculations showed that the magnitudes of these inertial forces were very significant in proportion to typical cutting forces, so it was deemed worthwhile to consider them in the dynamic model.

By treating the accelerations as inertial forces per d'Alembert's principle, the centrifugal and Coriolis forces are applied as in Fig. 7.1. Note that the cutting forces F_x and F_y act in the positive x - and y -directions, respectively, as defined in Section 2.1 and Fig. 2.1. The restoring forces of tool stiffness ($k_x x$ and $k_y y$) and the resisting forces of tool damping ($c_x \dot{x}$ and $c_y \dot{y}$) act in the negative directions along these axes, while the inertial forces that substitute tool accelerations along these axes ($m_x \ddot{x}$ and $m_y \ddot{y}$) also act in the negative direction, opposite their corresponding accelerations. The centrifugal force F_{cen} acts along the positive radial direction, opposite the direction of the centripetal acceleration it substitutes. If the radial velocity of the tool is positive, the Coriolis

acceleration points in the direction of tangential velocity, so the Coriolis inertial force F_{Cor} points opposite the direction of tangential velocity.

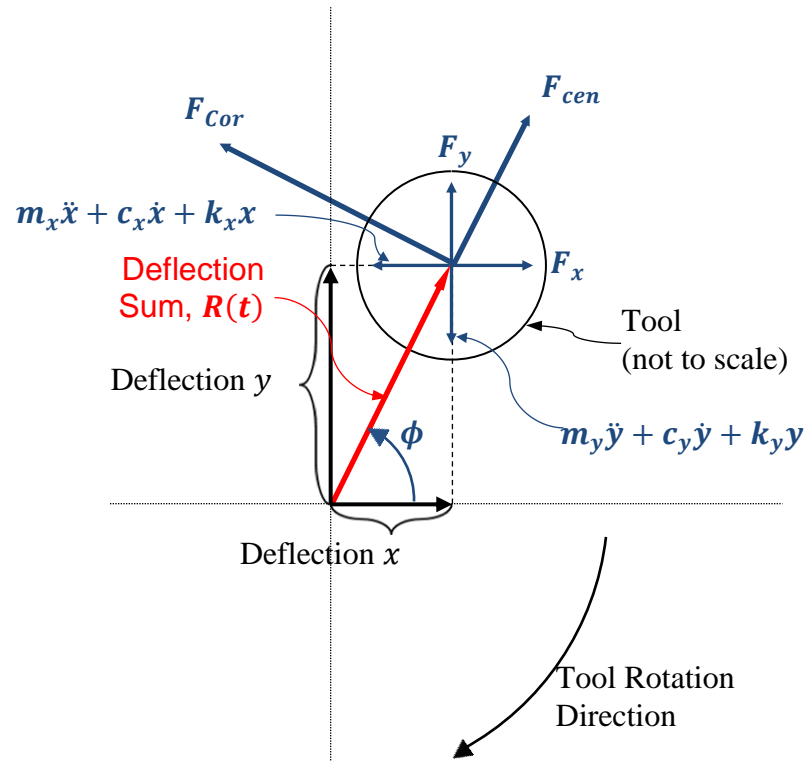


Figure 7.1. Diagram of applied and inertial forces, including centrifugal and Coriolis forces.

The magnitude of centrifugal force is defined as

$$F_{cen}(t) = mR(t)\omega_{\pi}^2, \quad (7.1)$$

where m is the modal mass of the tool (kg), assuming $m = m_x = m_y$ for simplicity, and ω_{π} is the spindle speed in rad/s. The radius $R(t)$ represents the distance (m) from the

tool center to the center of rotation. Note that when runout is present, the center of rotation is not the same as the undeflected position of the tool. Deflection measurements by the capacitive sensors are intended to represent deflection from the center of rotation, since the x - y origin is found by averaging several revolutions of measurements without cutting. The radius $R(t)$ is found as

$$R(t) = \sqrt{x(t)^2 + y(t)^2}. \quad (7.2)$$

The magnitude of Coriolis force is defined as

$$F_{Cor} = 2\dot{R}(t)\omega_{\pi}, \quad (7.3)$$

where $\dot{R}(t)$ is the radial velocity (m/s) of the tool deflection vector (i.e., velocity in the radial direction with respect to the center of rotation), where $\dot{R}(t) > 0$ indicates an increasing radial distance. This velocity is found by differentiating Eq. (7.2) with respect to time, and the result is

$$\dot{R}(t) = \frac{x(t)\dot{x}(t) + y(t)\dot{y}(t)}{\sqrt{x(t)^2 + y(t)^2}}, \quad (7.4)$$

where $\dot{x}(t)$ and $\dot{y}(t)$ represent the velocities (m/s) of the tool along the x - and y -axes, respectively. Note that $\dot{R}(t)$ and, therefore, the Coriolis force are functions of both tool deflection and tool velocity. The numerator of Eq. (7.4) could also be rewritten as the dot

product of the tool deflection vector with the tool velocity vector, where the denominator represents the length of the deflection vector.

Summing the forces in Fig. 7.1 and reorganizing the equations to resemble the original dynamic model (Eqs. (2.5)-(2.6)) results in

$$m_x \ddot{x}(t) + c_x \dot{x}(t) + k_x x(t) = F_x(t) + F_{cen}(t) \cos \phi(t) - F_{Cor} \sin \phi(t) \quad (7.5)$$

and

$$m_y \ddot{y}(t) + c_y \dot{y}(t) + k_y y(t) = F_y(t) + F_{cen}(t) \sin \phi(t) + F_{Cor} \cos \phi(t), \quad (7.6)$$

where $\phi(t)$ is the angle (rad) from the positive x -axis to the tool deflection vector. This angle is found from $x(t)$ and $y(t)$ as

$$\phi(t) = \begin{cases} \tan^{-1} \left(\frac{y(t)}{x(t)} \right), & \text{for } x(t) \geq 0 \\ \pi + \tan^{-1} \left(\frac{y(t)}{x(t)} \right), & \text{for } x(t) < 0 \end{cases} \quad (7.7)$$

and depends on the quadrant in which the tool deflection vector lies.

Moreover, as mentioned previously, it has been hypothesized that the undeflected centerline of the tool may not coincide with the axis of rotation, in which case the spring part of the model must be modified to reflect a new reference point that does not coincide

with the origin. When this assumption is made, the equations of motion in Eqs. (7.5) and (7.6) become

$$\begin{aligned} m_x \ddot{x}(t) + c_x \dot{x}(t) + k_x(x(t) - r_0 \sin(\theta - \theta_0)) \\ = F_x(t) + F_{cen}(t) \cos \phi(t) - F_{Cor} \sin \phi(t) \end{aligned} \quad (7.8)$$

and

$$\begin{aligned} m_y \ddot{y}(t) + c_y \dot{y}(t) + k_y(y(t) - r_0 \cos(\theta - \theta_0)) \\ = F_y(t) + F_{cen}(t) \sin \phi(t) + F_{Cor} \cos \phi(t), \end{aligned} \quad (7.9)$$

where r_0 is the eccentricity (m) of the undeflected centerline with respect to the centerline of rotation, and θ_0 is the angle of the eccentricity vector, defined clockwise from the y-axis.

7.2. Simulation Results

Preliminary simulations have been conducted with the inclusion of centrifugal and Coriolis forces (as in Eqs. (7.5) and (7.6)), but no definitive matches with experimental data have yet been found. Interesting bifurcation phenomena have, nevertheless, been observed. For instance, conducting a simulation with the inertial force model and using the system parameters estimated for the first incline trial (see Table 5.2) resulted in the once-per-revolution tool deflection data shown in Fig. 7.2. After some apparent bifurcation and reconvergence, two branches appear, with each branch then disintegrating into a cloud at a greater depth of cut. This form of bifurcation appears somewhat

different from the bifurcations observed in Sections 5.2 and 5.3, in which separate branches would cross over one another and eventually form a common cloud. The bifurcation followed by reconvergence and a second bifurcation also seems different from previous observations.

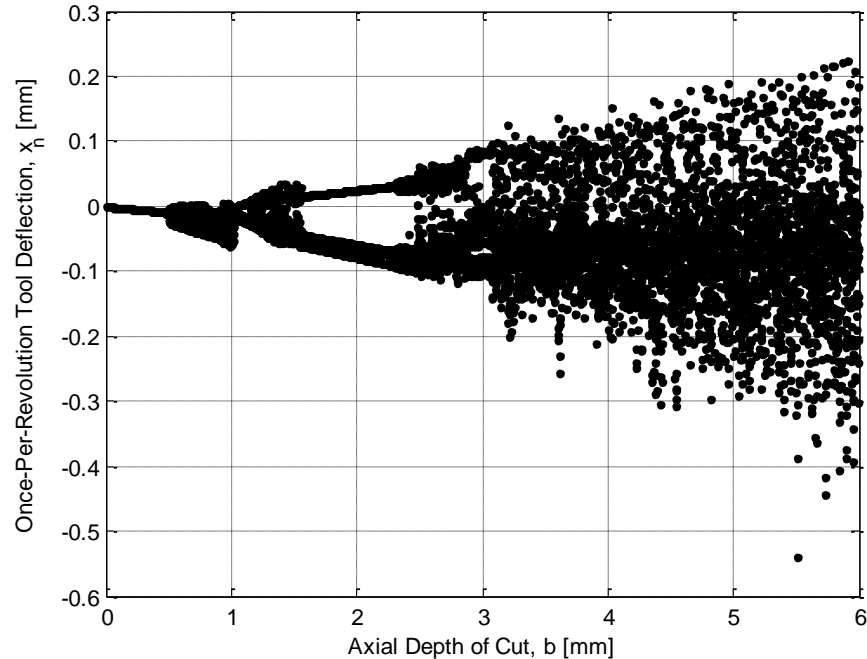


Figure 7.2. Once-per-revolution tool deflection results of simulation with centrifugal and Coriolis forces with system parameters from Table 5.2 for incline trial #1.

The cutting and inertial forces are displayed from this simulation over one revolution at 0.4 mm depth of cut (before any bifurcation occurs) in Fig. 7.3. The corresponding tool deflections for this revolution, from which the inertial forces were calculated, as well as the corresponding chip thicknesses, are displayed in Fig. 7.4. From Fig. 7.3 it is apparent that the inertial forces, especially the Coriolis force, have significant magnitudes compared to those of the cutting forces. Moreover, the inertial forces act throughout almost the entire revolution, whereas the cutting forces act only briefly in low-radial-immersion milling. By comparing Fig. 7.3 with Fig. 7.4, it can also

be observed that the Coriolis force is greatest when there is a moderate tool deflection and velocity, as should be expected from Eqs. (7.3) and (7.4), and is least when either deflection or velocity falls near zero.

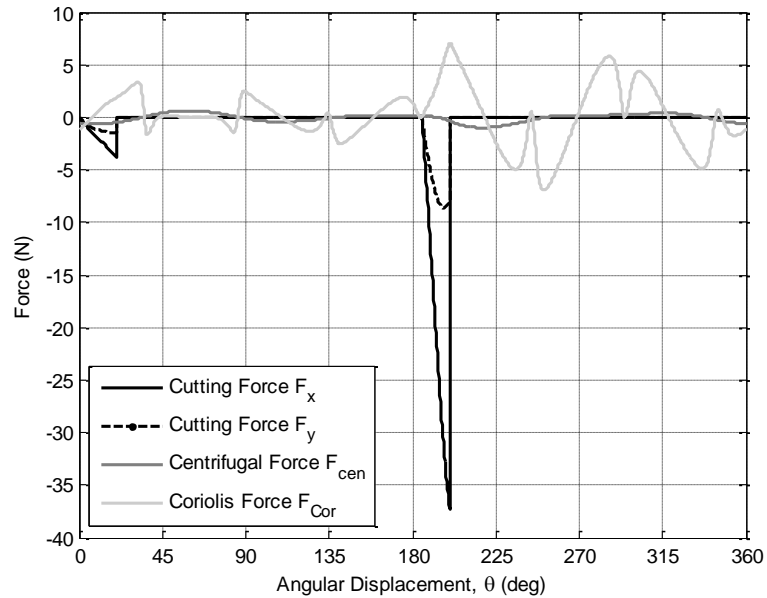


Figure 7.3. Cutting and inertial forces of simulation over single revolution at axial depth of cut of 0.4 mm with system parameters from Table 5.2 for incline trial #1.

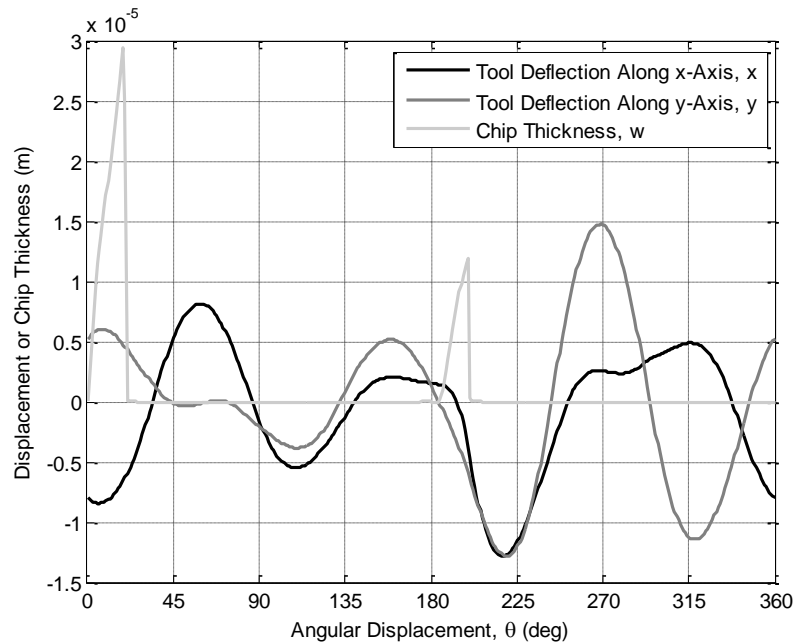


Figure 7.4. Tool deflection and chip thickness of simulation over single revolution at axial depth of cut of 0.4 mm with system parameters from Table 5.2 for incline trial #1.

Note that the simulations conducted in this section require an initial tool deflection along both axes because otherwise the Coriolis force is undefined (see Eqs. (7.3) and (7.4)). Therefore, the initial deflections along each axis are set equal to 1×10^{-8} m, which is nearly zero in this setting.

By including the eccentricity (used in Eqs. (7.8) and (7.9)) in the model and setting it to $r_0 = 1 \times 10^{-5}$ m and $\theta_0 = 5.17$ rad (values loosely based on observations of raw deflection data before subtracting the tool contour), the once-per-revolution tool displacement plot is changed to that of Fig. 7.5 from Fig. 7.2. In Fig. 7.5 the initial chatter-free points have been shifted in the negative x -direction. The figure exhibits a similar sort of bifurcation followed by reconvergence as in Fig. 7.2, except that the branches remain smooth longer and the large cloud emerges from one rough branch, rather than two distinct branches (as in Fig. 7.2). The cloud in Fig. 7.5 also does not appear until a much later depth of cut than in Fig. 7.2 (closer to the experimental value of 3.8 mm for this trial). Both figures seem to display period-doubling (or flip) bifurcations (characterized by two distinct branches emerging from one branch).

Both Figs. 7.2 and 7.5 exhibit non-uniform cloud densities once chatter is clearly present. Figure 7.2 exhibits greater density along the lower branch than the upper, and Fig. 7.5 exhibits greater density along the center of the cloud (coincident with the original branch), with relatively few points outside this region. The reasons for these non-uniform distributions remain unknown, but possible explanations include severe tooth asymmetry and, in Fig. 7.5, the eccentricity of the tool. It is also possible that these non-uniformities are caused by the added inertial forces, as they do not seem typical of previous simulations that omitted these forces.

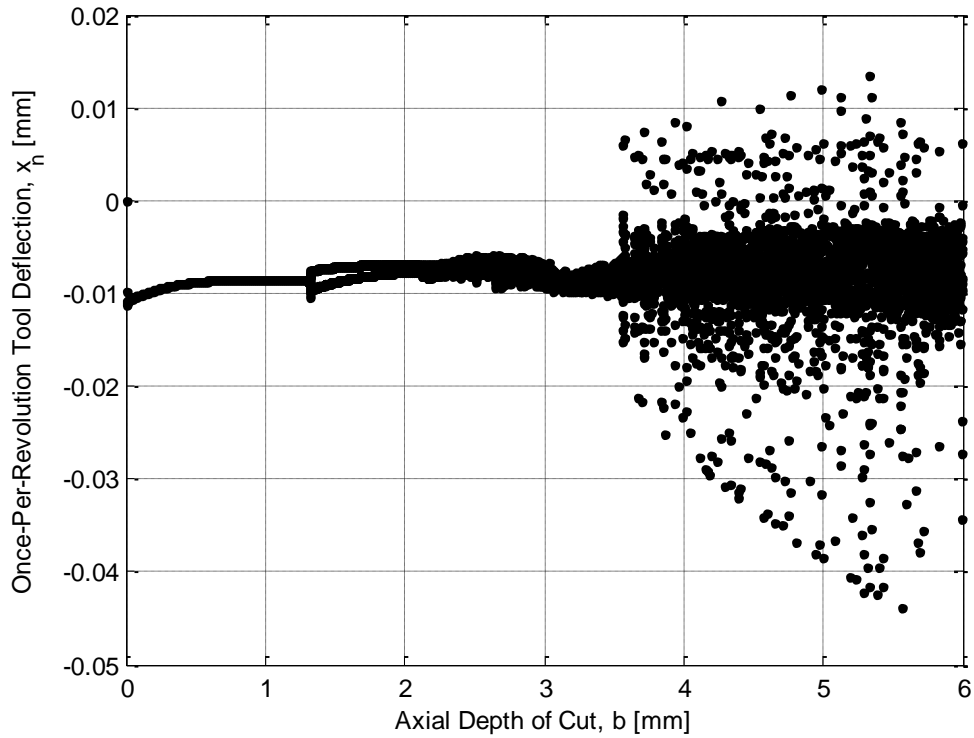


Figure 7.5. Once-per-revolution tool displacement results of simulation including inertial forces with eccentricity of $r_0 = 1 \times 10^{-5}$ m at $\theta_0 = 5.17$ rad, with incline trial #1 parameters.

The corresponding forces and tool displacements at 0.4 mm depth of cut are displayed in Figs. 7.6 and 7.7, respectively. Note that in these plots x and y represent the displacement of the tool tip from the center of rotation, rather than deflection away from the undeflected state (which actually rotates at radius $r_0 = 1 \times 10^{-5}$ m). For clarity, x and y in these plots are called tool displacements. These plots look similar to those in Figs. 7.3 and 7.4, but the displacements in Fig. 7.7 exhibit a greater tendency to stay on one side or the other of the undeflected position than those in Fig. 7.4. That is, there are fewer sign changes in the displacement: four per revolution along the x -axis instead of six, and two per revolution along the y -axis instead of eight. This trend seems to indicate that the mean tool trajectory oscillates at a much lower frequency (such as once per revolution due to eccentricity in the spring force) than the higher-frequency vibrations due to cutting

and inertial forces. Because the displacements along both axes are simultaneously large for more of the revolution in Fig. 7.7 than in Fig. 7.4, the resulting radial displacement $R(t)$ is also larger, causing the centrifugal force in the eccentricity simulation to be somewhat greater than when no eccentricity is included.

Figures 7.8 and 7.9 illustrate the tool trajectories of the non-eccentric and eccentric simulations (both including inertial forces) for every revolution from 0 mm to 0.4 mm axial depth of cut. The thick black line represents the mean trajectory for each simulation. From these figures it is evident that the mean trajectory has changed significantly because of eccentricity. Without eccentricity the mean trajectory oscillates only at high frequencies about the rotational axis, but with eccentricity, the mean trajectory has an additional low-frequency (once-per-revolution) oscillation, from which the higher-frequency oscillations deviate. Note that at this low depth of cut, an eccentricity as small as 1×10^{-5} m dwarfs the vibrations caused by inertial and cutting forces.

For comparison, Fig. 7.10 shows a sample of experimental deflection measurements along the x -axis from the first incline trial before the tool contour is subtracted from the data. Raw voltage measurements were converted to displacement measurements, and the mean displacement was subtracted from the data to center vibrations about zero. This 1-second sample of data was taken before cutting began and was used to find the average tool contour to subtract from the data (see Section 3.1 for a description of this process). The tool contour in Fig. 7.10 is very similar to the mean tool trajectory in Fig. 7.9, indicating that the inclusion of eccentricity in the model may allow the model to replicate the experimental behavior of the tool without subtracting the tool

contour. Preliminary attempts to reconcile the simulation with experimental tool trajectories have not been successful, but this approach warrants further investigation.

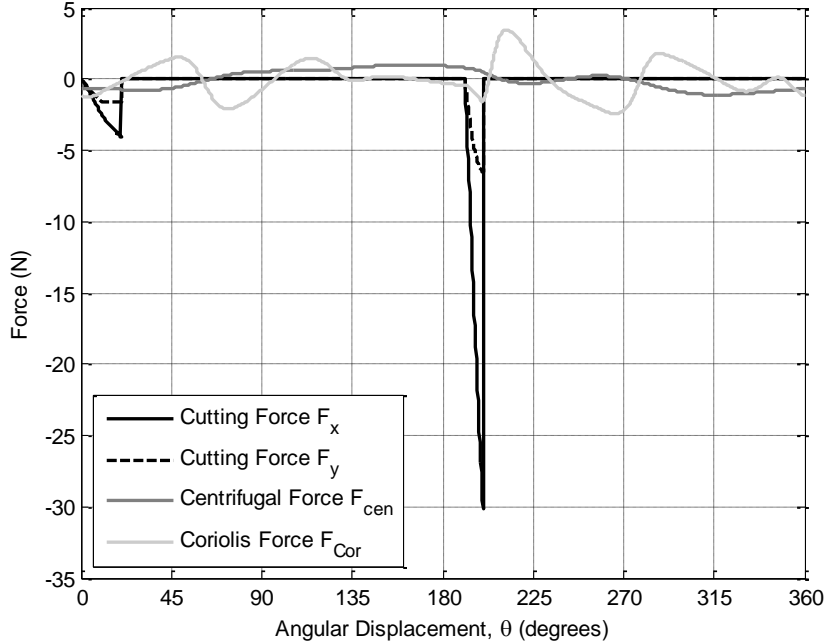


Figure 7.6. Cutting and inertial forces of simulation over one revolution at axial depth 0.4 mm with eccentricity $r_0 = 1 \times 10^{-5}$ m, $\theta_0 = 5.17$ rad, with incline trial #1 parameters.

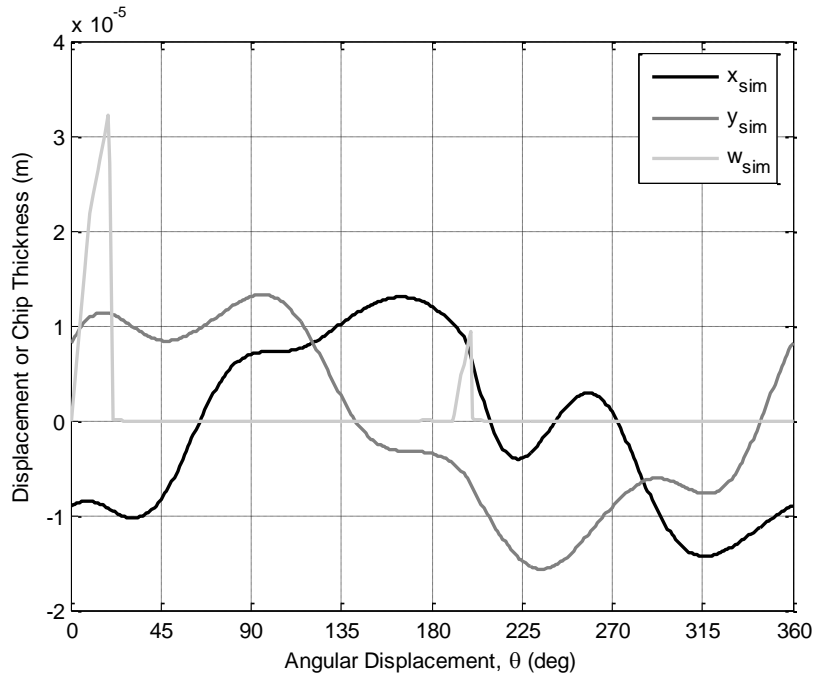


Figure 7.7. Tool displacement and chip thickness of simulation over one revolution at 0.4 mm depth with eccentricity $r_0 = 1 \times 10^{-5}$ m, $\theta_0 = 5.17$ rad, and incline trial #1 parameters.

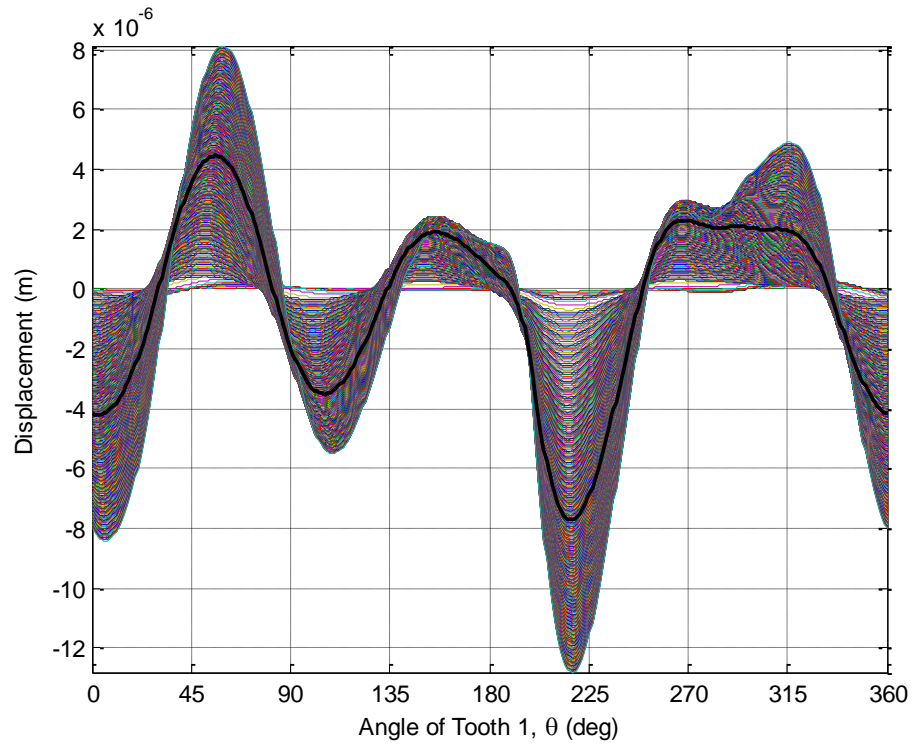


Figure 7.8. Tool displacement of simulation over every revolution from 0 to 0.4 mm depth without eccentricity, with inertial forces and incline trial #1 parameters.

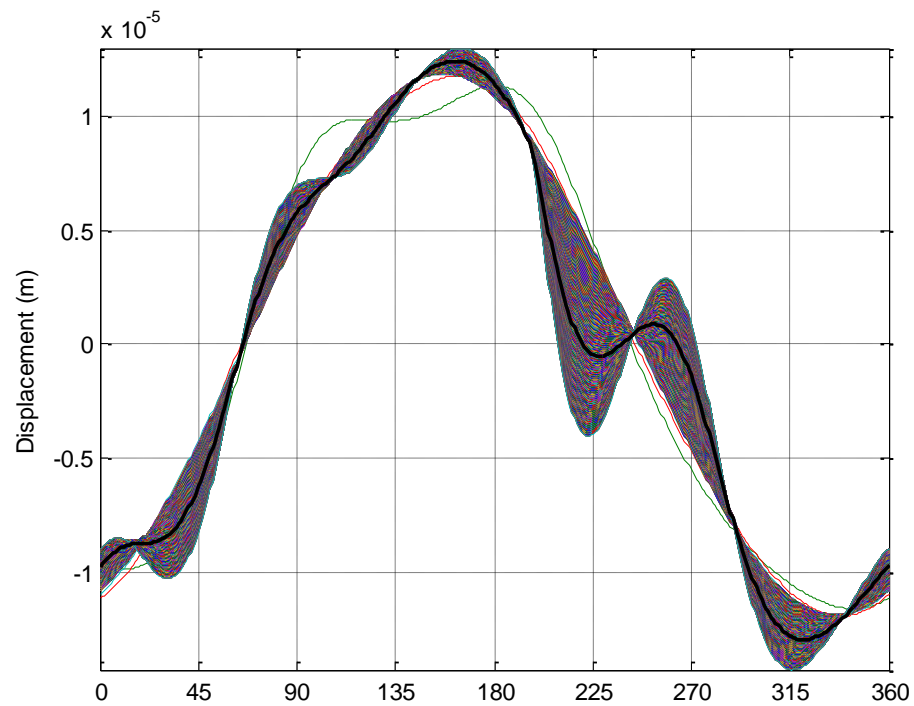


Figure 7.9. Tool displacement of simulation over every revolution from 0 to 0.4 mm depth with eccentricity $r_0 = 1 \times 10^{-5}$ m, $\theta_0 = 5.17$ rad, inertial forces, and incline #1 parameters.

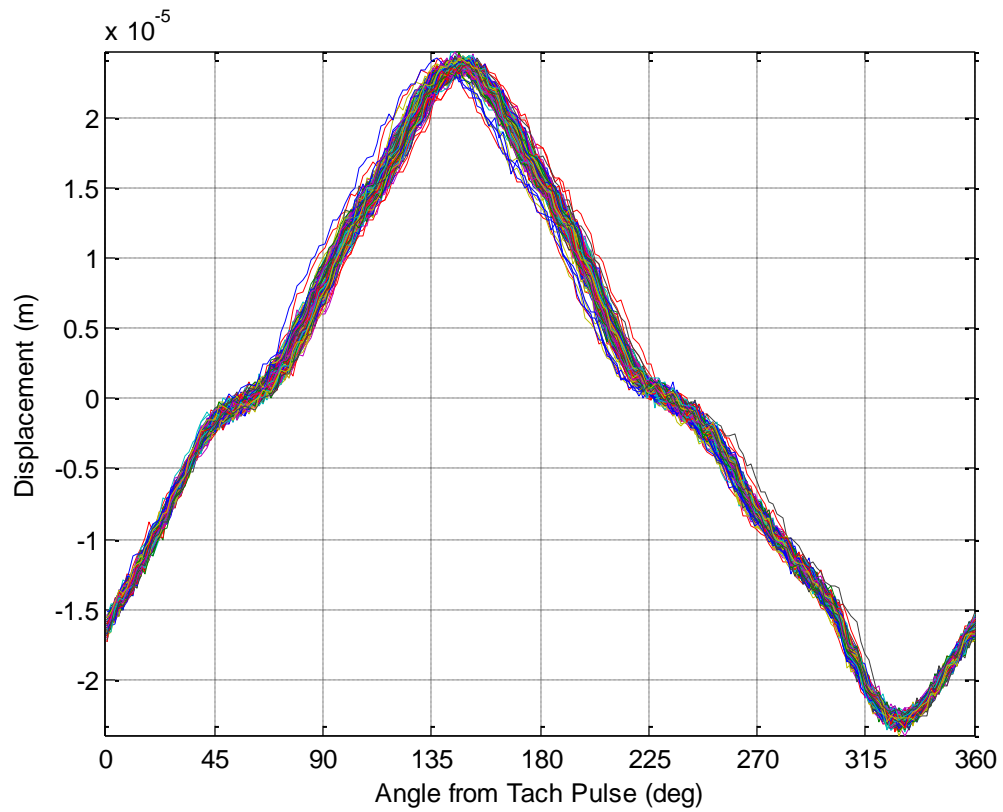


Figure 7.10. Raw tool displacement (no tool contour subtracted) of experiment over every revolution for 1 sec of data without cutting in incline trial #1.

CHAPTER 8: CONCLUSION

8.1. Summary of Findings

A variety of Kalman filters were considered for use in estimating parameters of the tool-workpiece dynamic system that are relevant to calculating chatter stability boundaries in high-speed low-radial-immersion milling processes. In particular, implementations of an EKF were proposed as possible improvements over the current state of research. Special attention was given to ensuring that the system was observable, which should guarantee convergence of the parameter estimates and improve robustness of the system in characterizing tool-workpiece dynamics for a wide variety of milling scenarios. To ensure observability while estimating two parameters (two modal parameters, two cutting force coefficients, or one of each) required including tool deflection measurements along the y -axis in the filter.

Two novel EKF structures were developed that could estimate system parameters with observability. One structure estimated two modal parameters from tool deflection measurements along both the x - and y -axes, and one estimated two cutting force coefficients from the same data. Both structures were tested on simulated and experimental data, and final estimates showed good convergence given a wide variety of initial estimates, which indicated good repeatability of the EKF. Accuracy of the estimates is difficult to determine, but numerical simulations based on the EKF parameter estimates correlated well with experimental measurements for a single-revolution tooth trajectory plot at similar axial depths of cut. These parameter estimates were found by implementing two EKFs in parallel to estimate separate cutting force coefficients for each

cutting tooth, which allowed the cutting force coefficients to reflect the tooth asymmetry evident in the experiment. Though the EKF estimates produced simulations that correlated well with the experiment over one revolution, the predicted bifurcation points in the simulations did not correlate as well with experimental observations. Modifications to the model, such as those in Chapter 7 and those proposed in Section 8.2, may improve the correlation of the simulated and experimental bifurcation points. It remains to be seen which pair of parameters provides the best characterization of the tool-workpiece system and how useful the EKF parameter estimates are for stability analysis (e.g., with TFEA).

A computational improvement was made to the numerical chip thickness model, significantly increasing its computational speed, and cutting force coefficients for the tools used in this research were found experimentally, eliminating the need to depend on values found in literature. Simulations of the milling process were conducted using both a traditional and a numerical chip thickness model, and the results were compared to experimental measurements of a similar process. The models correlated well with each other, though plots of simulated tooth paths from both models show that the traditional model repeatedly underestimates the chip thickness (as defined by the distance between one tooth path and another), while the numerical model calculates this value more accurately.

The inclusion of centrifugal and Coriolis inertial forces in the tool dynamic model was proposed, as well as a modification to the model that accounts for eccentricity between the tool center of mass and the center of rotation. Preliminary simulations were conducted with the modified model, but no system parameters were identified that would

allow the simulations to correlate well with experimental data. Nevertheless, the magnitudes of the inertial forces in the simulation were found to be very significant compared to the cutting forces, so it seems that the inclusion of these forces in the model could improve correlation of the simulation with experiment once the appropriate system parameters are found.

The inclusion of these inertial forces in simulations produced intriguing bifurcation behavior different from simulations conducted without the forces. Furthermore, the inclusion of eccentricity produced a mean tooth trajectory that was similar in shape to raw experimental tool deflection measurements (from which the tool contour had not been subtracted), indicating that this modification to the model may allow the simulation to correlate well with raw deflection data if given the proper system parameters. In particular, this modification could allow eccentricity to be accounted for without using severely asymmetric cutting force coefficients. If this modification were included in EKF structure, the EKF force coefficient estimates could potentially correlate better with dynamometer values, and simulations conducted with the estimates could potentially predict bifurcation more accurately.

Note that the techniques used in this study are not limited to the sensors and parameters employed here. Using the same techniques described in this study, an observable EKF structure could be implemented with the same or different sensors to estimate the same or different parameters. Nevertheless, this study found that an EKF could estimate modal mass and stiffness accurately from tool deflection measurements made with capacitive sensors. The findings of this study show that these approaches hold promise for the development of a real-time chatter prediction and control system.

8.2. Areas for Future Research

The next steps for research in this field include continuing to test the EKFs proposed in this study on simulated tool deflection data to determine the accuracy of their parameter estimates with respect to known simulation parameters, evaluating the accuracy and computational cost of each approach. As the EKFs are tested on more simulated and experimental data, a better sense of the reliability and robustness of each filter may be gained. Continuing to test the EKFs on experimental tool deflection data and comparing the resulting parameter estimates to values found experimentally (through impulse-response tests for modal parameters and dynamometer force measurements for cutting force coefficients) may produce insight into the reasons for the differences between the estimated and experimental values. Again the accuracy and computational cost of each filter should be evaluated. Of particular interest is the continued simulation of milling processes with the system parameter estimates found from experimental tool deflection measurements, comparing the resulting simulations with the experimental data to evaluate how well the tooth trajectories over a single revolution correlate and how well the bifurcation behavior of the simulation mimics that of the experiment.

Alternative chip thickness models might be considered in the interest of improving accuracy or computational efficiency of the filter. Of great interest would be the discovery of a chip thickness model and corresponding parameters that accurately reproduce the dynamic behavior of a real tool-workpiece system while minimizing computational cost. Such a discovery might illuminate which parts of the model are most important in characterizing the tool-workpiece system. For example, if a simple impulse, executed over one time step, of appropriate magnitude to impart the energy of an entire

chip to the tool, were found to be a realistic chip force model, this discovery would indicate that it is not the shape of the forcing function but the energy that most affects the tool dynamics.

Considerable attention should also be given to the algorithm for stability boundary calculation. Choice of this algorithm plays an important role in both the accuracy and the feasibility for real-time implementation of a chatter avoidance system. A robust avoidance system should also include the location of the transition region between chatter and chatter-free zones. This transition region, which exhibits significant hysteresis, should be included in a chatter avoidance system, or at least a factor of safety should be used to avoid it. Such measures require further investigation of the width of this region in various milling scenarios.

A means of including asymmetric teeth in stability analysis (such as the Altintas/Budak or TFEA methods mentioned in Section 5.3) should be considered, whether by using separate radii or separate cutting force coefficients for each tooth. It is possible that an approach to this problem already exists, but it is not immediately clear how to implement asymmetric teeth in these analyses. These stability analysis methods are computationally much faster than numerically simulating tooth trajectories, as in this study, and could allow for the real-time prediction of chatter stability using asymmetric cutting force coefficient estimates, which could allow the chatter stability prediction to reflect tool runout and other asymmetries.

Even the approach used in this study to reflect tool asymmetries in the EKF structure might be revised. Instead of estimating cutting force coefficients separately for each tooth, perhaps the tooth radii could be estimated in some manner. Preliminary

numerical simulations that used severely asymmetric teeth radii seemed to encounter difficulties with diverging tool deflections, but it is possible that further investigation would reveal asymmetric radii to be a valid alternative approach to modeling tool asymmetry.

Further investigation should also be made of the sensitivity of the numerical simulations to initial cutting conditions. It was observed that different initial axial depths of cut could result in significantly different bifurcation points in simulations, but the extent of this sensitivity remains unknown. It would be particularly useful to determine whether simulations begun at a high depth of cut can be compared to simulations begun at a low depth of cut (with depth of cut increasing in both trials) because the memory limitations of modern computers can restrict the range of axial depths of cut over which a single simulation can be run.

As mentioned in Section 4.4, tool deflection estimates were not used in the calculation of chip thickness in the EKF structures in this study, so the feedback effect inherent in the milling process was omitted from the EKF structures. Future research could consider including delayed tool deflection states in the EKF structure to allow for chip thickness calculation from the estimated states. It is unclear how delayed states would affect EKF performance, but it is possible that this expansion of the EKF structure could improve the accuracy and reliability of parameter estimates.

Deeper investigation should be made into the reason behind the need for two different EKF time steps, one for simulated data (particularly for the first incline trial in Section 5.3) and one for experimental data. Perhaps a sample rate could be found that allows the EKF to perform well on both sets of data, or perhaps a more comprehensive

frequency domain analysis of the two sets of data (and various resamplings of them) would provide insight into the necessity for two sample rates.

Future research could consider using a UKF or alternative filter for system parameter estimation. As discussed in Section 4.1, EKFs are often less accurate and less computationally efficient than UKFs when applied to highly nonlinear systems [45-47], as they rely on linearized versions of the systems that may not be accurate for large time steps. Consequently, small time steps are required, and the Jacobian must be reevaluated on each time step, both of which increase computational time. Tuning EKFs to perform well can also be time-consuming and difficult. The UKF was introduced to solve these problems and requires no Jacobian or linearization, instead using the unscented transform to propagate state and measurement noise through the update processes to find their effect on state estimates, typically resulting in faster (i.e., fewer iterations, though not necessarily less computational time unless a sufficiently larger step size can be used) and more accurate convergence on parameter estimates. In the interest of developing a system that robustly and accurately estimates parameters relevant to chatter stability in real time, such improvements in accuracy and speed of convergence are highly desirable. Alternative filters, such as a second-order EKF or a divided-difference filter, might also provide improvements in accuracy or computational efficiency over the first-order EKF. Implementing an EKF or UKF that estimates alternative parameter pairs, such as one modal parameter and one cutting force coefficient, could also be attempted.

In the interest of improving accuracy and computational efficiency, the improvements to the numerical chip thickness model described in Section 2.3 might be considered. Restructuring the model to consider potential intersections of the cutting

tooth over a limited number of revolutions with the current workpiece surface, rather than with every point in the corresponding historical tooth trajectories, could reduce the computational cost for a typical simulation by several times. Methods have already been proposed in literature that might be implemented for this purpose, and reducing the computational cost of this chip thickness model may allow its seemingly more accurate physics to be simulated in a more convenient amount of time. Nevertheless, this model might still be more difficult to fully incorporate into an EKF than the simpler traditional chip thickness model employed in this study.

The effect of including centrifugal and Coriolis inertial forces in the dynamic model should be investigated further, as well as the effect of including eccentricity in the model. These modifications to the model, briefly described and tested in Chapter 7, may provide a means of accounting for runout and tool unbalance in the model. Furthermore, the significant magnitudes of the inertial forces calculated in Section 7.2 seem to indicate that these forces should be included in milling simulations. Future research should include searching for the appropriate system parameters to allow the simulation to correlate well with experimental data. These forces could potentially be incorporated into the EKF structure to allow the EKF to estimate modal parameters in light of these effects, or perhaps to estimate the eccentricity magnitude and angle instead of modal parameters or cutting force coefficients. The eccentricity might also be found by comparing simulations conducted without cutting forces to experimental tool deflection measurements of the rotating tool disengaged from the workpiece (before subtracting the tool contour from the data).

Various questions arise from simplifying the three-dimensional tool and spindle structure into a two-dimensional mass-spring-damper system. For example, it is possible that, due to model simplifications, the modal masses for the linear inertial forces along each axis are actually different from the masses involved in the centrifugal and Coriolis forces, or perhaps the modal mass varies from the x - to the y -axis. To answer these questions, modal parameters along both the x - and y -axes should be tested, and further comparison of inertial force simulations with experimental data should be made.

Related to the simplification of the three-dimensional structure into a two-dimensional model is the question of how to accurately identify experimental system parameters. As discussed in Section 5.1, modal parameters and cutting force coefficients are likely to vary with spindle speed. It becomes difficult, then, to identify the actual experimental values of these parameters because the tests used in this study to find them (e.g., hammer test and dynamometer force measurements) involve much lower spindle speeds than the spindle speeds used in high-speed milling. Future research could investigate the effect of spindle speed on these system parameters and perhaps explain why the values estimated by the EKF are so different from the values found by these tests. Hence, a better understanding of the accuracy of parameter estimates might be gained. Furthermore, it is possible that the modal parameters are different along each axis. Experimental testing of this might be conducted, and the effect of including such asymmetric parameters in the simulation could be investigated.

APPENDIX: RESULTS OF CUTTING FORCE EXPERIMENTS

Workpiece: 6061-T6511 Aluminum				
<i>Tool Description</i>	<i>Tangential Coefficients</i>		<i>Radial Coefficients</i>	
	K_{tc} (10^8 N/m ²)	K_{te} (10^3 N/m)	K_{rc} (10^8 N/m ²)	K_{re} (10^3 N/m)
0-deg Uncoated Short	7.90	9.39	5.38	15.1
30-deg Uncoated Short	6.61	9.74	3.17	7.62
30-deg Uncoated A	5.89	9.08	3.19	11.3
30-deg Uncoated B	5.77	7.92	3.32	11.0
30-deg Uncoated C	6.01	12.4	3.65	11.7
30-deg Coated A	5.45	10.4	3.24	14.7
30-deg Coated B	5.60	16.1	3.58	19.3
45-deg Uncoated A	5.66	10.8	3.05	16.0
45-deg Uncoated B	5.66	17.4	3.10	16.4
45-deg Coated A	5.53	15.2	2.93	15.9
45-deg Coated B	5.71	13.9	2.91	13.6

Workpiece: 7075-T651 Aluminum				
<i>Tool Description</i>	<i>Tangential Coefficients</i>		<i>Radial Coefficients</i>	
	K_{tc} (10^8 N/m ²)	K_{te} (10^3 N/m)	K_{rc} (10^8 N/m ²)	K_{re} (10^3 N/m)
0-deg Uncoated Short	6.87	13.3	4.01	20.8
30-deg Uncoated Short	5.71	13.4	2.15	15.7
30-deg Uncoated A	5.24	16.2	2.26	16.1
30-deg Uncoated B	5.51	13.5	2.19	17.1
30-deg Uncoated C	5.79	15.9	2.41	19.5
30-deg Coated A	5.54	14.0	2.91	18.3
30-deg Coated B	5.91	18.3	3.57	24.8
45-deg Uncoated A	5.64	17.5	2.80	18.3
45-deg Uncoated B	5.74	17.2	3.23	25.7
45-deg Coated A	5.67	19.0	2.91	25.2
45-deg Coated B	5.63	17.8	2.87	20.2

REFERENCES

1. Arnold, R. N., 1946, "Mechanism of Tool Vibration in Cutting of Steel," Proceedings of the Institution of Mechanical Engineers, **154**, pp. 261-276.
2. Andrew, C., and Tobias, S. A., 1961, "A Critical Comparison of Two Current Theories of Machine Tool Chatter," International Journal of Machine Tool Design Research, **1**, pp. 325-335.
3. Albrecht, P., 1965, "Dynamics of the Metal-Cutting Process," Journal of Engineering for Industry, **87**(4), pp. 429-441.
4. Tobias, S. A., 1959, "The Vibrations of Vertical Milling Machines under Test and Working Conditions," Proceedings of the Institution of Mechanical Engineers, **173**(1), pp. 474-510.
5. Merritt, H. E., 1965, "Theory of Self-Excited Machine-Tool Chatter," Journal of Engineering for Industry, **87**(4), pp. 447-454.
6. Tlustý, J., and Ismail, F., 1981, "Basic Non-Linearity in Machining Chatter," CIRP Annals, **30**(1), pp. 299-304.
7. Smith, S., and Tlustý, J., 1993, "Efficient Simulation Programs for Chatter in Milling," CIRP Annals, **42**(1), pp. 463-466.
8. Gurney, J. P., and Tobias, S. A., 1961, "A Graphical Method for the Determination of the Dynamic Stability of Machine Tools," International Journal of Machine Tool Design Research, **1**, pp. 148-156.
9. Sridhar, R., Hohn, R. E., and Long, G. W., 1968, "A Stability Algorithm for the General Milling Process," Transactions of the ASME Journal of Engineering for Industry, **90**(2), pp. 330-334.
10. Altintas, Y., and Budak, E., 1995, "Analytical Prediction of Stability Lobes in Milling," CIRP Annals, **44**(1), pp. 357-362.
11. Insperger, T., Mann, B. P., Stépán, G., and Bayly, P. V., 2003, "Stability of up-milling and down-milling, part 1: alternative analytical methods," International Journal of Machine Tools and Manufacture, **43**, pp. 25-34.
12. Balachandran, B., and Zhao, M. X., 2000, "A Mechanics Based Model for Study of Dynamics of Milling Operations," Meccanica, **35**, pp. 89-109.

13. Nayfeh, A. H., and Balachandran, B., 1995, *Applied Nonlinear Dynamics: Analytical, Computational, and Experimental Methods*, Wiley, New York.
14. Davies, M. A., Pratt, J. R., Dutterer, B., and Burns, T. J., 2002, "Stability Prediction for Low Radial Immersion Milling," *Journal of Manufacturing Science and Engineering*, **124**(2), p. 217.
15. Insperger, T., and Stépán, G., 2004, "Vibration Frequencies in High-Speed Milling Processes or a Positive Answer to Davies, Pratt, Dutterer and Burns," *Journal of Manufacturing Science and Engineering*, **126**(3), p. 481.
16. Szalai, R., Stepan, G., and Hogan, S. J., 2004, "Global dynamics of low immersion high-speed milling," *Chaos*, **14**(4), pp. 1069-1077.
17. Altintas, Y., 2000, *Manufacturing Automation: Metal Cutting Mechanics, Machine Tool Vibrations, and CNC Design*, Cambridge University Press, Cambridge, UK.
18. Mann, B. P., Insperger, T., Bayly, P. V., and Stépán, G., 2003, "Stability of up-milling and down-milling, part 2: experimental verification," *International Journal of Machine Tools and Manufacture*, **43**, pp. 35-40.
19. Mann, B. P., Bayly, P. V., Davies, M. A., and Halley, J. E., 2004, "Limit cycles, bifurcations, and accuracy of the milling process," *Journal of Sound and Vibration*, **277**(1-2), pp. 31-48.
20. Mann, B. P., Garg, N. K., Young, K. A., and Helvey, A. M., 2005, "Milling Bifurcations from Structural Asymmetry and Nonlinear Regeneration," *Nonlinear Dynamics*, **42**(4), pp. 319-337.
21. Cao, H., Li, B., and He, Z., 2012, "Chatter stability of milling with speed-varying dynamics of spindles," *International Journal of Machine Tools and Manufacture*, **52**(1), pp. 50-58.
22. Gagnol, V., Le, T.-P., and Ray, P., 2011, "Modal identification of spindle-tool unit in high-speed machining," *Mechanical Systems and Signal Processing*, **25**(7), pp. 2388-2398.
23. Zaghbani, I., and Songmene, V., 2009, "Estimation of machine-tool dynamic parameters during machining operation through operational modal analysis," *International Journal of Machine Tools and Manufacture*, **49**(12-13), pp. 947-957.
24. Albrecht, A., Park, S. S., Altintas, Y., and Pritschow, G., 2005, "High frequency bandwidth cutting force measurement in milling using capacitance displacement sensors," *International Journal of Machine Tools and Manufacture*, **45**(9), pp. 993-1008.

25. Dhupia, J., and Girsang, I., 2012, "Correlation-Based Estimation of Cutting Force Coefficients for Ball-End Milling," *Machining Science and Technology*, **16**(2), pp. 287-303.
26. Engin, S., and Altintas, Y., 2001, "Mechanics and dynamics of general milling cutters, Part I: helical end mills," *International Journal of Machine Tools and Manufacture*, **41**, pp. 2195-2212.
27. Fontaine, M., Devillez, A., Moufki, A., and Dudzinski, D., 2007, "Modelling of cutting forces in ball-end milling with tool–surface inclination, Part II: Influence of cutting conditions, run-out, ploughing and inclination angle," *Journal of Materials Processing Technology*, **189**(1-3), pp. 85-96.
28. Gonzalo, O., Beristain, J., Jauregi, H., and Sanz, C., 2010, "A method for the identification of the specific force coefficients for mechanistic milling simulation," *International Journal of Machine Tools and Manufacture*, **50**(9), pp. 765-774.
29. Hoon Ko, J., and Cho, D.-W., 2005, "3D Ball-End Milling Force Model Using Instantaneous Cutting Force Coefficients," *Journal of Manufacturing Science and Engineering*, **127**(1), p. 1.
30. Ko, J. H., and Cho, D.-W., 2004, "Determination of Cutting-Condition-Independent Coefficients and Runout Parameters in Ball-End Milling," *The International Journal of Advanced Manufacturing Technology*, **26**(11-12), pp. 1211-1221.
31. Lamikiz, A., Lopez de Lacalle, L. N., Sanchez, J. A., and Bravo, U., 2005, "Calculation of the Specific Cutting Coefficients and Geometrical Aspects in Sculptured Surface Machining," *Machining Science and Technology*, **9**(3), pp. 411-436.
32. Powalka, B., Dhupia, J. S., Ulsoy, A. G., and Katz, R., 2008, "Identification of machining force model parameters from acceleration measurements," *International Journal of Manufacturing Research*, **3**(3), pp. 265-284.
33. Yun, W.-S., and Cho, D.-W., 2000, "An Improved Method for the Determination of 3D Cutting Force Coefficients and Runout Parameters in End Milling," *International Journal of Advanced Manufacturing Technologies*, **16**, pp. 851-858.
34. Dotcheva, M., Millward, H., and Lewis, A., 2008, "The evaluation of cutting-force coefficients using surface error measurements," *Journal of Materials Processing Technology*, **196**(1-3), pp. 42-51.
35. Kennedy, J., 2011, "Chatter Detection and Prevention in High-Speed Milling," Ph.D. Dissertation, University of Missouri.

36. Faassen, R. P. H., van de Wouw, N., Nijmeijer, H., and Oosterling, J. A. J., 2007, "An Improved Tool Path Model Including Periodic Delay for Chatter Prediction in Milling," *Journal of Computational and Nonlinear Dynamics*, **2**(2), p. 167.
37. Insperger, T. s., Gradišek, J., Kalveram, M., Stépán, G. b., Winert, K., and Govekar, E., 2006, "Machine Tool Chatter and Surface Location Error in Milling Processes," *Journal of Manufacturing Science and Engineering*, **128**(4), p. 913.
38. Bachrathy, D. n., Stépán, G. b., and Turi, J. n., 2011, "State Dependent Regenerative Effect in Milling Processes," *Journal of Computational and Nonlinear Dynamics*, **6**(4), p. 041002.
39. Li, H. Z., Liu, K., and Li, X. P., 2001, "A new method for determining the undeformed chip thickness in milling," *Journal of Materials Processing Technology*, **113**(1-3), pp. 378-384.
40. Radhakrishnan, A., Fales, R., and Mann, B., 2009, "Milling Bifurcations: A Numerical Study," *ASME International Design Engineering Technical Conferences & Computers and Information in Engineering Conference*, San Diego, CA, DETC2009-86852.
41. Campomanes, M. L., 1998, "Dynamics of Milling Flexible Structures," M.S. Masters Thesis, University of British Columbia.
42. Campomanes, M. L., and Altintas, Y., 2003, "An Improved Time Domain Simulation for Dynamic Milling at Small Radial Immersions," *Journal of Manufacturing Science and Engineering*, **125**(3), p. 416.
43. Adem, K., 2013, "Effects of Machining System Parameters and Dynamics on Quality of High-Speed Milling," Ph.D. Dissertation, University of Missouri-Columbia.
44. Kalman, R. E., 1960, "A New Approach to Linear Filtering and Prediction Problems," *Journal of Basic Engineering*, **82**(1), pp. 35-45.
45. Julier, S. J., and Uhlmann, J. K., "A New Approach for Filtering Nonlinear Systems," *Proc. Proceedings of the IEEE Americal Control Conference*, pp. 1628-1632.
46. Julier, S. J., and Uhlmann, J. K., 1997, "A New Extension of the Kalman Filter to Nonlinear Systems," *Proceedings of the SPIE, Signal Processing, Sensor Fusion, and Target Recognition VI*, **3068**, pp. 182-193.
47. Julier, S. J., and Uhlmann, J. K., 2004, "Unscented Filtering and Nonlinear Estimation," *Proceedings of the IEEE*, **92**(3), pp. 401-422.

48. Athans, M., Wishner, R. P., and Bertolini, A., 1968, "Suboptimal State Estimation for Continuous-Time Nonlinear Systems from Discrete Noisy Measurements," *IEEE Transactions on Automatic Control*, **13**(5), pp. 504-514.
49. Nørgaard, M., Poulsen, N. K., and Ravn, O., 2000, "New developments in state estimation for nonlinear systems," *Automatica*, **36**, pp. 1627-1638.
50. Ito, K., and Xiong, K., 2000, "Gaussian Filters for Nonlinear Filtering Problems," *IEEE Transactions on Automatic Control*, **45**(5), pp. 910-927.
51. Arasaratnam, I., Haykin, S., and Elliott, R., 2007, "Discrete-Time Nonlinear Filtering Algorithms Using Gauss-Hermite Quadrature," *Proceedings of the IEEE*, **95**(5), pp. 953-977.
52. Arasaratnam, I., and Haykin, S., 2009, "Cubature Kalman Filters," *IEEE Transactions on Automatic Control*, **54**(6), pp. 1254-1269.
53. Gustafsson, F., and Hendeby, G., 2012, "Some Relations Between Extended and Unscented Kalman Filters," *IEEE Transactions on Signal Processing*, **60**(2), pp. 545-555.
54. Van der Merwe, R., and Wan, E. A., "Square-Root Unscented Kalman Filter for State and Parameter Estimation," *Proc. IEEE International Conference on Acoustics, Speech, and Signal Processing*, pp. 3461-3464.
55. Simon, D., 2006, *Optimal State Estimation*, John Wiley & Sons, Inc., Hoboken, NJ.
56. Grewal, M. S., and Andrews, A. P., 2008, *Kalman Filtering: Theory and Practice Using MATLAB*, John Wiley & Sons, Inc., Hoboken, New Jersey.
57. Evans, R., Platt, E., Demanss, S., Moravek, M. K., and Morris, L., "Aluminum High Speed Machining: Metalworking Fluid Performance in Aluminum High Speed Machining," Quaker Chemical Corporation, <http://www.quakerchem.com/spanish/knowledge/brochures/quaker_aluminum_high_speed_machining.pdf>, accessed 12/19/2013.
58. Bryan, J. A., and Fales, R. C., 2013, "A Comparison of the Simulated Dynamics of Various Models Used to Predict Undeformed Chip Thickness in High-Speed Low-Radial-Immersion Milling Processes," *ASME Dynamic Systems and Controls*, Palo Alto, CA, DSCC2013-3952.
59. Hairer, E., Lubich, C., and Wanner, G., 2003, "Geometric numerical integration illustrated by the Störmer-Verlet method," *Acta Numerica*, **12**, pp. 399-450.

VITA

Josiah Bryan lived in St. Charles, MO until he was six years old, then moved to Columbia, MO, where he graduated from Rock Bridge High School in May 2006. He graduated from the University of Missouri in May 2010 with a BS in mechanical engineering with an emphasis in aerospace and minors in mathematics and business. He received an MS in mechanical and aerospace engineering at the University of Missouri in December 2011, and he hopes to receive a Ph.D. in the same discipline in May 2014. Throughout his undergraduate and graduate careers he has focused on studies in dynamics, controls, and optimization.

In addition to studying engineering, Josiah is an avid pianist, having played in the Columbia Jazz Orchestra and the University Concert Jazz Band and helped to lead worship in the Mizzou campus ministry he attended. He enjoys composing music, running, learning about other cultures, studying the pronunciation of everyday words like “war” and “when,” spending time with his wife, Rachel, and above all, getting to know his Lord and Savior Jesus Christ, Who alone is worthy of all glory and praise for every good thing in His Creation, including this dissertation.